THE UNIVERSITY OF CHICAGO

SELF-ASSEMBLY OF BLOCK COPOLYMER THIN FILMS FOR FABRICATING TAILORED NANOSTRUCTURES

A DISSERTATION SUBMITTED TO

THE FACULTY OF THE DIVISION OF THE PHYSICAL SCIENCES

IN CANDIDACY FOR THE DEGREE OF

DOCTOR OF PHILOSOPHY

DEPARTMENT OF CHEMISTRY

BY

CHUN ZHOU

CHICAGO, ILLINOIS

JUNE 2019

TABLE OF CONTENTS

LIST OF FIGURES v

LIST OF TABLES xi

ACKNOWLEDGEMENTS xii

ABSTRACT xiv

CHAPTER 1: INTRODUCTION 1

1.1 Motivations 1

1.2 Block copolymer thin films 2

1.3 Directed self-assembly of block copolymer 8

1.4 Pattern transfer for nanopatterning 11

1.6 References 12

CHAPTER 2: FABRICATION OF NANOPOROUS ALUMINA ULTRA-FILTRATION MEMBRANE WITH TUNABLE PORE SIZE USING BLOCK COPOLYMER TEMPLATES 24

2.1 Abstract 24

2.2 Introduction 24

2.3 Experimental Section 27

2.4 Results and Discussion 30

2.5 Summary 49

2.6 References 50

CHAPTER 3: STUDYING THE EFFECTS OF CHEMISTRY AND GEOMETRY ON DSA HOLE-SHRINK PROCESS IN THREE DIMENSIONS 58

3.1 Abstract 58

3.2 Introduction 58

3.3 Experimental Section 60

3.4 Results and Discussion 63

3.5 Summary 72

3.6 References 73

CHAPTER 4: COMBINING DOUBLE PATTERNING WITH SELF-ASSEMBLED BLOCK COPOLYMER LAMELLAE TO FABRICATE 10 NM FULL-PITCH LINE/SPACE PATTERNS 77

4.1 Abstract 77

4.2 Introduction 77

4.3 Experimental 79

4.4 Results and discussion 81

4.5 Summary and conclusions 90

4.6 References 91

CHAPTER 5: THERMAL CONDUCTIVITY REDUCTION IN AMORPHOUS SILICON NITRIDE PHONONIC CRYSTAL FABRICATED USING DIRECTED SELF-ASSEMBLY OF BLOCK COPOLYMERS 97

5.1 Abstract 97

5.2 Introduction 98

5.3 Experimental Section 101

5.4 Results and Discussion 104

5.5 Conclusions 119

5.6 References 120

CHAPTER 6: CONCLUSION 126

LIST OF FIGURES

Figure 2-1: Schematic illustration of BCP-templated AlO_x membrane fabrication process. PS-*b*-PMMA (C2050) BCP films were self-assembled on a random copolymer mat on top of a water-soluble PAA-Na layer. The BCP and the random copolymer films were floated off in water and transferred onto AAO membranes. The polymer film was treated with Al_2O_3 SIS to selectively grow Al_2O_3 within the PMMA microdomains. After the reaction, the samples were etched by oxygen plasma to remove the polymer, resulting in nanoporous AlO_x membrane. 31

Figure 2-2: Top-down SEM images of 30 nm (0.8 L_0) thick C2050 films on chemically modified substrates containing different mole fractions of styrene and annealed at various temperatures. Green and yellow colors indicate defect-free perpendicular PS cylinders in PMMA matrix, and nearly defect-free perpendicular cylinders with few defects around grain boundaries, respectively. 33

Figure 2-3: Top-down SEM images of C2050 films with different thickness on 30S, 63S and 85S. Samples were annealed at 270 °C for 3 h under a nitrogen atmosphere. Green, yellow and red colors indicate defect-free perpendicular PS cylinders in PMMA matrix, PS cylinders with defects around the grain boundaries, and other morphologies, respectively. 36

Figure 2-4: Top down SEM images of 141 nm thick C2050 BCP film self-assembled on 63S mat. The sample was annealed at 270 °C for 3 h under a nitrogen atmosphere. 38

Figure 2-5: (a) SEM images of 141 nm thick C2050 BCP film, BCP film treated with 3 TMA/H_2O cycles of SIS, and nanoporous AlO_x structure formed after O_2 etching. (b) Corresponding GISAXS scattering pattern at incident angle $\alpha_i = 0.200^{\circ}$. (c) Line intensity scanned along the in-plane direction around Yoneda peak *vs.* q_y 40

Figure 2-6: Top down SEM image of AlO_x membranes templated by 141 nm thick C2050 film using 3 cycles of TMA/H_2O SIS. 41

Figure 2-7: The full range of GISAXS scattering pattern for 141 nm thick C2050 BCP film after three Al_2O_3 SIS cycles and the corresponding line intensity profile vs. q_y. The hump observed in the high q range indicates that the Al_2O_3 particles formed during the SIS have weak ordering with average spacing around 3.52 nm. 41

Figure 2-8: Pore size tuning through SIS cycles: (a) SEM images of AlO_x membranes templated by 141 nm thick C2050 film using 2, 3, 4, and 5 cycles of TMA/H_2O SIS, followed by oxygen plasma etch. (b) Pore size distribution calculated from ~ 240 pores. (c) Pore diameter as a function of cycle number...42

Figure 2-9: STEM tomography characterization of alumina membrane templated by **C2050** using 3 cycles of AlO_x SIS followed by polymer etch: (a) visualization of the reconstructed volume; the dimensions of the reconstructed volume are 635 nm, 612 nm, and 62 nm (x,y,z). (b-d) 0.68 nm thick, *xy* slices of the reconstructed volume at z high of 6 nm, 34 nm, and 58 nm, respectively. $z = 0$ is defined as the height at the SiN_x substrate. (e) *yz* digitally sliced cross section of the reconstructed volume. (f) Pore diameter as a function of depth. 44

Figure 2-10: The separation of similarly size proteins: (a) the membranes performance was tested using a U-shape cell. (b) The flux of BSA and BHb measured at pH values of 4.7 and 7.0 through three different membranes: AAO membrane with average pore diameter of 100 nm, AAO membrane with average pore diameter of 20 nm, and a hierarchical membrane with BCP-templated AlO_x membrane on top of AAO membrane with average pore diameter of 100 nm (AlO_x SIS membrane). (c) Separation selectivity of BSA/BHb at pH 4.7 and BHb/BSA at pH 7 for the three membrane types. 47

Figure 2-11: (a) Surface charge *versus* pH for BSA, BHb and Al_2O_3 membranes. (c) Schematic illustrations showing the transport of BSA (blue) and BHb (red) through the membrane at pH 4.7 and 7.0. 47

Figure 3-1: Schematic illustration of DSA hole-shrink process and TEM sample preparation 60

Figure 3-2: (a) Schematic of 1.25 L_0 thick lamella-forming PS-*b*-PMMA films thermally annealed at 180 °C on substrates with different affinity to PS or PMMA. (b) Optical micrographs of 40 nm thick lamellar PS-b-PMMA (L_0 = 32nm) thin films on the mimicked SiN_x bottom surface and SOC sidewall surface before and after applying brush A or B. The inset is an SEM image of the perpendicular lamella morphology of the optically flat film. 66

Figure 3-3: Top-down SEM and 2D STEM images of two DSA samples using different brush. In each prepatterned hole, the brighter domains are Al_2O_3-stained PMMA or the sidewall surface and the darker area is PS. 67

Figure 3-4: STEM tomography reconstruction results of two DSA samples using different brush for surface modification. *xy* slices were taken at three different sample heights *z*. The brighter domains are Al_2O_3-stained PMMA or the sidewall surface and the darker domains are PS and SOC template. In the 3D visualization, Al_2O_3-stained PMMA is in blue color and PS is in red color. 68

Figure 3-5: Simulation results using coarse-grained model where the volume franction of PMMA is 0.3 and the diameter of confinement is 50 nm (1.32 L0). Only the PMMA block is presented in blue color. 69

Figure 3-6: STEM tomography results of singlets with different template CD and the representative 3D rendering. 71

Figure 4-1: Process flow of combining DSA and SADP approaches to reach the total density pitch scaling factor of 8..81

Figure 4-2: SADP results using solvent annealed P2VP-*b*-PS-*b*-P2VP self-assembly patterns. Top-down (a) and cross-sectional (b) SEM images of the Al_2O_3 spacer lines. (c) FFT spectrum showing the pitch of the Al_2O_3 spacer lines are 10.5 nm. 83

Figure 4-3: DSA result of solvent annealed P2VP-*b*-PS-*b*-P2VP (L_0=21 nm) on 84 nm pitch chemical pattern made by E-beam lithography with guiding stripes trimmed to different width W_s. DSA was successful when W_s =21.1 nm (red frame)..84

Figure 4-4: Representative top-down SEM images and corresponding full-pitch of line/space patterns of (a) E-beam patterns after trim etch; (b) DSA of P2VP-*b*-PS-*b*-P2VP after SIS; (c) AlO_x lines after polymer removal; (d) SOC mandrels; (e) ALD spacer deposited on mandrels; (f) final Al_2O_3 spacer lines after etching back 84

Figure 4-5: Top-down SEM images of (a) SOC mandrels with average line width of ~9 nm and (b) the morphology after 5 nm ALD Al_2O_3 spacer deposition and (c) the resulting Al_2O_3 spacer lines after etching back 85

Figure 4-6: Defect gallery collected from SEM images of (a) DSA pattern, (b)polymer removal, (c) SOC mandrels, (d) spacer deposition and (e) Al_2O_3 spacer lines 87

Figure 4-7: Example image of ALD spacer lines for roughness analysis: (a) the original SEM image, (b) binary image after thresholding, (c) extracted line edges. (d) The binned distribution of LWR, LER and LPR (blue) and fitting curves (red) measured from SEM image 88

Figure 4-8: Measured line roughness at each process step 89

Figure 5-1: (a) Schematic illustration of fabricating silicon nitride phononic crystals for thermoreflectance measurement. The corresponding optical microscopy images showing the fabrication process of the DSA patterned phononic crystal device: (b) pattern transfer of the BCP templated holes into SOG film; (c) photolithography and only holes in the exposed area were

transferred from SOG/SOC to silicon nitride (light blue color); (d) photolithography and metal lift-off to deposit the aluminum pads (white color); (e) silicon nitride was removed in the two triangular area; (f) the bridge of silicon nitride phononic crystal was released by Si wet etch. 104

Figure 5-2: Design of the silicon nitride phononic crystals for thermoreflectance measurement with dimensions labeled. 105

Figure 5-3: (a) Schematic illustration of DSA of PS-cylinder forming BCP on ebeam defined chemical pattern with $L_s = 2L_0$ and patterning silicon nitride with holes templated by the DSA pattern of PS cylinder forming BCP. (b) Top-down SEM images of ebeam resist pattern ($L_s = 75$ nm), DSA pattern of PS cylinder forming BCP ($L_0 = 37.5$ nm), and holes etched into silicon nitride with pitch 37.5 nm. (c) Cross-sectional SEM images of the BCP templated holes etched into SOG/SOC and silicon nitride respectively (imaged samples were tilted to 70 °). 107

Figure 5-4: (a) SEM images of the resist patterns ($L_s = 75$ nm) with different exposed hole sizes and the corresponding DSA results. The ebeam condition circled in red was used to make phononic crystal device. (b) A SEM image of the DSA result taken at the edge of the patterned area. (c) A SEM image of the DSA holes in silicon nitride over a larger area and the 2D FFT image (insect). (d) The low-magnification SEM image with Moiré interference patterns of a 50 μm × 50 μm DSA patterned area (indicated by the white dash lines) with long range ordering. Outside of the DSA patterned area, the Moiré interference patterns have multiple orientations, indicating there is no long-range ordering. 110

Figure 5-5: SEM images of DSA patterns etched into silicon nitride with different L_s and the 2D FFT images (inset). The DSA on resist pattern at $L_s = 75$ nm (in red circle) was used to make the phononic crystal device. 111

Figure 5-6: Optical microscopy and SEM images and of the suspending silicon nitride bridges (a) with DSA patterned holes (p = 37.5 nm), (b) ebeam patterned holes (p = 800 nm), and (c) without holes patterned 112

Figure 5-7: High magnification SEM images taken along the edge of the bridges and statistical analysis of hole sizes (fitted the normal distribution) of (a) DSA and (b) ebeam patterned holes. 113

Figure 5-8: The outlines of (a) DSA and (b) ebeam patterned holes extracted from SEM image. 114

Figure 5-9: (a) Schematic illustration of cross-section of the device and the thermoreflectance measurement. Laser beams are focused on the aluminum pad placed at the center of silicon nitride bridge. (b) Representative recorded reflectance signals of silicon with DSA patterned holes (red curve), ebeam patterned holes (blue curve), and unpatterned silicon nitride membrane (green curve). 115

Figure 5-10: (a) SEM images and (b) corresponding thermal conductivities of DSA patterned silicon nitride phononic crystals with four different rotation angles and self-assembled holes. The SEM images were taken near the longer edges of bridges. 118

LIST OF TABLES

Table 2-1: Average pore diameter, standard deviation, and open area fraction of AlO_x membranes templated by 141 nm thick C2050 film using various cycles of TMA/H_2O SIS, followed by oxygen plasma etch. The measurements were done using SEM images, 700 nm × 700 nm in size, with ~ 240 pores. 42

Table 3-1: Summary of wetting behaviors of bottom and sidewall surfaces 66

Table 4-1: Measured line width and line roughness values after each process 89

Table 5-1: Summary of measurement results 115

ACKNOWLEDGEMENTS

I would like to take this chance to thank many people who mentored me, supported me, encouraged me, grew up with me in the past five years. I could not have such a wonderful PhD journey without them.

Foremost, I am grateful to my advisor, Professor Paul F. Nealey. He welcomed me to join his group in Institute for Molecular Engineering as a student from Department of Chemistry. It is my honor to be the first graduate student he got at University of Chicago. He provided me so many opportunities to learn from other scholars, collaborate in different research projects, present my works in conferences and intern in company. Whenever I talked with him, he always gave positive attitude and encouraging spirit. I particularly want to thank Paul for not only teaching me not only so much about research but also training me how to better present ideas and address to different audience. I can't find a better advisor than him! I also would like to thank Professor Ka Yee Lee in Department of Chemistry. As my Pro Forma advisor, she keeps good track of my academic progress and gave me many insightful discussions and suggestions.

I thank all the present and past members of the Nealey group. Dr. Xuanxuan Chen and Dr. Jiaxing Ren were the best mentors and friends. I got my first lesson about block copolymers from them. Dr. Tamar Segal-Peretz was so patient to teach me all the tricks about tomography, and she always inspires me as a strong, confident and determined female scientist. Dr. Hyo Seon Suh taught me many great lab skills. I want to thank Dr. Paulina Rincon-Delgadillo, Dr. Xiao Li, Dr. Xiaoying Liu, Dr. Shisheng Xiong, Dr. Muhammed Enes Oruc, Dr. Christopher Arges, Dr. Manolis Doxastakis, Dr. Guangpeng Wu, Dr. Takejiro Inoue, Dr. Lance Williamson, Dr. Robert Seidel who have been so helpful since I first joined the group. They are extremely knowledgeable and always willing to discuss research with me. I also want to thank all the younger students: Moshe Dolejsi,

Yu Kambe, Jiajing Li, Elizabeth Ashley, Ruben Waldman, James Lettow, Veronica Burnett, Peter Bennington and post-docs joined the group recently: Dr. James Dolan, Dr. Ban Dong, Dr. Daniel Sharon, Dr. Hongbo Feng, Dr. Hyeong Min Jin, Dr. Ning Zhu. They are all amazing people and very enthusiastic about research. It was great sharing laboratory with all of them during last five years.

I also thank people who are not part of the Nealey group but helped me out: Cody Bezik and Dr. Grant Garner from de Pablo group, Dr. Qiti Guo and Dr. Justin Jureller in Materials Research Science & Engineering Center, Dr. Peter Duda in Pritzker Nanofabrication Facility, Dr. Nestor J. Zaluzec, Dr. Jianguo Wen, Dr. Joyce Wang, Dr. Leonidas L Ocula, Dr. Zhang Jiang, Dr. Joseph Strzalka and Dr. Jae Jin Kim from Argonne National Lab, Dr. Jan Doise and Dr. Roel Gronheid from imec (Belgium), Dr. XiaoMin Yang, Dr. Zhaoning Yu and Dr. Kim Lee in Seagate technology, Dr. Takahiro Dazai and Tsuyoshi Kwurosawa from Tokyo Ohka Kogyo co. ltd (Japan), Dr. Kouhei Takahashi, Naoki Tambo and Dr. Masaki Fujikane from Panasonic (Japan). I learned a lot from everyone, and my research would not have been possible without their generous support.

Last but not the least, I would like to thank my friends and family. My friends, especially Weiwei Chu and Ye Zhou, have always been there for me through all the ups and downs. My mom, Ying Zhou, encouraged me to pursue my graduate degree in United States while knowing living so far away from her only child is not easy. Thank you, mom!

ABSTRACT

Block copolymers (BCPs) self-assemble into periodic arrays of lamella, cylinders, spheres and gyroids with characteristic feature sizes of 3-100nm, making them ideal for fabrication of nanostructured materials. For many applications including separation membranes and nanopatterning, it is necessary to use block copolymer in thin film geometries and with domain orientations perpendicular to substrates. Chapter 2 discusses the effects of surface and interfacial energy on the self-assembly of PS-cylinder forming PS-*b*-PMMA thin films. These are less studied than the standard PMMA-cylinder forming BCPs. We explore using this BCP as a sacrificial template for the formation of nanoporous metal oxide films with tunable pore sizes. The fabricated nanoporous membrane is transferred onto a macroporous support for protein separation studies.

Directed self-assembly (DSA) of BCPs utilizes topographic or chemical contrast guide patterns to provide long-range orientational order. DSA has great potential for next generation lithography as it enables low processing cost and feature density multiplication. Defectivity is the biggest challenge for moving DSA into high-volume manufacturing. Current defectivity studies reply on surface or cross-sectional 2D metrologies. These data are not enough to describe the 3D nature of DSA morphologies and probe hidden defects under the surface. In chapter 3, we describe a 3D metrology for graphoepitaxial DSA contact-hole shrink process (to make vias) using the post-DSA membrane fabrication technique and STEM tomography. The 3D reconstruction results reveal relationships between guide patterns of different surface chemistry and geometry and types of defects in DSA morphologies.

In addition to patterning contacts using graphoepitaxial patterns, DSA using chemoepitaxial patterns is a very effective technology for line/space patterning over large area. It is of particularly interest in bit patterned media (BPM) applications. In BPM, an areal density of 5 Tb/in^2

corresponds to an 11 nm bit pitch size, which is a huge challenge for any existing lithography techniques. Chapter 4 investigates the combination of two commonly used pitch splitting techniques: DSA and self-aligned double patterning (SADP) to reach a total density multiplication factor of 8. Starting from guiding lines with 84 nm pitch, a final line/space pattern with pitch as small as 10.5 nm is demonstrated. This combined DSA and SADP strategy could avoid many sacrificial layers and etch/deposition steps to reach the same aggressive pitch scaling compared to self-aligned octuplet patterning (SAOP).

While DSA is approaching maturity for use in the semiconductor industry, researchers can develop high-resolution nanofabrication using DSA technology to solve problems in the condensed matter physics community. One revolutionary idea is to control the thermal transport by periodic nanostructures, or phononic crystal patterning. Chapter 5 describes the approach to fabricate DSA templated phononic crystal devices which have well-defined hexagonal packed holes with 38 nm pitch in suspended silicon nitride bridges. A great reduction in thermal conductivity is observed from thermoreflectance measurements. This work has applications into novel thermoelectric devices and highly sensitive bolometric radiation detectors.

CHAPTER 1: INTRODUCTION

1.1 Motivations

Nanostructured materials exhibit many interesting properties that are very different of those of bulk materials. The remarkable potential of nanostructured materials makes nanotechnology the most rapidly growing field, where scientists synthesize, characterize and process nanostructured materials to utilize their unique physical, chemical, mechanical and optical properties.[1] Scientists commonly applied two strategies to control the structure of materials at the nanoscale: top-down and bottom-up.[2] The top-down approach is to use various lithography techniques to pattern ordered nanostructures, which is used in today's semiconductor industry. The bottom-up approach is to let various nanocomposites form nanostructures with little long-range order by themselves.[2] Although top-down techniques, such as electron beam lithography, generate features as small as 10 nm, the photolithography techniques currently being used in high volume manufacturing has resolution coarser than the dimensions of structures bottom-up methods could form.[3]

The strategy to bridge top-down and bottom up and get both long-range ordering and fine resolution is "self-assembly": molecules synthesized bottom-up spontaneously form a desired pattern.[2,4] Templates fabricated top-down are often used to guide the ordering of the self-assembly process. The self-assembly is driven by noncovalent interactions to find the lowest energy configuration of the system and achieve equilibrium.[4] It is a powerful approach because scientists can design and synthesize large quantities of materials with targeted properties to form well-defined nanostructures with low-cost and high yield.[2] The self-assembly of block copolymers (BCPs) is particularly attractive. For nanolithography applications, it is a cost-effective and scalable way to pattern densely packed periodic arrays of features with dimensions typically beyond the resolution limit of conventional photolithography.

When the self-assembling block copolymer is directed by templates made by top-down conventional lithographic process, periodic nanostructures can be created with registration, perfection, accuracy as well as enhanced density. The remarkable potential to use directed self-assembly (DSA) of BCPs to providing higher resolution nanoscale features while working along with the current photolithography process is recognized by semiconductor industry. The international technology roadmap for semiconductors (ITRS) put it in the next generation lithography landscape for the fabrication of integrated circuits at advanced node.[5] Nonetheless, BCPs can be easily utilized in the lab as a tool to create uniform nanoscale features over a large area at low cost when fabricating functional materials and nanodevices for fundamental research.

The work in this dissertation elaborate the appealing aspects by using self-assembly of BCPs to create various nanostructures with potential applications in nanoporous membrane, contact via patterning for integrated circuits, high areal density bit-patterned media for future hard disk drives, and nanoscale thermal transport. The successful fabrication of functional nanostructures requires comprehensive consideration factors, including material selection, annealing conditions, interfaces and surface, etc., which in many cases reply on fundamental understanding of the thermodynamics and kinetics involved in block copolymer self-assembly.

1.2 Block copolymer thin films

1.2.1 Microphase separation

For a blend of two homopolymers, A and B, the free energy of mixing, F, described by the Flory-Huggins theory[6] is:

$$\frac{F}{k_B T} = \frac{f_A}{N_A}\ln(f_A) + \frac{f_B}{N_B}\ln(f_B) + \chi f_A f_B$$

where k_B is the Boltzmann constant, T is the temperature, f is the volume fraction of the two components ($f_A + f_B = 1$), N is the degree of polymerization, and χ is the A-B Flory-Huggins

interaction parameter. The first two terms represent the entropy component, which is negative but reduced when polymer chain is long. The third term represents the enthalpy of mixing, where χ is the free energy cost per monomer when A and B contacts. The larger positive χ is, the larger the enthalpy penalty will be when A and B contacts, and the more likely polymer/polymer blends phase separate on a micrometer scale, which is referred as macrophase separation. χ is a function of both chemistry of A and B monomers and temperature:

$$\chi = a + \frac{b}{T}$$

where a and b are experimentally obtained constants for a given pair of A and B.

Block copolymers (BCPs) have covalent bonds to link two or more different polymer chains. Unlike macrophase separation in homopolymer blends, the different polymer blocks in BCPs cannot separate completely. Instead, they form microdomain structures at nanometer scale when organizing to minimize unfavorable interactions between different polymer blocks, described as microphase separation.[7] For a diblock copolymer, A-*b*-B, the strength of segregation is proportional to χN and the microphase separation will not happen when χN <10.5 or at temperatures above the order-disorder transition (ODT) temperature, T_{ODT}. Below T_{ODT}, a linear diblock copolymer, according to the phase diagram of [8], forms spheres A in a matrix of B when f_{A} is very small. As f_{A} keeps increasing towards 0.5, it will form hexagonal cylinders, then gyroid, and finally lamellae.[8]

More morphologies were later discovered for this linear diablock copolymer. Bates and his group discovered surprisingly low-symmetry Frank-Kasper σ phases and a metastable dodecagonal quasicrystalline phase in sphere-forming poly(isoprene)-b-poly(lactide) diblock copolymers.[9–11] The phase behaviors of multiblock copolymers and branched block copolymers

are even more complicated. For example, linear ABC triblock copolymers are know to form phases including lamellae (L) phases, core-shell versions of the gyroid (G), hexagonal cylinder (C), body-centered cubic (BCC) sphere phases (S), "alternating" versions of the gyroid (G^A), diamond (D^A), cylinder (C^A), and sphere (S^A and F^A) phases, and an *Fddd* (or O^{70}) network phase.[12,13] The freedom to select different polymer chemistries, to vary block lengths, and to even blend in other components provides unlimited potential for designing BCPs to create nanostructures with precisely specified microdomain geometry, packing symmetry and chemical composition.[14]

1.2.2 Self-assembly of block copolymer thin films

Although BCPs in bulk and solution have extensive applications ranging from templating materials to drug delivery,[15] the nanopatterning patterning application has particular interest where BCPs are usually used as thin films or in confined spaces. In thin films, the orientation of BCPs microdomains is sensitive to boundary conditions including the polymer-air or polymer-vacuum interface and polymer-substrate interface. The total free energy F of BCP thin films can be approximated as:

$$F = F_{poly,poly} + F_{elastic} + F_{Poly,air} + F_{Poly,sub}$$

The first two terms are associated with the interfacial energy between different domains and the configurational entropy of the polymer chains, governing the BCP self-assembly in the bulk. The third and fourth terms represent the surface energy and the interfacial energy.[16]

When one block preferentially wets the surface or interface, the lamellae and cylinders orient parallelly to the substrate to minimize surface energy and interfacial energy. One block wetting both the surface and interface is referred as symmetric wetting, while different blocks wetting surface and interface is described as asymmetric wetting.[17] For parallel lamellae pattern, holes or islands form when the film thickness is incommensurate with the BCP natural period, L_0.[17] If

knowing the film thickness and L_0, the surface topography (islands or holes) as well as step heights are very useful to tell the preferentiality of surface and interface.[18–20]

For many nanopatterning applications, perpendicular microdomain orientation is more desired. To balance interfacial energy, the surface of substrate could be easily chemically modified to make it have similar interaction strength with different polymer blocks, which is referred as surface neutralization. Mansky et al. showed that to induce perpendicular domain orientation of poly(styrene-b-methyl methacrylate) (PS-b-PMMA) lamella, the substrate surface could be modified with a random copolymer (PS-*b*-PMMA) with composition tailored to neutrally wet both PS and PMMA.[21,22] The random copolymers used for chemical modification are often brushes or mat. Brushes have hydroxyl groups in each chain that attach to a surface to form thin polymer layers and mats are thin cross-linked networks.[23] Han et al. studied the range of different random copolymer brush and mat layers to form vertical structures of PS PS-*b*-PMMA cylinders and lamellae.[24] In thin films, the orientation often propagates throughout the film thickness. When the BCP film is thicker, the nucleation and growth of microdomains from surface and interface become decoupled.[25–27] Han et al. showed that the PS-*b*-PMMA cylindrical domains have areas with disconnections or junctions in the middle of the film where two nucleation frons meet in 300-900 thick films.[26] For PS-*b*-PMMA, the most commonly used BCP for thin film nanopatterning applications, the control of domain orientation often relies on substrate surface modification because the upper surface is assumed to be relatively neutral to PS and PMMA. PS and PMMA have similar surface energies in the annealing temperature range used in most studies[28,29], but this is usually not the case for other block copolymer systems. For BCPs with more distinct surface energies between different blocks, scientists have developed various strategies including: top-coat surface treatment,[30,31] solvent annealing,[32] BCPs with decoupled bulk thermodynamics and

wetting characteristics,[19] surface active and phase-preferential additives[33] or embedded neutral layer,[34] to neutralize top surface and control orientation.

1.2.3 Thermal annealing and solvent annealing

Commonly, BCP thin films are prepared by spin-coating. The solvent runs off quickly, so the as-spun films have structures far away from equilibrium. To evolve the self-assembly towards thermodynamic equilibrium morphology, BCP films are often annealed at elevated temperatures, known as thermal annealing, or in solvent vapor at room temperature, known as solvent annealing.

For thermal annealing, BCP films are heated up to and hold at a temperature greater than glass transition temperature, T_g, to enable polymers disentangle and alter configurations but not to exceed T_{ODT} or cause polymer degradation. The diffusivity, D, of a polymer chain exhibits Arrhenius dependence on temperature, T:

$$D = A \exp(-\frac{\Delta E_a}{RT})$$

where A is a constant, E_a is the apparent activation energy of a polymer, and R is the ideal gas constant.[35] Increasing the thermal annealing temperature leads to faster ordering kinetics. During thermal annealing, the two-dimensional ordering of BCP morphology is often observed to improve with the formation of equilibrium nanodomains.[36] The BCP nanodomains arrange into polycrystalline arrays with small grains collapse into larger grains along annealing. The rotation of small grains could be main pathway to merge into large grains.[37] On the boundary of two grains, the nanodomains have disclinations or dislocations defects. With self-assembly process alone, the polycrystalline grains could not grow into a single crystal grain. The grain boundary defects always persist in the self-assembly pattern. Ji et al. found that the in cylinder forming PS-*b*-PMMA films, diffusivity was faster at surface than that near interface and thicker films have faster ordering kinetics and larger grain size than thin films.[37] Welander et al. reported that increasing the

annealing temperature could shorten the annealing time to achieve defect free pattern in the case of directed self-assembly of PS-*b*-PMMA.[38]

The other commonly used method, solvent annealing, increases the polymer chain mobility by lowering the T_g of solvent-swollen BCP films under room temperature. Kim et al. used solvent annealing significantly facilitated the mass transport in high molecular weight PS-*b*-PMMA which is hardly achievable using thermal annealing alone.[39] The solvent annealing driven self-assembley follows a "quasi-equilibrium and quenching" mechanism.[40] When the dry BCP film absorb the solvents and swell, the microdomain structures of the swollen film at equilibrium depend on the solvent selectivity and the swelling ratio. Then the self-assembly is quenched by quickly removing the solvent from BCP film. The final morphology in the rapidly dried films is maintained except for shrinking in the direction normal to the substrate.[41] The swelling ratio of BCP film depends on the solvent vapor pressure, which is more difficult to control compared with thermal annealing temperature. Therefore, solvent annealing is considerate not as industry-friendly as thermal annealing. One setup developed for more reproducible solvent annealing process uses continuous inert gas flow to carry solvent vapor to BCP films by bubbling through liquid solvent. After annealing, the solvent could be rapidly removed from BCP by purging pure inert gas.[42] When polymer volume fraction, ϕ, is large, the swollen film is at glass state at low T and the polymer chain doesn't have sufficient mobility, which is the higher limit of ϕ corresponding to T_g. The effective interaction parameter in the BCP and solvent mixture is:

$$\chi_{\text{eff}} = \chi\phi^a$$

where a describes the selectivity of solvent. Neutral solvent, which distributes equally in different polymer blocks, has $a = 1$ in SCMF theory and reduces the effective segregation strength.[43] If ϕ is too small, an order-disorder phase transition occurs and the BCP could not phase separate in

swollen state. This is the lower limit of ϕ corresponding to $(\chi N)_{\mathrm{ODT}}$.[41] The variations in χ_{eff} leads to changes in the periods of BCP domains at swollen state. A neutral or slightly selective solvent reduces the period, while a strong selective solvent (a is larger) increase the period as chains need to stretch more to reduce more unfavored interfacial area between blocks.[35]

There is a growing desire to reduce the self-assembly processing time. A diversity of annealing methods have been developed, such as microwave annealing,[44] solvo-microwave annealing,[45] and laser annealing[46]. The principles of these rapid annealing method are still very similar to the basic thermal annealing and solvent annealing. Although some newer methods are very amenable to scale-up roll-to-roll process, currently pure thermal annealing remains attractive to industry from the point of view of simple process.[47]

1.3 Directed self-assembly of block copolymer

The polycrystalline grains, or "fingerprint" structures, formed in self-assembled BCP films only have short-range ordering. For many lithographic applications, it is necessary to have BCP structures organized in long-range order or in a desired placement. For this purpose, different directed self-assembly (DSA) techniques have been developed to control the placement of BCP domains, and they have mainly two categories: graphoepitaxy topographic patterns, and chemoepitaxy on chemical patterns. Epitaxy, a term often used in crystal growth, describes the self-assembled BCP domains are growing in accordance with the patterned substrate and thus grain coarsening stage is eliminated.

1.3.1 Graphoepitaxy

Graphoepitaxy utilizes topographic features, such as trenches to guide the self-assembly of BCPs. Kramer and coworkers first demonstrated with substrates with shallow trenches separated by several micrometers lead to long-range ordering of poly(styrene-*b*-2-vinylpyridine) (PS-*b*-

P2VP) spheres over areas up to two hundred domains wide.[48] The ordering of BCP domains within topographic confinement is mainly governed by commensurability of the confined geometry with the BCP sizes and the interaction of each block with template surface. Ross and coworkers used narrower templates for poly(styrene-*b*-ferrocenylsilane) (PS-*b*-PFS) spheres and found perfect *n* rows of spheres form when the wall spacing is between $(n\text{-}0.5)L_0$ and $(n+0.5)L_0$.[49] Han et al. found PS-*b*-PMMA lamellar domains orient perpendicularly to both trench bottom and sidewall when the surface of trench is homogeneous non-preferential, but the orientation with respect to trench sidewalls becomes parallel by adjusting film thickness when the surface is weakly preferential.[50]

Many groups have used various types of BCPs and topographic patterns to further develop graphoepitaxy method. Successful DSA patterns were templated using hydrogen silsesquioxane (HSQ) pillars,[51] V shape grooves formed by <111> Si planes,[52] nanoscopic surface facets generated from single-crystalline wafers,[53] imprint molds,[54] and even inorganic nanowires converted from the fist layer BCP could be used to align the additional BCP films.[55]

1.3.2 Chemoepitaxy

Chemoepitaxy uses patterns having regions preferentially wet different blocks, or chemical contrast, to induce the formation of single-orientation patterns.[56] Nealey and coworkers used extreme ultraviolet (EUV) interferometric lithography to pattern self-assembled monolayers (SAMs).[56] The PMMA preferentially wet the SAMs in the exposed area and the other regions were non-preferential to PS and PMMA. When the period of chemically patterned SAM matches L_0, the orientation of PS-*b*-PMMA lamella perfectly matches the pattern. When the underlying chemical pattern mismatches L_0, BCP forms defects to minimize the strain.[56] BCP directed by chemical patterns could form complex geometries with great fidelity. Nealey and coworkers demonstrated the perfect registration of PS-*b*-PMMA lamella for device-oriented non-regular structures.[57,58]

This 1:1 patterning doesn't prove smaller feature dimensions and advanced lithography is required to fabricate templates for small BCPs. The resolution enhancement by DSA with density multiplication provides higher resolution and throughput beyond the capabilities of lithographic process used to make chemical patterns, and thus it has been pursued by semiconductor industry. Ruiz et al. only patterned every other spot on PS-OH brush by electron beam lithography and pattern period, L_s = 54 nm. DSA of PS-*b*-PMMA cylinders with L_0 = 27 nm result in defect-free hexagonal arrays of cylinders with long-range order over the entire area, multiplying the feature density by a factor of 4, known as the density multiplication factor.[59] Analogous to the density multiplication of BCP cylinders, lamellae-forming BCPs on sparse chemical patterns could enhance resolution of line and space patterns, which is very useful to pattern unidirectional dense lines.[60] Liu et al. developed a process known as LiNe flow to fabricate chemical patterns, which has been widely used for chemoepitaxy studies.[61–63] The LiNe flow uses a crosslinked polymer mat on substrate, followed by lithographic patterning of photoresist on top of the mat. The mat is etched and trimmed to width of W with top surface protected under photoresist. After stripping photoresist, a brush is backfilled into the interspatial regions of patterned mat to create chemical contrast.

The control of W, L_s, and background chemistry is critical to obtain a defect-free DSA.[61,64,65] For DSA of PS-*b*-PMMA, zero dislocation defects can be achieved on optimized chemical pattern at thermodynamic equilibrium, as the free energy of defects is much higher than that of the aligned state.[66,67] Along with the thermodynamics, kinetics also plays an important role in DSA. Both theoretical and experimental studies show that the defective morphologies are not equilibrium structures but metastable state that are kinetically trapped long the annihilation pathway. With kinetic barriers, even aligned structure has lower energy at equilibrium, defects are often difficult

to annihilate.[66–69] The chemical patterns made with LiNe flow originally has minimal template topography. Recent studies show that chemically modified sidewalls also have enthalpic interactions and pin one of the blocks.[65,70–72] Chemical patterns having higher topography, or combined chemical and topographic template could provide additional driving force for alignment. Enhanced DSA kinetics and defects reduction were observed.[70,73]

1.4 Pattern transfer for nanopatterning

Applications using self-assembled BCP thins films often involve pattern transfer, so the nanostructures formed in BCP could be replicated in different materials. Analogous to the development step in photolithography, pattern transfer of BCP pattern requires selectively removing one of the blocks so the remaining materials could serve as the etch mask. The selectivity between two blocks is thus an important factor when choosing and developing BCP materials. Many approaches have been developed to selectively remove one block. For example, "wet PMMA development" is commonly used for PS-*b*-PMMA pattern. It utilizes UV irradiation to degrade PMMA block followed by dissolving PMMA segments in acetic acid while leaving PS structure intact.[74] The pattern collapse using wet process is an important concern.[75] Plasma etching could be a better option if two blocks have dry etch selectivity to reduce the collapsing.[76] Inorganic materials can be added to the BCPs to enhance dry etch contrast by polymer synthesis or post-assembly infusion. Some iron-containing and Si-containing BCP systems showed high etch contrast tween the organic and inorganic blocks.[30,77–81]

The work in this thesis utilizes a process termed as sequential infiltration synthesis (SIS)[82,83] in infuse inorganic materials into BCP pattern. The SIS process uses standard atomic layer deposing (ALD) setup. Compared to regular ALD deposition, the SIS mode has much longer reaction time and higher pressure to allow ALD precursors diffuse deeply into BCP films.[84] The BCPs suitable

for SIS often contains one polar block and one non-polar block, such as PS-*b*-PMMA[82,85,86] and PS-*b*-P2VP[17,87]. Al_2O_3 is the most commonly used metal oxide for SIS and used in this thesis. The BCP film is first exposed to the vapor of metal precursor for a given time, which is trimethylaluminum (TMA) in the case of Al_2O_3. The metal precursor diffuses into the BCP and selectively bind to the polar components. The excess precursor vapor is removed by inert gas in a purge step. Then another cycle using the vapor of the co-reactant precursor is run to finish the reaction on the sites of metal precursor. In the case of Al_2O_3, water is used. In this way, the growth of metal oxide only happens in the polar block. The full cycle is repeated for several times to increase the amount of metal oxide. The polymer matrix could be removed by plasma etching leaving behind the inorganic pattern that replicates the original BCP pattern. Biswas et al. used in-situ Fourier transform infrared (FTIR) spectroscopy to investigate the SIS mechanism.[88,89] They found that the TMA form an unstable intermediate complex with PMMA quickly but the conversion of this intermediate complex into covalently-bonded structure is slow and competing with TMA desorption. Therefore, longer exposure time and shorter purge time will promote the SIS reaction. In addition to Al_2O_3, various inorganic materials, including TiO_2,[83] SiO_2,[82] ZnO,[82] and WO_3,[90] used for SIS process have been reported.

1.6 References

(1) Gleiter, H. Nanostructured Materials: Basic Concepts and Microstructure. *Acta Mater.* **2000**, *48* (1), 1–29.

(2) Whitesides, G. M.; Kriebel, J. K.; Mayers, B. T. Self-Assembly and Nanostructured Materials. In *Nanoscale Assembly*; Huck, W. T. S., Ed.; Springer US: Boston, MA, **2005**; 217–239.

(3) Brunner, T. A. Why Optical Lithography Will Live Forever. *J. Vac. Sci. Technol. B*

Microelectron. Nanom. Struct. **2003**, *21* (6), 2632.

(4) Whitesides, G.; Mathias, J.; Seto, C. Molecular Self-Assembly and Nanochemistry: A Chemical Strategy for the Synthesis of Nanostructures. *Science (80-.).* **1991**, *254* (5036), 1312–1319.

(5) International Technology Roadmap for Semiconductors 2.0 Lithography. **2015**.

(6) Flory, P. J. *Principles of Polymer Chemistry*; Cornell University Press, 1953.

(7) Bates, F. S.; Fredrickson, G. H. Block Copolymer Thermodynamics: Theory and Experiment. *Annu. Rev. Phys. Chem.* **1990**, *41* (1), 525–557.

(8) Bates, F. S.; Fredrickson, G. H. Block Copolymers—Designer Soft Materials. *Phys. Today* **1999**, *52* (2), 32–38.

(9) Lee, S.; Bluemle, M. J.; Bates, F. S. Discovery of a Frank-Kasper Phase in Sphere-Forming Block Copolymer Melts. *Science (80-.).* **2010**, *330* (6002), 349–353.

(10) Kim, K.; Schulze, M. W.; Arora, A.; Lewis, R. M.; Hillmyer, M. A.; Dorfman, K. D.; Bates, F. S. Thermal Processing of Diblock Copolymer Melts Mimics Metallurgy. *Science (80-.).* **2017**, *356* (6337), 520–523.

(11) Gillard, T. M.; Lee, S.; Bates, F. S. Dodecagonal Quasicrystalline Order in a Diblock Copolymer Melt. *Proc. Natl. Acad. Sci.* **2016**, *113* (19), 5167–5172.

(12) Chatterjee, J.; Jain, S.; Bates, F. S. Comprehensive Phase Behavior of Poly(Isoprene- b -Styrene- b -Ethylene Oxide) Triblock Copolymers. *Macromolecules* **2007**, *40* (8), 2882–2896.

(13) Qin, J.; Bates, F. S.; Morse, D. C. Phase Behavior of Nonfrustrated ABC Triblock Copolymers: Weak and Intermediate Segregation. *Macromolecules* **2010**, *43* (11), 5128–5136.

(14) Bates, F. S.; Hillmyer, M. A.; Lodge, T. P.; Bates, C. M.; Delaney, K. T.; Fredrickson, G. H. Multiblock Polymers: Panacea or Pandora's Box? *Science (80-.).* **2012**, *336* (6080), 434–440.

(15) Schacher, F. H.; Rupar, P. A.; Manners, I. Functional Block Copolymers: Nanostructured Materials with Emerging Applications. *Angew. Chemie Int. Ed.* **2012**, *51* (32), 7898–7921.

(16) Edwards, E. W.; Montague, M. F.; Solak, H. H.; Hawker, C. J.; Nealey, P. F. Precise Control over Molecular Dimensions of Block-Copolymer Domains Using the Interfacial Energy of Chemically Nanopatterned Substrates. *Adv. Mater.* **2004**, *16* (15), 1315–1319.

(17) Suh, H. S.; Kim, D. H.; Moni, P.; Xiong, S.; Ocola, L. E.; Zaluzec, N. J.; Gleason, K. K.; Nealey, P. F. Sub-10-Nm Patterning via Directed Self-Assembly of Block Copolymer Films with a Vapour-Phase Deposited Topcoat. *Nat. Nanotechnol.* **2017**, *12* (6), 575–581.

(18) Smith, A. P.; Sehgal, A.; Douglas, J. F.; Karim, A.; Amis, E. J. Combinatorial Mapping of Surface Energy Effects on Diblock Copolymer Thin Film Ordering. *Macromol. Rapid Commun.* **2003**, *24* (1), 131–135.

(19) Kim, S.; Nealey, P. F.; Bates, F. S. Decoupling Bulk Thermodynamics and Wetting Characteristics of Block Copolymer Thin Films. *ACS Macro Lett.* **2012**, *1* (1), 11–14.

(20) Kim, S.; Bates, C. M.; Thio, A.; Cushen, J. D.; Ellison, C. J.; Willson, C. G.; Bates, F. S. Consequences of Surface Neutralization in Diblock Copolymer Thin Films. *ACS Nano* **2013**, *7* (11), 9905–9919.

(21) Mansky, P. Controlling Polymer-Surface Interactions with Random Copolymer Brushes. *Science (80-.).* **1997**, *275* (5305), 1458–1460.

(22) Mansky, P.; Russell, T. P.; Hawker, C. J.; Pitsikalis, M.; Mays, J. Ordered Diblock Copolymer Films on Random Copolymer Brushes. *Macromolecules* **1997**, *30* (22), 6810–

6813.

(23) Han, E.; Stuen, K. O.; La, Y.-H.; Nealey, P. F.; Gopalan, P. Effect of Composition of Substrate-Modifying Random Copolymers on the Orientation of Symmetric and Asymmetric Diblock Copolymer Domains. *Macromolecules* **2008**, *41* (23), 9090–9097.

(24) Han, E.; Stuen, K. O.; La, Y.-H.; Nealey, P. F.; Gopalan, P. Effect of Composition of Substrate-Modifying Random Copolymers on the Orientation of Symmetric and Asymmetric Diblock Copolymer Domains. *Macromolecules* **2008**, *41* (23), 9090–9097.

(25) Xu, T.; Hawker, C. J.; Russell, T. P. Interfacial Interaction Dependence of Microdomain Orientation in Diblock Copolymer Thin Films. *Macromolecules* **2005**, *38* (7), 2802–2805.

(26) Han, E.; Stuen, K. O.; Leolukman, M.; Liu, C.-C.; Nealey, P. F.; Gopalan, P. Perpendicular Orientation of Domains in Cylinder-Forming Block Copolymer Thick Films by Controlled Interfacial Interactions. *Macromolecules* **2009**, *42* (13), 4896–4901.

(27) Welander, A. M.; Craig, G. S. W.; Tada, Y.; Yoshida, H.; Nealey, P. F. Directed Assembly of Block Copolymers in Thin to Thick Films. *Macromolecules* **2013**, *46* (10), 3915–3921.

(28) Wu, S. Surface and Interfacial Tensions of Polymer Melts. II. Poly(Methyl Methacrylate), Poly(n-Butyl Methacrylate), and Polystyrene. *J. Phys. Chem.* **1970**, *74* (3), 632–638.

(29) Mansky, P.; Russell, T. P.; Hawker, C. J.; Mays, J.; Cook, D. C.; Satija, S. K. Interfacial Segregation in Disordered Block Copolymers: Effect of Tunable Surface Potentials. *Phys. Rev. Lett.* **1997**, *79* (2), 237–240.

(30) Bates, C. M.; Seshimo, T.; Maher, M. J.; Durand, W. J.; Cushen, J. D.; Dean, L. M.; Blachut, G.; Ellison, C. J.; Willson, C. G. Polarity-Switching Top Coats Enable Orientation of Sub-10-Nm Block Copolymer Domains. *Science (80-.).* **2012**, *338* (6108), 775–779.

(31) Suh, H. S.; Kim, D. H.; Moni, P.; Xiong, S.; Ocola, L. E.; Zaluzec, N. J.; Gleason, K. K.;

Nealey, P. F. Sub-10-Nm Patterning via Directed Self-Assembly of Block Copolymer Films with a Vapour-Phase Deposited Topcoat. *Nat. Nanotechnol.* **2017**, *12* (6), 575–581.

(32) Sinturel, C.; Vayer, M.; Morris, M.; Hillmyer, M. A. Solvent Vapor Annealing of Block Polymer Thin Films. *Macromolecules* **2013**, *46* (14), 5399–5415.

(33) Vora, A.; Schmidt, K.; Alva, G.; Arellano, N.; Magbitang, T.; Chunder, A.; Thompson, L. E.; Lofano, E.; Pitera, J. W.; Cheng, J. Y.; et al. Orientation Control of Block Copolymers Using Surface Active, Phase-Preferential Additives. *ACS Appl. Mater. Interfaces* **2016**, *8* (43), 29808–29817.

(34) Zhang, J.; Clark, M. B.; Wu, C.; Li, M.; Trefonas, P.; Hustad, P. D. Orientation Control in Thin Films of a High-χ Block Copolymer with a Surface Active Embedded Neutral Layer. *Nano Lett.* **2016**, *16* (1), 728–735.

(35) Ji, S.; Wan, L.; Liu, C.-C.; Nealey, P. F. Directed Self-Assembly of Block Copolymers on Chemical Patterns: A Platform for Nanofabrication. *Prog. Polym. Sci.* **2016**, *54–55*, 76–127.

(36) Segalman, R. A. Patterning with Block Copolymer Thin Films. *Mater. Sci. Eng. R Reports* **2005**, *48* (6), 191–226.

(37) Ji, S.; Liu, C.-C.; Liao, W.; Fenske, A. L.; Craig, G. S. W.; Nealey, P. F. Domain Orientation and Grain Coarsening in Cylinder-Forming Poly(Styrene- b -Methyl Methacrylate) Films. *Macromolecules* **2011**, *44* (11), 4291–4300.

(38) Welander, A. M.; Kang, H.; Stuen, K. O.; Solak, H. H.; Müller, M.; de Pablo, J. J.; Nealey, P. F. Rapid Directed Assembly of Block Copolymer Films at Elevated Temperatures. *Macromolecules* **2008**, *41* (8), 2759–2761.

(39) Kim, E.; Ahn, H.; Park, S.; Lee, H.; Lee, M.; Lee, S.; Kim, T.; Kwak, E.-A.; Lee, J. H.; Lei, X.; et al. Directed Assembly of High Molecular Weight Block Copolymers: Highly Ordered

Line Patterns of Perpendicularly Oriented Lamellae with Large Periods. *ACS Nano* **2013**, *7* (3), 1952–1960.

(40) Paik, M. Y.; Bosworth, J. K.; Smilges, D.-M.; Schwartz, E. L.; Andre, X.; Ober, C. K. Reversible Morphology Control in Block Copolymer Films via Solvent Vapor Processing: An in Situ GISAXS Study. *Macromolecules* **2010**, *43* (9), 4253–4260.

(41) Hur, S.-M.; Khaira, G. S.; Ramírez-Hernández, A.; Müller, M.; Nealey, P. F.; de Pablo, J. J. Simulation of Defect Reduction in Block Copolymer Thin Films by Solvent Annealing. *ACS Macro Lett.* **2015**, *4* (1), 11–15.

(42) Gotrik, K. W.; Hannon, A. F.; Son, J. G.; Keller, B.; Alexander-Katz, A.; Ross, C. A. Morphology Control in Block Copolymer Films Using Mixed Solvent Vapors. *ACS Nano* **2012**, *6* (9), 8052–8059.

(43) Whitmore, M. D.; Vavasour, J. D. Self-Consistent Mean Field Theory of the Microphase Diagram of Block Copolymer/Neutral Solvent Blends. *Macromolecules* **1992**, *25* (7), 2041–2045.

(44) Jin, C.; Murphy, J. N.; Harris, K. D.; Buriak, J. M. Deconvoluting the Mechanism of Microwave Annealing of Block Copolymer Thin Films. *ACS Nano* **2014**, *8* (4), 3979–3991.

(45) Mokarian-Tabari, P.; Cummins, C.; Rasappa, S.; Simao, C.; Sotomayor Torres, C. M.; Holmes, J. D.; Morris, M. A. Study of the Kinetics and Mechanism of Rapid Self-Assembly in Block Copolymer Thin Films during Solvo-Microwave Annealing. *Langmuir* **2014**, *30* (35), 10728–10739.

(46) Jiang, J.; Jacobs, A. G.; Wenning, B.; Liedel, C.; Thompson, M. O.; Ober, C. K. Ultrafast Self-Assembly of Sub-10 Nm Block Copolymer Nanostructures by Solvent-Free High-Temperature Laser Annealing. *ACS Appl. Mater. Interfaces* **2017**, *9* (37), 31317–31324.

(47) Majewski, P. W.; Yager, K. G. Rapid Ordering of Block Copolymer Thin Films. *J. Phys. Condens. Matter* **2016**, *28* (40), 403002.

(48) Segalman, R. A.; Yokoyama, H.; Kramer, E. J. Graphoepitaxy of Spherical Domain Block Copolymer Films. *Adv. Mater.* **2001**, *13* (15), 1152–1155.

(49) Cheng, J. Y.; Mayes, A. M.; Ross, C. A. Nanostructure Engineering by Templated Self-Assembly of Block Copolymers. *Nat. Mater.* **2004**, *3* (11), 823–828.

(50) Han, E.; Kang, H.; Liu, C.-C.; Nealey, P. F.; Gopalan, P. Graphoepitaxial Assembly of Symmetric Block Copolymers on Weakly Preferential Substrates. *Adv. Mater.* **2010**, *22* (38), 4325–4329.

(51) Bita, I.; Yang, J. K. W.; Jung, Y. S.; Ross, C. A.; Thomas, E. L.; Berggren, K. K. Graphoepitaxy of Self-Assembled Block Copolymers on Two-Dimensional Periodic Patterned Templates. *Science (80-.).* **2008**, *321* (5891), 939–943.

(52) Chuang, V. P.; Cheng, J. Y.; Savas, T. A.; Ross, C. A. Three-Dimensional Self-Assembly of Spherical Block Copolymer Domains into V-Shaped Grooves. *Nano Lett.* **2006**, *6* (10), 2332–2337.

(53) Park, S.; Lee, D. H.; Xu, J.; Kim, B.; Hong, S. W.; Jeong, U.; Xu, T.; Russell, T. P. Macroscopic 10-Terabit-per-Square-Inch Arrays from Block Copolymers with Lateral Order. *Science (80-.).* **2009**, *323* (5917), 1030–1033.

(54) Li, H.-W.; Huck, W. T. S. Ordered Block-Copolymer Assembly Using Nanoimprint Lithography. *Nano Lett.* **2004**, *4* (9), 1633–1636.

(55) Majewski, P. W.; Rahman, A.; Black, C. T.; Yager, K. G. Arbitrary Lattice Symmetries via Block Copolymer Nanomeshes. *Nat. Commun.* **2015**, *6* (1), 7448.

(56) Ouk Kim, S.; Solak, H. H.; Stoykovich, M. P.; Ferrier, N. J.; de Pablo, J. J.; Nealey, P. F.

Epitaxial Self-Assembly of Block Copolymers on Lithographically Defined Nanopatterned Substrates. *Nature* **2003**, *424* (6947), 411–414.

(57) Stoykovich, M. P. Directed Assembly of Block Copolymer Blends into Nonregular Device-Oriented Structures. *Science (80-.).* **2005**, *308* (5727), 1442–1446.

(58) Liu, G.; Thomas, C. S.; Craig, G. S. W.; Nealey, P. F. Integration of Density Multiplication in the Formation of Device-Oriented Structures by Directed Assembly of Block Copolymer-Homopolymer Blends. *Adv. Funct. Mater.* **2010**, *20* (8), 1251–1257.

(59) Ruiz, R.; Kang, H.; Detcheverry, F. A.; Dobisz, E.; Kercher, D. S.; Albrecht, T. R.; De Pablo, J. J.; Nealey, P. F. Density Multiplication and Improved Lithography by Directed Block Copolymer Assembly. *Science (80-.).* **2008**, *321* (5891), 936–939.

(60) Cheng, J. Y.; Rettner, C. T.; Sanders, D. P.; Kim, H.-C.; Hinsberg, W. D. Dense Self-Assembly on Sparse Chemical Patterns: Rectifying and Multiplying Lithographic Patterns Using Block Copolymers. *Adv. Mater.* **2008**, *20* (16), 3155–3158.

(61) Liu, C.-C.; Ramírez-Hernández, A.; Han, E.; Craig, G. S. W.; Tada, Y.; Yoshida, H.; Kang, H.; Ji, S.; Gopalan, P.; de Pablo, J. J.; et al. Chemical Patterns for Directed Self-Assembly of Lamellae-Forming Block Copolymers with Density Multiplication of Features. *Macromolecules* **2013**, *46* (4), 1415–1424.

(62) Liu, C.-C.; Han, E.; Onses, M. S.; Thode, C. J.; Ji, S.; Gopalan, P.; Nealey, P. F. Fabrication of Lithographically Defined Chemically Patterned Polymer Brushes and Mats. *Macromolecules* **2011**, *44* (7), 1876–1885.

(63) Liu, C.-C.; Nealey, P. F.; Raub, A. K.; Hakeem, P. J.; Brueck, S. R. J.; Han, E.; Gopalan, P. Integration of Block Copolymer Directed Assembly with 193 Immersion Lithography. *J. Vac. Sci. Technol. B, Nanotechnol. Microelectron. Mater. Process. Meas. Phenom.* **2010**,

28 (6), C6B30-C6B34.

(64) Garner, G. P.; Rincon Delgadillo, P.; Gronheid, R.; Nealey, P. F.; de Pablo, J. J. Design of Surface Patterns with Optimized Thermodynamic Driving Forces for the Directed Self-Assembly of Block Copolymers in Lithographic Applications. *Mol. Syst. Des. Eng.* **2017**, *2* (5), 567–580.

(65) Williamson, L. D.; Seidel, R. N.; Chen, X.; Suh, H. S.; Rincon Delgadillo, P.; Gronheid, R.; Nealey, P. F. Three-Tone Chemical Patterns for Block Copolymer Directed Self-Assembly. *ACS Appl. Mater. Interfaces* **2016**, *8* (4), 2704–2712.

(66) Hur, S.-M.; Thapar, V.; Ramírez-Hernández, A.; Khaira, G.; Segal-Peretz, T.; Rincon-Delgadillo, P. A.; Li, W.; Müller, M.; Nealey, P. F.; de Pablo, J. J. Molecular Pathways for Defect Annihilation in Directed Self-Assembly. *Proc. Natl. Acad. Sci.* **2015**, *112* (46), 14144–14149.

(67) Hur, S.-M.; Thapar, V.; Ramírez-Hernández, A.; Nealey, P. F.; de Pablo, J. J. Defect Annihilation Pathways in Directed Assembly of Lamellar Block Copolymer Thin Films. *ACS Nano* **2018**, *12* (10), 9974–9981.

(68) Ren, J.; Zhou, C.; Chen, X.; Dolejsi, M.; Craig, G. S. W.; Delgadillo, P. A. R.; Segal-Peretz, T.; Nealey, P. F. Engineering the Kinetics of Directed Self-Assembly of Block Copolymers toward Fast and Defect-Free Assembly. *ACS Appl. Mater. Interfaces* **2018**, *10*, 23414–23423.

(69) Raybin, J.; Ren, J.; Chen, X.; Gronheid, R.; Nealey, P. F.; Sibener, S. J. Real-Time Atomic Force Microscopy Imaging of Block Copolymer Directed Self Assembly. *Nano Lett.* **2017**, *17* (12), 7717–7723.

(70) Blachut, G.; Sirard, S. M.; Maher, M. J.; Asano, Y.; Someya, Y.; Lane, A. P.; Durand, W.

J.; Bates, C. M.; Dinhobl, A. M.; Gronheid, R.; et al. A Hybrid Chemo-/Grapho-Epitaxial Alignment Strategy for Defect Reduction in Sub-10 Nm Directed Self-Assembly of Silicon-Containing Block Copolymers. *Chem. Mater.* **2016**, *28* (24), 8951–8961.

(71) Segal-Peretz, T.; Ren, J.; Xiong, S.; Khaira, G.; Bowen, A.; Ocola, L. E.; Divan, R.; Doxastakis, M.; Ferrier, N. J.; De Pablo, J.; et al. Quantitative Three-Dimensional Characterization of Block Copolymer Directed Self-Assembly on Combined Chemical and Topographical Prepatterned Templates. *ACS Nano* **2017**, *11* (2), 1307–1319.

(72) Cushen, J.; Wan, L.; Blachut, G.; Maher, M. J.; Albrecht, T. R.; Ellison, C. J.; Willson, C. G.; Ruiz, R. Double-Patterned Sidewall Directed Self-Assembly and Pattern Transfer of Sub-10 Nm PTMSS- b -PMOST. *ACS Appl. Mater. Interfaces* **2015**, *7* (24), 13476–13483.

(73) Ren, J.; Zhou, C.; Chen, X.; Dolejsi, M.; Craig, G. S. W.; Rincon Delgadillo, P. A.; Segal-Peretz, T.; Nealey, P. F. Engineering the Kinetics of Directed Self-Assembly of Block Copolymers toward Fast and Defect-Free Assembly. *ACS Appl. Mater. Interfaces* **2018**, *10* (27), 23414–23423.

(74) Thurn-Albrecht, T.; Schotter, J.; Kastle, G. A.; Emley, N.; Shibauchi, T.; Krusin-Elbaum, L.; Guarini, K.; Black, C. T.; Tuominen, M. T.; Russell, T. P. Ultrahigh-Density Nanowire Arrays Grown in Self-Assembled Diblock Copolymer Templates. *Science (80-.).* **2000**, *290* (5499), 2126–2129.

(75) Muramatsu, M. Nanopatterning of Diblock Copolymer Directed Self-Assembly Lithography with Wet Development. *J. Micro/Nanolithography, MEMS, MOEMS* **2012**, *11* (3), 031305.

(76) Ting, Y.-H.; Park, S.-M.; Liu, C.-C.; Liu, X.; Himpsel, F. J.; Nealey, P. F.; Wendt, A. E. Plasma Etch Removal of Poly(Methyl Methacrylate) in Block Copolymer Lithography. *J.*

Vac. Sci. Technol. B Microelectron. Nanom. Struct. **2008**, *26* (5), 1684.

(77) Hirai, T.; Leolukman, M.; Liu, C. C.; Han, E.; Kim, Y. J.; Ishida, Y.; Hayakawa, T.; Kakimoto, M.; Nealey, P. F.; Gopalan, P. One-Step Direct-Patterning Template Utilizing Self-Assembly of POSS-Containing Block Copolymers. *Adv. Mater.* **2009**, *21* (43), 4334–4338.

(78) Cheng, J. Y.; Ross, C. A.; Thomas, E. L.; Smith, H. I.; Vancso, G. J. Fabrication of Nanostructures with Long-Range Order Using Block Copolymer Lithography. *Appl. Phys. Lett.* **2002**, *81* (19), 3657–3659.

(79) Cheng, J. Y.; Ross, C. A.; Chan, V. Z.-H.; Thomas, E. L.; Lammertink, R. G. H.; Vancso, G. J. Formation of a Cobalt Magnetic Dot Array via Block Copolymer Lithography. *Adv. Mater.* **2001**, *13* (15), 1174–1178.

(80) Jung, Y. S.; Ross, C. A. Orientation-Controlled Self-Assembled Nanolithography Using a Polystyrene−Polydimethylsiloxane Block Copolymer. *Nano Lett.* **2007**, *7* (7), 2046–2050.

(81) Lane, A. P.; Yang, X.; Maher, M. J.; Blachut, G.; Asano, Y.; Someya, Y.; Mallavarapu, A.; Sirard, S. M.; Ellison, C. J.; Willson, C. G. Directed Self-Assembly and Pattern Transfer of Five Nanometer Block Copolymer Lamellae. *ACS Nano* **2017**, *11* (8), 7656–7665.

(82) Peng, Q.; Tseng, Y.-C.; Darling, S. B.; Elam, J. W. A Route to Nanoscopic Materials via Sequential Infiltration Synthesis on Block Copolymer Templates. *ACS Nano* **2011**, *5* (6), 4600–4606.

(83) Peng, Q.; Tseng, Y.-C.; Darling, S. B.; Elam, J. W. Nanoscopic Patterned Materials with Tunable Dimensions via Atomic Layer Deposition on Block Copolymers. *Adv. Mater.* **2010**, *22* (45), 5129–5133.

(84) Ramanathan, M.; Tseng, Y.-C.; Ariga, K.; Darling, S. B. Emerging Trends in Metal-

Containing Block Copolymers: Synthesis, Self-Assembly, and Nanomanufacturing Applications. *J. Mater. Chem. C* **2013**, *1* (11), 2080.

(85) Tseng, Y.-C.; Peng, Q.; Ocola, L. E.; Czaplewski, D. A.; Elam, J. W.; Darling, S. B. Enhanced Polymeric Lithography Resists via Sequential Infiltration Synthesis. *J. Mater. Chem.* **2011**, *21* (32), 11722.

(86) Segal-Peretz, T.; Winterstein, J.; Doxastakis, M.; Ramírez-Hernández, A.; Biswas, M.; Ren, J.; Suh, H. S.; Darling, S. B.; Liddle, J. A.; Elam, J. W.; et al. Characterizing the Three-Dimensional Structure of Block Copolymers via Sequential Infiltration Synthesis and Scanning Transmission Electron Tomography. *ACS Nano* **2015**, *9* (5), 5333–5347.

(87) Xiong, S.; Chapuis, Y.-A.; Wan, L.; Gao, H.; Li, X.; Ruiz, R.; Nealey, P. F. Directed Self-Assembly of High-Chi Block Copolymer for Nano Fabrication of Bit Patterned Media via Solvent Annealing. *Nanotechnology* **2016**, *27* (41), 415601.

(88) Biswas, M.; Libera, J. A.; Darling, S. B.; Elam, J. W. Kinetics for the Sequential Infiltration Synthesis of Alumina in Poly(Methyl Methacrylate): An Infrared Spectroscopic Study. *J. Phys. Chem. C* **2015**, *119* (26), 14585–14592.

(89) Biswas, M.; Libera, J. A.; Darling, S. B.; Elam, J. W. New Insight into the Mechanism of Sequential Infiltration Synthesis from Infrared Spectroscopy. *Chem. Mater.* **2014**, *26* (21), 6135–6141.

(90) Kim, J. J.; Suh, H. S.; Zhou, C.; Mane, A. U.; Lee, B.; Kim, S.; Emery, J. D.; Elam, J. W.; Nealey, P. F.; Fenter, P.; et al. Mechanistic Understanding of Tungsten Oxide In-Plane Nanostructure Growth via Sequential Infiltration Synthesis. *Nanoscale* **2018**, *10* (7), 3469–3479.

CHAPTER 2: FABRICATION OF NANOPOROUS ALUMINA ULTRA-FILTRATION MEMBRANE WITH TUNABLE PORE SIZE USING BLOCK COPOLYMER TEMPLATES

2.1 Abstract

Control over nanopores size and three-dimensional structure is necessary to advance membrane performance in ubiquitous separation devices. Here, inorganic nanoporous membranes are fabricated by combining the assembly of cylinder-forming PS-*b*-PMMA (poly(styrene-*block*-methyl methacrylate)) block copolymer and sequential infiltration synthesis (SIS). A key advance relates to the use of PMMA majority block copolymer films and the optimization of thermal annealing temperature and substrate chemistry to achieve through-film vertical PS cylinders. The resulting morphology allows for direct fabrication of nanoporous AlO_x by selective growth of Al_2O_3 in the PMMA matrix during the SIS process, followed by polymer removal using oxygen plasma. Control over the pore diameter is achieved by varying the number of Al_2O_3 growth cycles, leading to pore size reduction from 21 nm to 16 nm. Three-dimensional characterization, using TEM tomography, reveals that the AlO_x channels are continuous through the film and have a gradual increase in pore size with depth. Finally, we demonstrate the ultrafiltration performance of the fabricated AlO_x membrane for protein separation as a function of protein size and charge.

2.2 Introduction

Nanoporous membranes with uniform pore size have gained growing interest in the last decade since they enable separations at the micro- and nano- scale in water filtration, molecular sorting, drug delivery, and molecular sensing applications.[1–6] The performance of nanoporous membranes or ultrafiltration (UF) membranes depends on several critical properties: high selectivity is achieved by tailoring the pore size and obtaining narrow pore distribution, while high flux can be

achieved by high porosity, non-tortuous pathways, and high pressure gradient across the membrane.[4,7] Common commercial nanoporous membranes, like polymeric UF membranes, generally exhibit random structure pores, tortuous pore paths, wide pore size distribution, and are relatively thick.[4,6] Recently, high density porous arrays of inorganic and hybrid organic-inorganic materials were demonstrated using a variety of nanofabrication techniques such as focused ion and electron beams[7,8] and rapid thermal annealing of nanocrystalline silicon.[9,10] However, most of these methods are suitable for small scale fabrication while separation processes typically require large areas. Block copolymers (BCPs), on the other hand, are easily processed from solutions and are amenable to the large-scale roll-to-roll fabrication[11,12], offering a simple and scalable solution for membrane fabrication.

BCPs have been widely used to generate templates and scaffolds for fabrication of nanostructured materials, as chemically dissimilar polymer chains covalently linked together self-assemble into periodic arrays of lamellar, cylindrical, spherical, and gyroid morphologies with characteristic feature sizes of 5-50 nm.[13] To create membranes with high pore densities, cylinder-forming BCPs are typically used, and porosity is obtained either by selectively removing one block by post-assembly etching processes,[14–16] or by using non-solvent induced phase separation.[17,18] Previous studies have demonstrated the ability to fabricate nanoporous membranes with well-ordered pores, narrow pore size distribution, and high pore density using self-assembled BCPs.[2,14–16,19–22] However, tuning the pore size to create size selectivity by design is still a major challenge in the field. An additional challenge in polymeric and BCP membranes is the membranes' high fouling tendency that occurs due to the inherent hydrophobicity of polymers.[10] On the other hand, inorganic membranes, such as anodic aluminum oxide (AAO) membranes and titanium dioxide

membranes, exhibit attractive thermal, chemical, and mechanical stability, greater fouling-resistance, and often photocatalytic ability.[10]

Recently, sequential infiltration synthesis (SIS), a technique derived from atomic layer deposition (ALD), has been developed to selectively grow inorganic species (such as ZnO, TiO_2 and Al_2O_3) in polymers that contain polar moieties, enabling inorganic nanostructures fabrication from polymer and BCP templates.[23–27] The SIS process is based on the selective binding of gaseous organometallic precursors to polar moieties,[28] which produces a hybrid organic-inorganic composite. Subsequent polymer removal results in inorganic nanostructures templated by the original block copolymer morphology. SIS has been demonstrated to significantly enhance etch contrast in BCP lithography, enable fabrication of high aspect ratio inorganic nanostructure, as well as enhance *Z* contrast for STEM imaging and tomography of BCP films.[24,29–33]

In this work, we harness Al_2O_3 SIS to fabricate highly ordered, isoporous, AlO_x membranes with tunable pore size, templated by BCP self-assembly, and demonstrate the selectivity capabilities of this membrane through charge-based separation of similarly sized proteins. Self-assembled films of cylinder-forming poly(styrene-*block*-methyl methacrylate) (PS-*b*-PMMA) with PS cylinders in PMMA matrix were used to template the AlO_x membranes. The assembly was tuned through careful control of boundary conditions to create perpendicular PS cylinders for templating non-tortuous membranes. The templating of AlO_x membrane from BCP film was characterized through a combination of scanning electron microscopy (SEM), grazing incident small angle X-ray (GISAXS), and transmission electron microscopy (TEM) tomography, giving detailed description of the AlO_x membrane and its three-dimensional morphology. With the additional degrees of freedom that the SIS process provides, we varied the AlO_x membrane pore diameter between 21 nm and 16 nm, using a single BCP template. Finally, the thin AlO_x membrane

was combined with a supporting anodic aluminum oxide (AAO) membrane to create mechanically robust hierarchical AlO_x/AAO membrane. Utilizing the pH-responsive surface charge of metal oxides, we efficiently separated similarly sized proteins with both high selectivity and high flux using the hierarchical membrane.

2.3 Experimental Section

2.3.1 Materials

Cylinder-forming polystyrene-block-poly(methyl methacrylate) (PS-*b*-PMMA, C2050, M_n = 20.2-50.5 kg/mol, PDI = 1.07) was purchased from Polymer Source, Inc. Poly(acrylic acid) sodium salt solution ($M_w \approx$ 15000 g/mol, 35% mass fraction in water) was purchased from Sigma-Aldrich and used as received. Poly(styrene-co-methylmethacrylate-co-glycidyl methacrylate) (PS-*r*-PMMA-PGMA) containing ~ 4 mol % of glycidyl methacrylate was synthesized by reversible addition fragmentation chain transfer (RAFT) polymerization with styrene mole fractions from 21 to 85% (denoted as 21S to 85S) determined by 1H nuclear magnetic resonance spectroscopy. Anodic aluminum oxide membranes (Anopore) were purchased from Sigma-Aldrich (20 nm and 100 nm pore size membranes with 60 um thickness). Bovine serum albumin (66 kDa) and bovine hemoglobin (65 kDa) were purchased from Sigma-Aldrich and used as received. The buffer powder for phosphate buffered saline (PBS) was purchased from Sigma-Aldrich (catalog no. P3563). The pH values of the buffer solutions were tuned to 4.7 and 7.0 by adding a small amount of HCl or NaOH solution.

2.3.2 Sample preparation

Silicon wafers were cleaned in a piranha solution (3:7 volumetric ration of concentrated sulfuric acid and 30 wt% hydrogen peroxide solution) at 130 °C for 30 min and rinsed with deionized water prior to use. PS-*r*-PMMA-modified substrates were prepared by spincoating 1 wt% of 21S to 85S

in toluene solution onto the cleaned Si wafer at 4000 rpm for 1 min, followed by annealing at 250 °C for 30 min under a nitrogen atmosphere to be fully crosslinked. C2050 films with thickness ranging from 22 nm to 401 nm were deposited from chlorobenzene solutions with concentrations of 1-8 wt% on the PS-*r*-PMMA-modified substrates. Samples were annealed at 190 to 270 °C for 30 min to 3 h under a nitrogen atmosphere. Al_2O_3 SIS was performed in Arradiance Gemstar ALD using alternating exposures to TMA and deionized H_2O at 95 °C in semistatic mode. N_2 gas flow was used as purge and as carrier gas. The base pressure of the reactor was 50 mTorr before introducing the precursors. During each setting exposure period, the TMA valve was opened for 1 s, after which the valve was closed, and the samples were exposed for 10 min, and then pure N_2 gas was flowed through the chamber at 200 sccm for 5 min to purge any unreacted precursor. A same exposure/purge process was used for the H_2O precursor to complete one SIS cycle. The long exposure time was chosen to ensure the precursors can diffuse through the entire thickness of the film. The SIS cycle number was varied between 2 and 5. The polymers were etched with O_2 Reactive Ion Etching (RIE) using Oxford Plasma-Pro NGP80. The samples were etched at 50 W (RF power) for 5 min to make sure polymers were removed thoroughly. Film thickness was measured using an alpha-SE ellipsometry.

2.3.3 Membrane fabrication

Silicon wafers were piranha cleaned with same procedure. About 100 nm thick water soluble sacrifice layers were prepared by spin coating 5 wt% poly(acrylic acid) sodium salt (PAA-Na) in water at 4000 rpm for 90 s. 63S was spin-cast from a 1 wt% toluene solution and followed by annealing at 250 °C for 30 min under a nitrogen atmosphere to function as surface neutral layer. C2050 films with thickness of 141 nm were spin-cast from chlorobenzene solutions with concentrations of 4 wt% on the silicon-PAA-mat substrates. Samples were annealed at 270 °C for

3 h under a nitrogen atmosphere. The BCP film and mat were floated using deionized water and transferred onto the commercial AAO supporting membrane, followed by SIS and O_2 RIE as previously described. While the SIS process results in growth of Al_2O_3 also inside the polymer mat,[30] this non-structured thin layer is not mechanically stable to be a stand-alone layer and porosity is achieved without breakthrough Al_2O_3 etch.

For TEM imaging samples, the BCP film and mat were floated and collected with a silicon nitride supporting film (200 μm silicon frame, 30 nm silicon nitride supporting film).[33–35] The same SIS and etching recipes were applied to TEM samples.

2.3.4 Metrology

A Carl Zeiss Merlin field-emission scanning electronic microscopy (SEM) was used to investigate the surface morphology with an acceleration voltage of 1 keV and a typical working distance of 3 mm. STEM imaging and tomography was performed using a field-emission gun TEM operated at 200 kV, and camera length of 300 mm. For tomography, a series of STEM images were acquired at tilt angles ranging from -68° to +68° at angular interval of 3° from -54° to +54°, and at angular interval of 2° from +54° to +68° and from -54° to -68°. The tilt series of the STEM images (51 projections) were aligned with Inspect 3D® software using naturally occurring defects in the film. Reconstruction was performed using simultaneous iterative reconstruction technique (SIRT) algorithm applied through the same software. Segmentation (thresholding) of the reconstructed volume was performed manually using ImageJ to define the alumina domains for surface rendering. Visualization of the segmented volume was performed using Amira® software. Pore size analysis was performed using watershed segmentation algorithm implemented in a python script. Pore diameter was measured as the diameter of a circle with the same area as the segmented pore. Grazing-incidence small-angle scattering (GISAXS) measurements were

performed at beamline 8-ID-E of the Advanced Photon Source at Argonne National Laboratory. The X-ray energy was 7.35 keV, the wavelength was 1.69 nm, and the sample to detector distance was 1.30 m. The exposure time to collect each scattering measurement was 1 second. Sets of 30 scattering measurements were collected and integrated to produce each 2D scattering profile.

2.3.5 Protein Transport and Separation

Protein separation was probed in a custom-made U-shape diffusion cell. Membranes were sandwiched between two glass slides with a hole and two rubber O-rings and clamped between glass fittings. The effective permeation area of the all membranes was 0.45 cm^2. Fifteen milliliters of a 0.01 M buffer solutions were placed into the source (including a mixture of 25μM BSA and 25μM BHb) and sink chambers. The value of the electrical double layer thickness is given by

$$\lambda_D = (8\pi n_0 \lambda_B)^{-1/2}$$

where the ion density n_0 is ~0.006 for 0.01 M buffer solutions and λ_B is ~0.7 nm in water. [21,36] Both compartments were stirred vigorously with magnetic stirrers to ensure homogenic solutions. One milliliter was taken every 60 min from both the sink and the source sides, and the solute concentrations in the sink side were quantified by UV-visible spectroscopy (Agilent 8453), using the absorption band at 278 nm for BSA and at 408 nm for BHb.

2.4 Results and Discussion

The fabrication process of BCP-templated AlO_x membrane is illustrated in Figure 2-1. A silicon wafer coated with a ~100 nm thick water-soluble sodium salt of poly(acrylic) acid (PAA-Na) layer was used as a substrate. The substrate chemistry was modified and controlled by depositing a 10 nm thick random copolymer mat with varied PS content. Cylinder-forming PS-*b*-PMMA (C2050) films (M_n = 20.2-*b*-50.5 kg/mol, center to center spacing- L_0 = 38.3 nm) were self-assembled on the random copolymer mat at various thicknesses. The polymer films were floated in deionized

water and were transferred onto 60 μm thick AAO membranes with average pore size of 100 nm. Al_2O_3 SIS was performed directly on the hierarchical BCP/AAO membrane, selectively growing Al_2O_3 in the PMMA domains. Finally, the membrane samples were exposed to oxygen plasma to remove polymer components generating ultrathin highly ordered porous AlO_x membranes on AAO support.

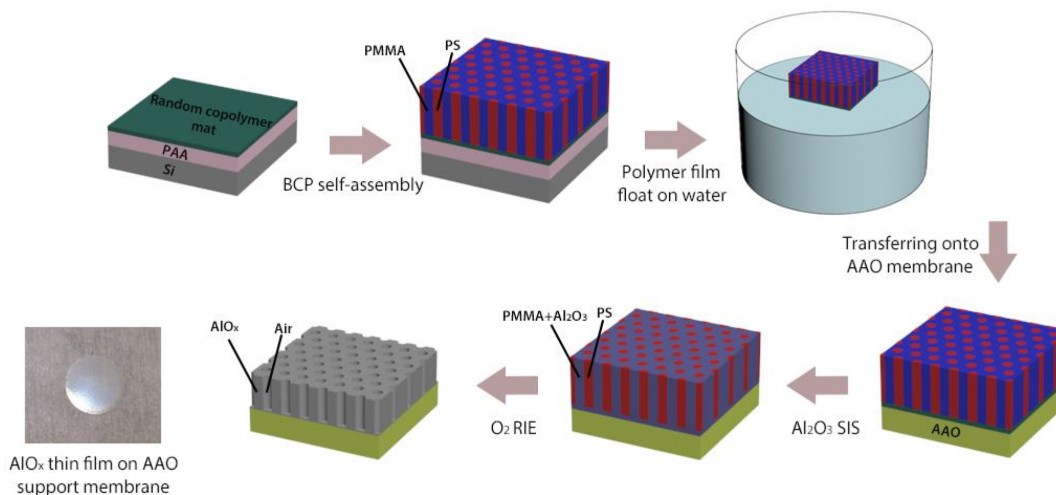

Figure 2-1: Schematic illustration of BCP-templated AlO_x membrane fabrication process. PS-*b*-PMMA (C2050) BCP films were self-assembled on a random copolymer mat on top of a water-soluble PAA-Na layer. The BCP and the random copolymer films were floated off in water and transferred onto AAO membranes. The polymer film was treated with Al_2O_3 SIS to selectively grow Al_2O_3 within the PMMA microdomains. After the reaction, the samples were etched by oxygen plasma to remove the polymer, resulting in nanoporous AlO_x membrane.

2.4.1 Self-assembly Study of Cylinder Forming PS-*b*-PMMA with PS cylinders

For utilizing BCP films as separation membranes, it is desired to induce the assembly of perpendicular-oriented cylinders due to their high density and direct pathway through the film. While the assembly of cylinder-forming poly(styrene-*block*-methyl methacrylate) (PS-*b*-PMMA) with PMMA cylinders is well documented,[37–41] less is known about PS-*b*-PMMA with PS cylinders assembly. Han *et al.* reported non-preferential brush and mat chemistries that can generate perpendicular-oriented PS cylinders in extremely thin C2050 films (BCP thickness of

~0.5 L_0).[42] However, these conditions were not sufficient to induce perpendicular orientation in films thicker than 0.5 L_0. To rigorously study PS cylinder assembly in PS-*b*-PMMA films and to identify the thermodynamically favorable boundary conditions to achieve the desired orientation, the effects of the substrate chemistry and the annealing temperature on the domain orientation in C2050 thin films (~0.8 L_0) were investigated using top-down SEM imaging (Figure 2). Silicon wafers coated with the crosslinked polystyrene-*random*-poly(methyl methacrylate) mats with different styrene mole fractions F_{St} (ranging from 0.21 to 0.85, 21S-85S) were used as substrates. The thermal annealing temperature, T, was varied between 190-270 °C, and the films were annealed for 30 min.

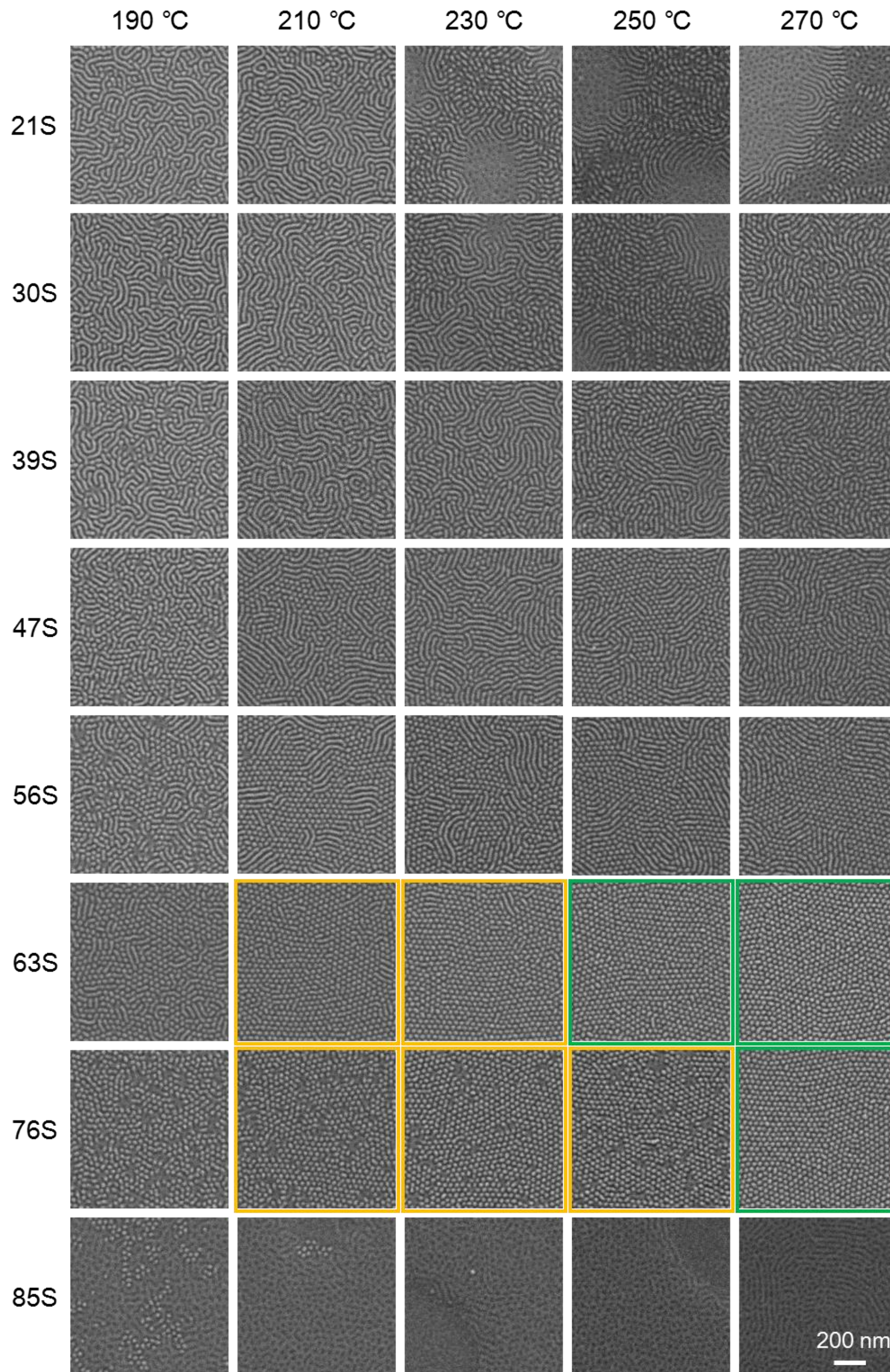

Figure 2-2: Top-down SEM images of 30 nm (0.8 L_0) thick C2050 films on chemically modified substrates containing different mole fractions of styrene and annealed at various temperatures. Green and yellow colors indicate defect-free perpendicular PS cylinders in PMMA matrix, and nearly defect-free perpendicular cylinders with few defects around grain boundaries, respectively.

On F_{St} mats 21S-63S, the surface morphology progressed from parallel cylinders to perpendicular cylinders with increasing F_{St}, and vertical cylinders were observed when F_{St} was around 0.63. As F_{St} was increased above 0.63, the area fraction of vertically oriented structures decreased, and perpendicular cylinders formed only over small areas on 85S. Even for films assembled on 63S, and in particular for temperatures below 230 °C, non-perfect morphologies were observed with some bridging between adjacent cylinders, in agreement with previous work conducted at 190 °C.[42]

Since the annealing temperature also plays an important role in modulating the domain orientation, the effect of the annealing temperature was studied. When the substrate composition induced perpendicular morphology ($0.56 \leq F_{St} \leq 0.73$), a wider perpendicular process window was observed with an increase in the annealing temperature. While at 190 °C, only at $F_{St} = 0.63$ a majority of vertically oriented structures was observed, at 270 °C, C2050 assembled into vertically oriented structures between $0.56 \leq F_{St} \leq 0.73$. In addition, the number of parallel defects decreased when the annealing temperature was increased from 190 °C to 270 °C.

Self-assembly behavior of a BCP film is governed by the interfacial interactions both at the bottom and top of a film. Thus, the annealing temperature that affects the surface energy of PS and PMMA (γ_s and γ_m, respectively) is as critical as the surface chemistry of substrate to achieve the targeted BCP orientation. γ_s and γ_m become nearly equal at 250 ºC which is considered to be the optimized annealing temperature for symmetric lamella forming PS-*b*-PMMA films.[43,44] However, in perpendicular orientation of C2050, larger PMMA fraction is exposed at the free surface compared with symmetric lamella forming PS-*b*-PMMA films; thus, conditions for slightly PMMA preferential free surface are desired. At 270ºC, γ_m becomes lower than γ_s, yielding a more stable free surface for this asymmetric PS-*b*-PMMA film and leading to defect-free perpendicular

PS cylinders as was seen by top-down SEM in Figure 2-2 (63S and 73S). For comparison, the optimized annealing temperatures for PMMA cylinders in the PS matrix (C4621, M_n = 46-*b*-21 kg/mol) were reported as 210ºC - 230ºC at which the free surface is slightly PS preferential.[39,41] It is important to note that the annealing temperature also plays a role in the nucleation at free surface and in the pattern coarsening dynamics.[39,45] Faster coarsening dynamics could be an additional reason for better defined cylinders formed in the high temperature regime. As shown in Figure 2-2, optimization of annealing temperature in combination with fine turning of substrate chemistry enabled us to achieve desired perpendicular PS cylinders in the PMMA matrix.

To maintain the mechanical strength of BCP and AlO_x membranes, it is desirable to use semi-thick block copolymer films as templates (thickness >100 nm). To examine the film morphology as a function of thickness, three sets of C2050 films with thickness ranging from 20 nm to 401 nm were compared and the surface morphologies of films were imaged after annealing at 270 °C for 3 hours (Figure 2-3). The high temperature which was chosen to induce perpendicular morphology in C2050 also facilitates rapid assembly of BCP films. Therefore, we assumed that the BCP films have reached close to equilibrium state in 3 hours. On 63S modified silicon substrates which were shown to be a non-preferential substrate for C2050 thin films (Figure 2-2), high-degree of perpendicular structures were obtained in most of the film thicknesses. Such thickness-independent orientation indicates that both the bottom and top surfaces of BCP films are non-preferential.[46,47] In addition, the grain size increased with the film thickness, in agreement with Ji *et al.*'s study on cylinder-forming PS-*b*-PMMA with PMMA cylinders (C4621, M_n = 46-21 kg/mol).[41]

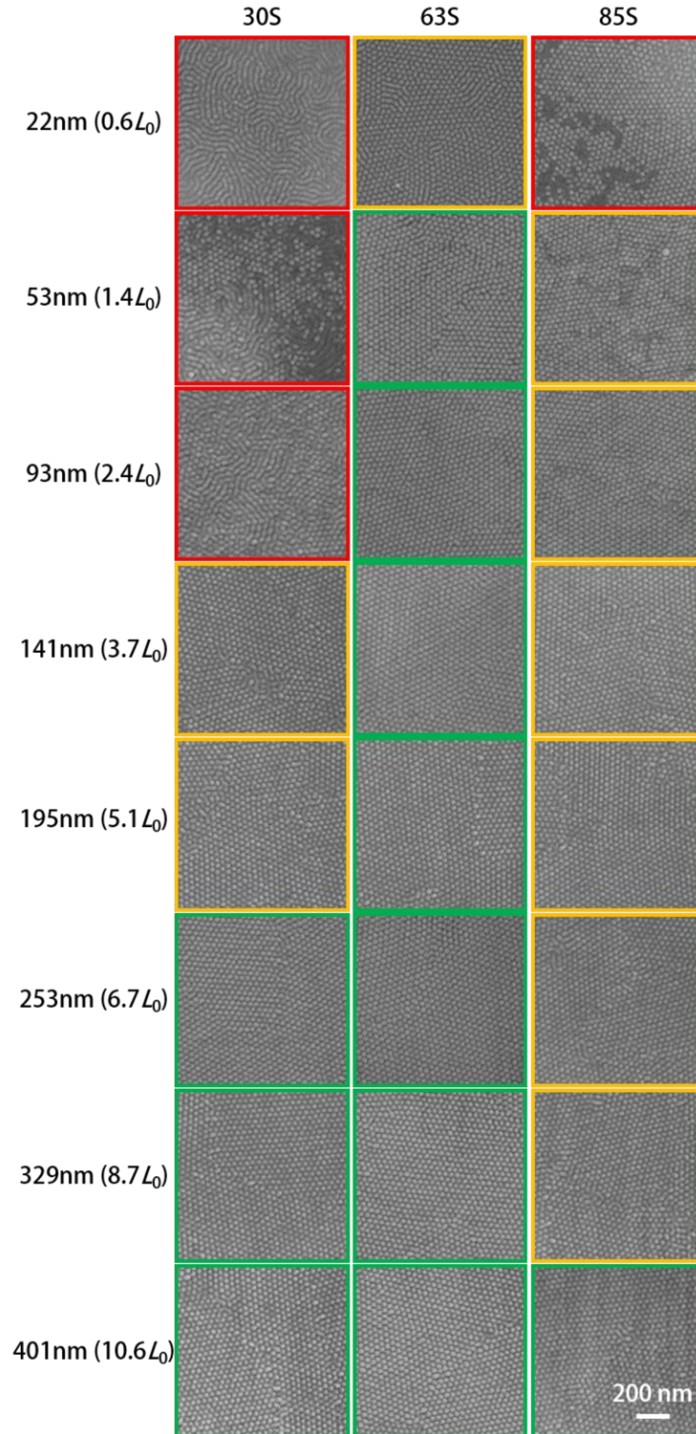

Figure 2-3: Top-down SEM images of C2050 films with different thickness on 30S, 63S and 85S. Samples were annealed at 270 °C for 3 h under a nitrogen atmosphere. Green, yellow and red colors indicate defect-free perpendicular PS cylinders in PMMA matrix, PS cylinders with defects around the grain boundaries, and other morphologies, respectively.

On 30S and 85S modified substrates, different behavior was observed compared with films assembled on 63S. In films thinner than 141 nm for 30S and 93 nm for 85S, the films exhibited various morphologies including hole/island, hexagonally perforated lamellae, and parallel cylinder, rather than perpendicular hexagonally packed cylinders. On the other hand, films thicker than 141 nm (on 30S) and thicker than 93 nm (on 85S) showed perpendicular morphology with only few parallel defects at the top surface, similarly to what was observed in films assembled on 63S.

The change in coupling between the mat chemistry and surface morphology at the various thicknesses reveals the effect of boundary conditions on surface morphology in semi-thick films. At thickness smaller than ~ 100 nm, the polymer-substrate boundary condition dominates the assembly and determines the domain orientation of the block copolymer throughout the film thickness. At thicknesses above ~ 100 nm, on the other hand, the polymer-substrate and polymer-free surface boundary condition are decoupled, and the polymer-free surface interaction determines the domain orientation of cylinders near the film surface regardless of the chemistry of the underlying substrate. This decoupling of boundary conditions in thick BCP films is in good agreement with previous reports on other cylinder forming BCP.[39,41]

To utilize BCP films as templates for inorganic membranes it is important to have perpendicular cylindrical domains through the entire film thickness that would lead to membranes with high connectivity and direct pathways. Non-preferential boundaries are necessary but not sufficient condition to ensure through-film continues cylinders; at thick and semi-thick films, non-coupled nucleation occurs simultaneously at the substrate and at the free surface, which could result in non-continuous perpendicular cylinders even when perpendicular assembly occurs at both interfaces.[39,41,45] In order to ensure continuous PS cylinders and template thin AlO_x membrane that would enable high flux, the BCP film thickness was selected to be 141 nm and 63S was selected

as the mat chemistry. The good assembly of C2050 film was demonstrated in lower magnification SEM image shown in Figure 2-4. The continuity of cylinder channels will be further discussed in sections 2.4.2 and 2.4.3.

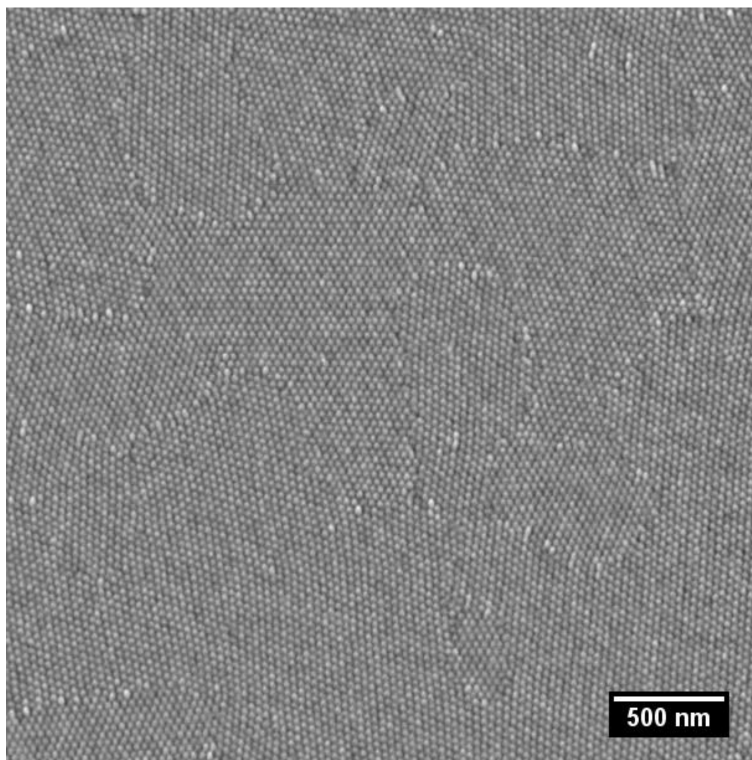

Figure 2-4: Top down SEM images of 141 nm thick C2050 BCP film self-assembled on 63S mat. The sample was annealed at 270 °C for 3 h under a nitrogen atmosphere.

2.4.2 BCP-templated AlO_x membrane

To fabricate the BCP-templated AlO_x membranes, Al_2O_3 SIS was performed using multiple trimethylaluminum/water (TMA/H_2O) exposure cycles followed by oxygen plasma to remove the polymer (see experimental section for details). Figure 2-5 shows the morphology of the BCP film, the hybrid BCP-Al_2O_3 nanostructure after 3 cycles of TMA/H_2O SIS, and the nanoporous AlO_x membrane after oxygen plasma etching, using both SEM imaging (Figure 2-5(a)) and GISAXS (Figure 2-5(b)). SEM images show that the hexagonal morphology at the surface was maintained during SIS and plasma etch processes and the Al_2O_3 growth occurred primarily in the PMMA

domains, in agreement with previous SIS studies.[25,26] The AlO_x membrane showed mostly cylindrical pores with few short openings caused by merging and splitting of cylinder domains around grain boundaries, and large scale defects were not observed (Figure 2-6). To analyze the ordering through the entire film thickness, films were characterized by GISAXS; the incidence angle α_i between the X-ray and the film's surface was set to 0.200°, above the critical angle of the BCP. For all three samples, multiple strong vertical peaks were present only in the q_y direction, corresponding to perpendicularly-oriented domains. Four intense multiple-order Bragg-rod peaks at scattering vector ratios of $q/q^* = 1{:}\sqrt{3}{:}\sqrt{4}{:}\sqrt{7}$, as shown in Figure 2-5(c), indicated hexagonal packing in all three samples, in agreement with the SEM results (Figure 2-5(a)). The average center-to-center distance in the plane of films, measured from the peak position of first four peaks, was 38.3 nm for all samples, confirming that the SIS and the etch process did not change the lateral structure and that the AlO_x membrane was indeed templated by the BCP film. Additionally, the absent of diffuse elliptical scattering (Debye-Scherrer ring), which corresponds to tilted or randomly oriented domains[48,49] supports the formation of vertically oriented cylinders throughout the film. While the periodicity was maintained through the processes, the number of high order peaks in the GISAXS significantly differs between the samples; the hybrid BCP-Al_2O_3 had an additional high order diffraction peak compared with the pristine BCP film, while the AlO_x nanostructure had as many as ten diffraction peaks, highlighting the long-range order of the AlO_x membrane. The increase in high order peaks originates from the increase in X-ray scattering contrast with Al_2O_3 incorporated in PMMA domains and between AlO_x and air in the nanoporous AlO_x structure formed after the oxygen etching.

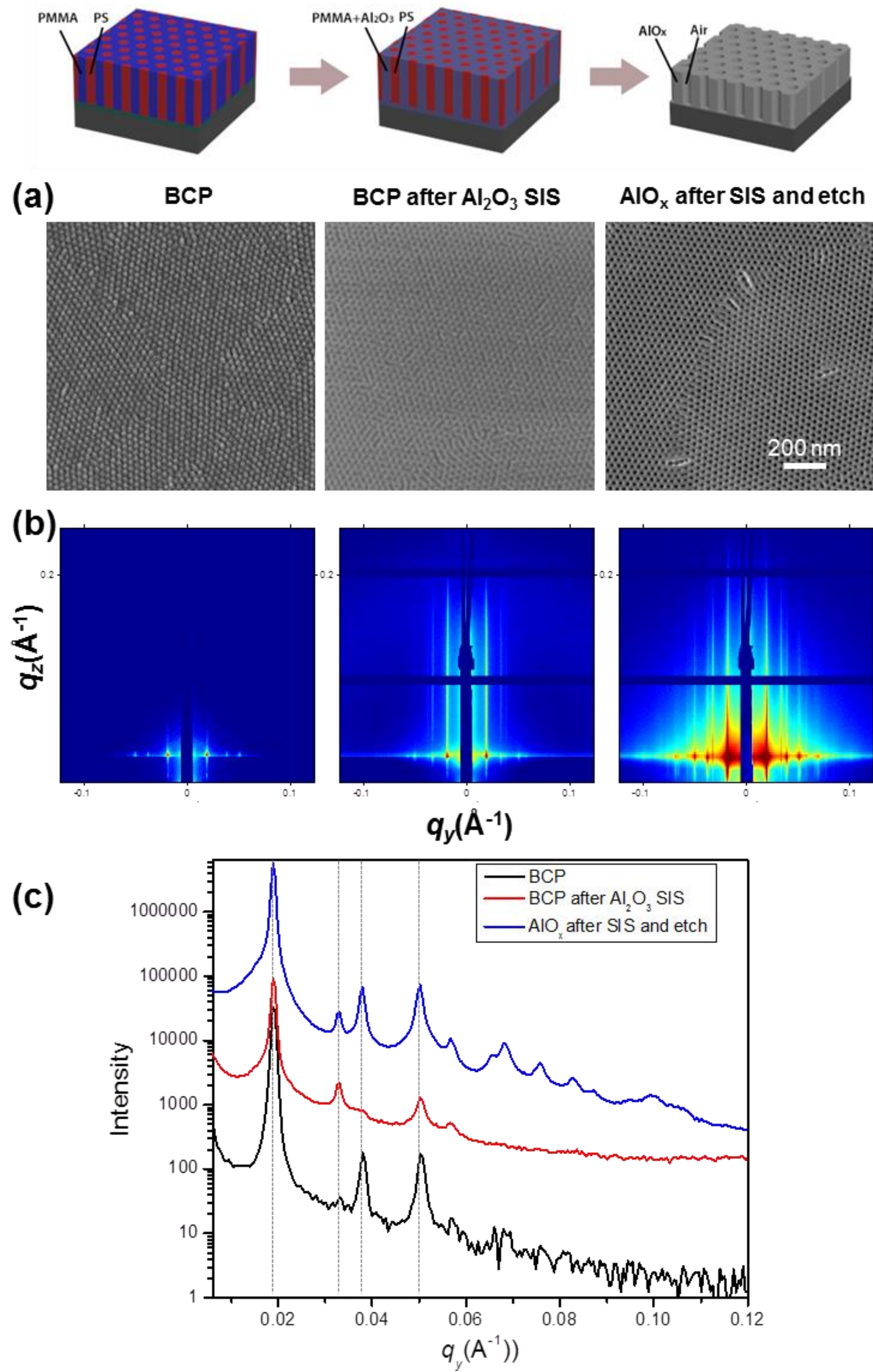

Figure 2-5: (a) SEM images of 141 nm thick C2050 BCP film, BCP film treated with 3 TMA/H_2O cycles of SIS, and nanoporous AlO_x structure formed after O_2 etching. (b) Corresponding GISAXS scattering pattern at incident angle $\alpha_i = 0.200^{\circ}$. (c) Line intensity scanned along the in-plane direction around Yoneda peak *vs.* q_y

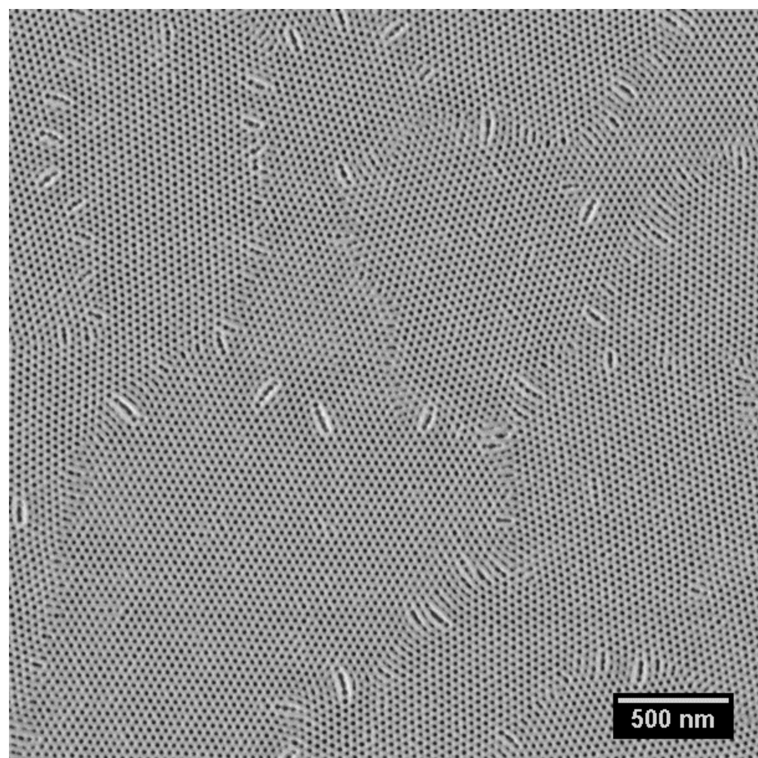

Figure 2-6: Top down SEM image of AlO_x membranes templated by 141 nm thick C2050 film using 3 cycles of TMA/H_2O SIS.

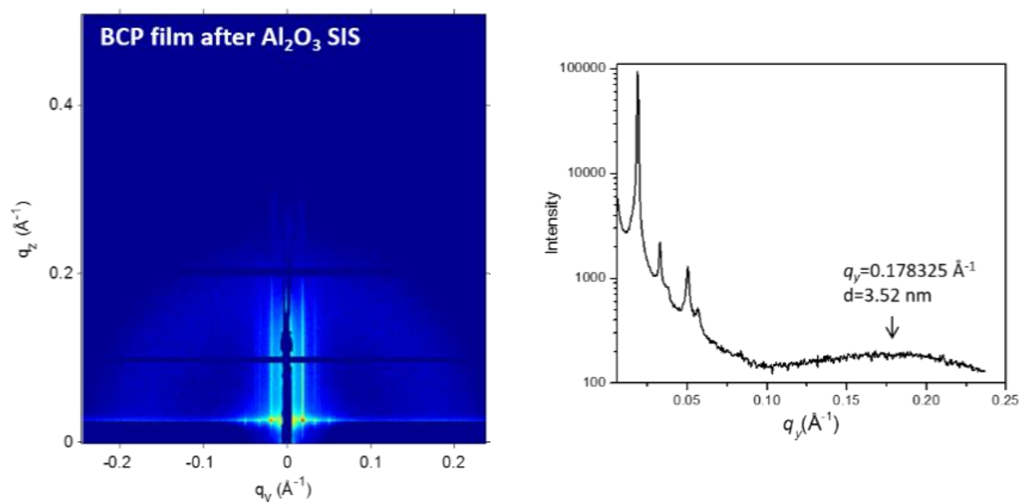

Figure 2-7: The full range of GISAXS scattering pattern for 141 nm thick C2050 BCP film after three Al_2O_3 SIS cycles and the corresponding line intensity profile vs. q_y. The hump observed in the high q range indicates that the Al_2O_3 particles formed during the SIS have weak ordering with average spacing around 3.52 nm.

Analysis of the GISAXS data also reveals a hump in the high q range of the hybrid BCP-Al_2O_3 film scattering pattern, (Figure 2-7). This hump was not observed in the nanoporous AlO_x structure formed after oxygen etching. We hypothesize that the Al_2O_3 particles formed during the SIS process have weak ordering with average spacing of ~ 3.5 nm, while the AlO_x in the porous membrane is closely packed. This observation is in good agreement with previous reports on the dimension shrinkage during post-SIS etch process. [30,50] Detailed distribution of inorganic nanoparticles during SIS process is under ongoing investigation.

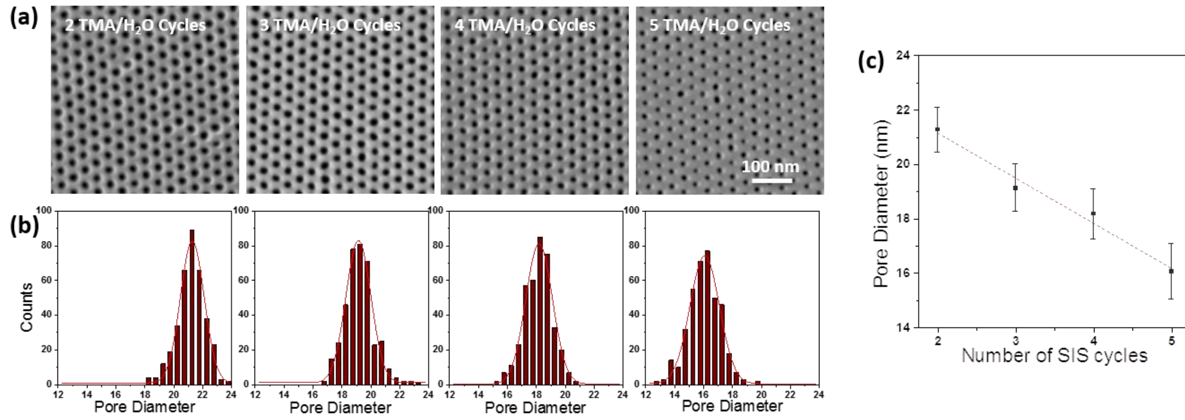

Figure 2-8: Pore size tuning through SIS cycles: (a) SEM images of AlO_x membranes templated by 141 nm thick C2050 film using 2, 3, 4, and 5 cycles of TMA/H_2O SIS, followed by oxygen plasma etch. (b) Pore size distribution calculated from ~ 240 pores. (c) Pore diameter as a function of cycle number.

Table 2-1: Average pore diameter, standard deviation, and open area fraction of AlO_x membranes templated by 141 nm thick C2050 film using various cycles of TMA/H_2O SIS, followed by oxygen plasma etch. The measurements were done using SEM images, 700 nm × 700 nm in size, with ~ 240 pores.

Number of SIS cycles	Average pore diameter (nm)	STD (1 σ)	Open area fraction (*f*)
2	21.3	0.8	0.280
3	19.1	0.9	0.226
4	18.2	0.9	0.205
5	16.1	1.0	0.160

To investigate the pore-size tunability, 141 nm thick BCP films assembled on 63S modified substrates were treated with various number of TMA/H_2O cycles followed by oxygen plasma etching. Increasing the number of SIS cycles resulted in hexagonally packed pores with decreasing pore sizes, as shown by top-view SEM imaging (Figure 2-8). The average pore diameters at the film surface were 21.3 ± 0.8 nm, 19.1 ± 0.9, 18.2 ± 0.9, and 16.1 ± 1.0 nm when BCP films were exposed to 2, 3, 4, and 5 TMA/H_2O cycles, respectively (Figure 2-8 and Table 2-1); the corresponding open area fractions f are listed in Table 2-1. The pore size was linearly dependent on the number of SIS cycles (Figure 2-8(c)), but as the average pore diameter decreased, the pore size distribution gradually became wider.

The decrease in pore size is the result of higher Al_2O_3 content in the PMMA domain with additional cycles which leads to thicker AlO_x matrix after oxygen etching. The Al_2O_3 growth at the surface becomes less uniform with additional cycles, as evident from the increase in standard deviation with cycles. However, since Al_2O_3 growth in SIS occurs throughout the film thickness, a more thorough inspection of the three-dimensional structure is needed to fully understand the growth of Al_2O_3 with SIS cycles. By controlling the growth of Al_2O_3 in the BCP we were able to decrease the pore size by ~ 25 %, demonstrating the ability to tune the pore size from a single BCP template. Further decrease in pore size can be conducted using additional SIS cycles or ALD coatings.

2.4.3 The three-dimensional structure of AlO_x membranes

While the pore size at the membrane surface is an important factor, the membrane performance is determined by its entire three-dimensional (3D) structure. In order to probe the pores' 3D morphology and verify that the cylinder channels are indeed continuous throughout the entire membrane thickness, scanning transmission electron microscopy (STEM) tomography[33] was used

to directly resolve the 3D structures of the membrane with high resolution. For STEM imaging, 141 nm thick BCP film assembled on 63S modified substrate was floated (together with the random copolymer layer) onto deionized water and was transferred onto a silicon nitride window,[35] followed by Al_2O_3 SIS and O_2 etch under the same conditions previously described.

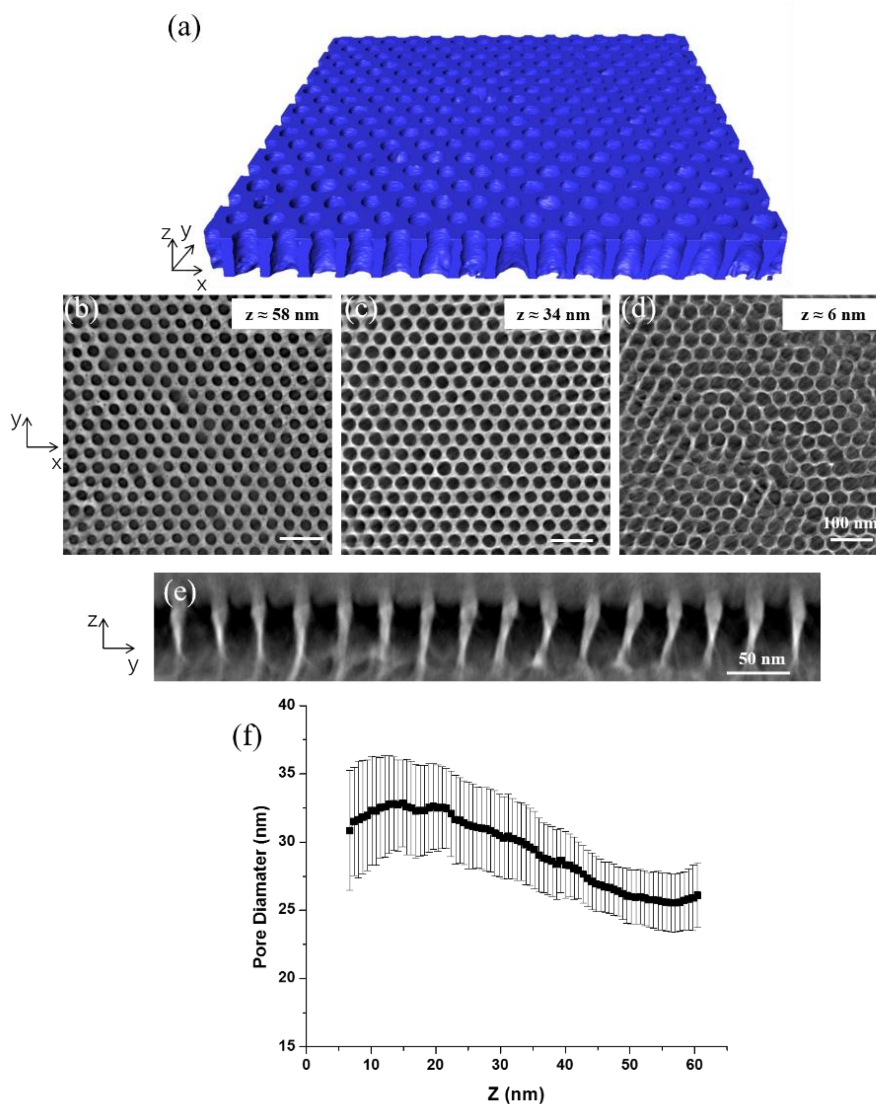

Figure 2-9: STEM tomography characterization of alumina membrane templated by **C2050** using 3 cycles of AlO_x SIS followed by polymer etch: (a) visualization of the reconstructed volume; the dimensions of the reconstructed volume are 635 nm, 612 nm, and 62 nm (x,y,z). (b-d) 0.68 nm thick, *xy* slices of the reconstructed volume at z high of 6 nm, 34 nm, and 58 nm, respectively. $z = 0$ is defined as the height at the SiN_x substrate. (e) *yz* digitally sliced cross section of the reconstructed volume. (f) Pore diameter as a function of depth.

Visualization of the 3D reconstructed volume of AlO_x membrane prepared using 3 SIS cycles, obtained by angular dark field (ADF) STEM tomography, is shown in Figure 2-9(a); for clarity, the AlO_x is colored in blue and the pores are transparent. To better understand the pores structure, the reconstructed volume was digitally sliced in *xy* and *yz* planes, creating slices parallel and perpendicular to the subatrate, respectively. Figures 2-9 (b-d) show 0.68 nm thick *xy* slices taken at the top, middle and bottom of the film ($z \approx 58$ nm, $z \approx 34$ nm, and $z \approx 6$ nm, respectively, where $z \approx 0$ nm is the SiN_x substrate). The bright regions in the ADF-STEM images are the strong scattering AlO_x, while the darker regions are the pores. The *xy* slices show perpendicular pores throughout the AlO_x thickness with some decrease in perpendicularity at the bottom of the membrane (Figure 2-9(d)). The tomographic characterization indicates that the original BCP film, which templated the AlO_x membrane, had perpendicular-oriented PS cylinders in the entire film thickness, in good agreement with the GISAXS characterization results (Figure 2-6). The perpendicularity of the pores can also be clearly seen in the cross sectional *yz* slice (Figure 2-9(e)). The AlO_x membrane thickness, measured from the *yz* slices, was ~ 62 nm; i.e., the film shrunk in z direction by 56% during etching, similar to recent studies on ZnO, AlO_x, and TiO_x nanostructures formed by SIS in polymers.[23,51]

Figures 2-9(b-e) show that the pore size changes as a function of depth and the sidewalls become thinner at smaller *z*. To analyze the change in pore size with depth, the average pore diameter of 240 pores was measured in each *xy* slice of the tomography reconstructed volume using watershed segmentation and the pore diameter was plotted as a function of *z* (Figure 2-9(f)). Close to the surface ($z = 60$ nm), average pore size of 26.1 ± 2.4 nm was measured, with minor change in diameter until $z = 50$ nm. Below $z = 50$ nm, the pore size gradually increased towards the substrate (until $z = 20$ nm), where at the bottom of the film ($z = 8$ nm) average pore size of 32.0

± 4.1 nm was measured. Below z = 7 nm the signal to noise ratio was too low for a reliable measurement. The measured pore size at the surface from the tomography data was higher than what was measured from the SEM images; we attribute this difference to the different interaction of the specimen with the electron beam and the detecting systems in the two imaging systems.

The change in pore size through depth indicates that for the SIS conditions used in this study, higher Al_2O_3 growth occurred at the top third of the film compared to the bottom of the film. Since SIS is a diffusion-limited process, more uniform Al_2O_3 growth could be expected if longer exposure time is used.[52,53] Additionally, purge time could affect the SIS growth due to the unstable nature of physisorbed PMMA-TMA complex.[53] Optimizing purge time could minimize the amount of precursor that is physically absorbed at the top of the film and allow covalent bonding to form between the metal precursor and the polymer moieties inside the film.[53] However, for separation applications, the widening of pores with depth is desired, since the narrow pore size enables high selectively and the widening of the pores leads to high flux.[15,17]

2.4.4 Similarly Sized Protein Separation

Using a U-shape diffusion cell (Figure 2-10), separation tests were conducted on alumina membranes using two similar-size proteins in buffer solutions (see experimental section). Bovine serum albumin (BSA) and bovine hemoglobin (BHb) were chosen as a model system since they have similar volumes (14 nm × 3.8 nm × 3.8 nm and 6.4 nm × 5.5 nm × 5 nm, respectively) but different isoelectric points (4.7 and 7.0, respectively);[54,55] thus, their electrical charge can be tuned by varying the pH value of the buffer solution (Figure 2-11). The ionic strength of the buffer solution was chosen to be 0.01M since it results in Debye length of ~ 3.3 nm in the electric double layer (EDL) which is developed around the charged proteins and the charged pore walls (see experimental section). This Debye length is significant for pore sizes of ~ 20 nm and proteins

diameters of ~ 6 nm.[21,36,56] The flux and the separation selectivity were compared between three membranes: a) the hierarchical AlO_x/AAO membrane developed in this study (AlO_x membrane templated by the 141 nm thick BCP film treated with 3 cycles of Al_2O_3 SIS and transferred onto a commercially available AAO membrane with 100 nm pores), b) commercially available AAO membrane with 100 nm pores, and c) commercially available AAO membrane with 20 nm pores.

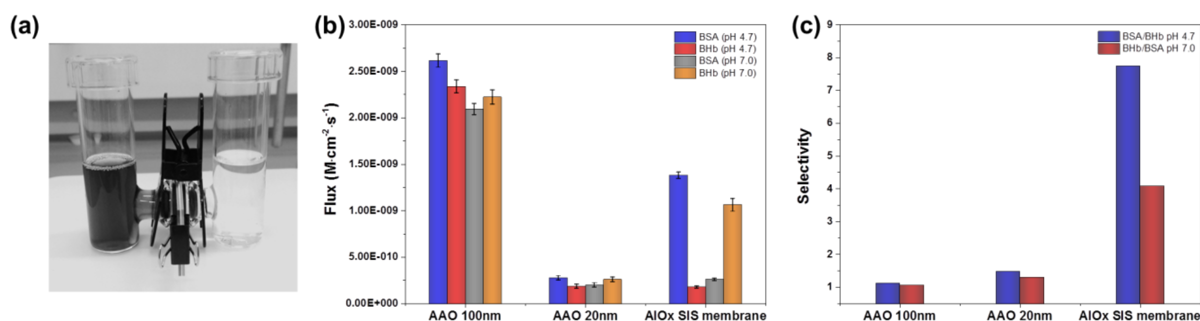

Figure 2-10: The separation of similarly size proteins: (a) the membranes performance was tested using a U-shape cell. (b) The flux of BSA and BHb measured at pH values of 4.7 and 7.0 through three different membranes: AAO membrane with average pore diameter of 100 nm, AAO membrane with average pore diameter of 20 nm, and a hierarchical membrane with BCP-templated AlO_x membrane on top of AAO membrane with average pore diameter of 100 nm (AlO_x SIS membrane). (c) Separation selectivity of BSA/BHb at pH 4.7 and BHb/BSA at pH 7 for the three membrane types.

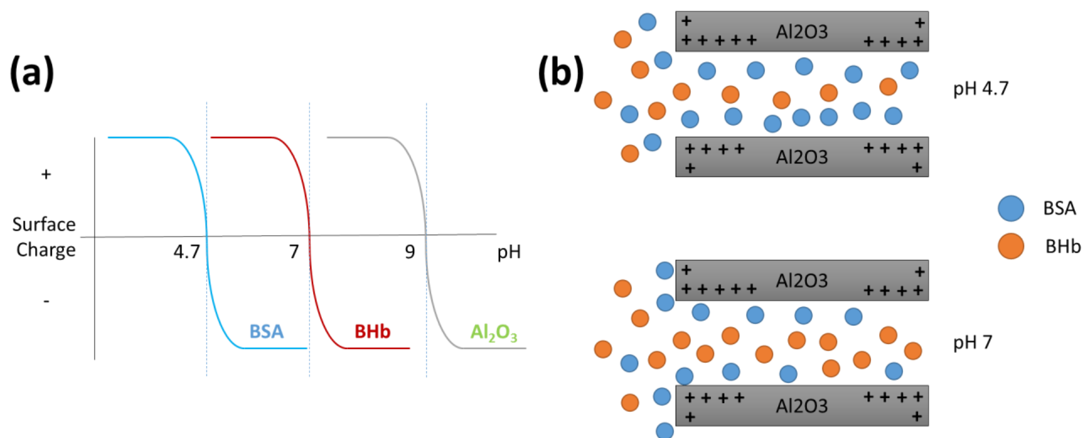

Figure 2-11: (a) Surface charge *versus* pH for BSA, BHb and Al_2O_3 membranes. (c) Schematic illustrations showing the transport of BSA (blue) and BHb (red) through the membrane at pH 4.7 and 7.0.

The average flux of the proteins at pH = 4.7 and pH = 7.0 in a mixed protein diffusion experiment using these three membranes is presented in Figure 2-10(b). The flux values were normalized according to the open area fraction of each membrane, considering that 37% of AlO_x pores are blocked by the AAO membrane underneath. At pH = 4.7, BSA diffused through AAO membrane with average pore size of 100 nm at high flux of $(2.6 \pm 0.1) \times 10^{-9}$ $M \cdot cm^{-2} \cdot s^{-1}$, and the flux of BHb was only slightly lower ($(2.3 \pm 0.1) \times 10^{-9}$ $M \cdot cm^{-2} \cdot s^{-1}$). These flux values are in good agreement with other protein separation results using membranes with the same characteristic pore size.[54,56] The selectivity of separation, calculated from the flux ratio between two proteins, was 1.1 ± 0.1 (Figure 2-10(c)). Although at pH = 4.7 BSA has neutral charge while BHb and the AlO_x membrane are positively charged (Al_2O_3 isoelectric point is 9), the difference in the charge states has little effect on the separation selectivity since the effective pore size (with the EDL) is considerably larger than the hydrated protein diameters. The same behavior was seen at pH = 7.0, where both proteins showed high flux (BSA flux: $(2.1 \pm 0.1) \times 10^{-9}$ $M \cdot cm^{-2} \cdot s^{-1}$, and BHb flux: $(2.2 \pm 0.1) \times 10^{-9}$ $M \cdot cm^{-2} \cdot s^{-1}$), leading to low selectivity of 1.1 ± 0.1.

When AAO membrane with average pore size of 20 nm was used for separating the two proteins, small increase in selectivity was measured (1.5 ± 0.2 and 1.3 ± 0.2 for the pH values of 4.7 and 7, respectively), but with low flux values of $(1.8 \pm 0.2) \times 10^{-10}$ to $(2.8 \pm 0.2) \times 10^{-10}$ $M \cdot cm^{-2} \cdot s^{-1}$. At pore diameter of 20 nm, the effective pore size is close to the hydrated protein diameter and the proteins must diffuse through 60 µm thick membrane, resulting in lower flux compared to the 100 nm pore AAO membrane. The relatively small increase in selectivity was attributed to the large thickness of the membrane and the wide distribution of pore sizes.[55]

When the hierarchical membrane with 62 nm thick top layer of porous AlO_x templated by BCP (SIS membrane) was used to separate the proteins, both high flux and high selectivity were

observed. At pH = 4.7, BSA flux was $(1.4 \pm 0.1) \times 10^{-9}$ M·cm^{-2}·s^{-1} and BHb flux was $(1.8 \pm 0.1) \times 10^{-10}$ M·cm^{-2}·s^{-1}, resulting in selectivity of 7.7 ± 0.1, while at pH = 7.0, BSA flux and BHb flux were $(2.6 \pm 0.1) \times 10^{-10}$ M·cm^{-2}·s^{-1}, and $(1.1 \pm 0.1) \times 10^{-9}$ M·cm^{-2}·s^{-1}, respectively, resulting in selectivity of 4.1 ± 0.1. The high flux through the AlO_x membrane and the 3-5 folds' increase in selectivity compared to the 20 nm pores size AAO membrane are attributed to the ultrathin selective layer (62 nm, Figure 2-9) and the narrow pore size distribution (19.1 ± 0.9 nm, Figure 2-8, that enable to effectively harness the charged protein-membrane interactions. At pH = 4.7, the positively charged BHb can barely diffuse through the positively charged membrane, while BSA, which does not carry electrical charges, can efficiently diffuse through the 60 nm thick AlO_x membrane. At pH = 7.0, BSA is negatively charged while BHb is neutral, leading to efficient diffusion of BHb through the hierarchical membrane.

The combination of hierarchical alumina membrane with thin separating layer and uniform nanoscale pores resulted in improved performance over commercial AAO membranes. Future development of this BCP-templated inorganic membrane for water UF should include a comparison between this type of membrane and commercially available polymeric UF membranes. With the progress recently demonstrated in roll-to-roll processes for both BCP[11] and ALD[57] and further engineering of the support layer to create low-roughness, low-cost, robust substrate, BCP-templated inorganic membrane could be fabricated on a large scale.

2.5 Summary

In summary, we have demonstrated that PMMA-rich, cylinder-forming PS-*b*-PMMA can be harnessed to template nanoporous AlO_x membranes with narrow pore size distribution and precise control over the pore size and showed the protein separation capabilities of this membrane. Perpendicular-oriented PS cylinders were assembled in PMMA-rich BCP films over a large range

of thicknesses by precisely controlling the substrate chemistry and the annealing temperature. Nanoporous AlO_x membranes with tunable pore size were templated by single BCP through variating the amount of Al_2O_3 grown inside the PMMA domains in the SIS process. GISAXS and electron microscopy showed the highly order hexagonally packed structures of the BCP film, the hybrid intermediate, and the AlO_x nanoporous membrane, with STEM tomography revealing the high connectivity and non-tortuous pore structure in three dimensions. The diffusion-limited infiltration and growth of Al_2O_3 precursors in the PMMA block resulted in a gradient in Al_2O_3 content through depth, with larger Al_2O_3 content at the top versus the bottom and hence an increase in pore size from top to bottom of the membrane, as evident from the STEM tomography. This non-homogeneous depth profile is considered ideal for separation applications.

Combining the thin BCP-templated AlO_x membrane with supporting AAO membrane resulted in hierarchical membrane that was used for separating similarly sized proteins. The ultrathin AlO_x nanostructure and the narrowly distributed pore size enabled the hierarchical membrane to separate proteins with both high flux and high selectivity. The processes and membrane fabrication approach developed in this research provides a potential new route for making isoporous metal-oxide membranes. We envision this route as a new platform for advanced and multifunctional membranes that would exhibit high separation selectivity, anti-fouling behavior and photocatalytic activity.

2.6 References

(1) Dekker, C. Solid-State Nanopores. *Nat. Nanotechnol.* **2007**, *2* (4), 209–215.

(2) Jackson, E. A.; Hillmyer, M. A. Nanoporous Membranes Derived from Block Copolymers: From Drug Delivery to Water Filtration. *ACS Nano* **2010**, *4* (7), 3548–3553.

(3) Fu, J.; Mao, P.; Han, J. Artificial Molecular Sieves and Filters: A New Paradigm for

Biomolecule Separation. *Trends Biotechnol.* **2008**, *26* (6), 311–320.

(4) Adiga, S. P.; Jin, C.; Curtiss, L. A.; Monteiro-Riviere, N. A.; Narayan, R. J. Nanoporous Membranes for Medical and Biological Applications. *Wiley Interdiscip. Rev. Nanomedicine Nanobiotechnology* **2009**, *1* (5), 568–581.

(5) Majd, S.; Yusko, E. C.; Billeh, Y. N.; Macrae, M. X.; Yang, J.; Mayer, M. Applications of Biological Pores in Nanomedicine, Sensing, and Nanoelectronics. *Curr. Opin. Biotechnol.* **2010**, *21* (4), 439–476.

(6) Adiga, S. P.; Curtiss, L. A.; Elam, J. W.; Pellin, M. J.; Shih, C.-C.; Shih, C.-M.; Lin, S.-J.; Su, Y.-Y.; Gittard, S. D.; Zhang, J.; et al. Nanoporous Materials for Biomedical Devices. *JOM* **2008**, *60* (3), 26–32.

(7) Kim, M. J.; Wanunu, M.; Bell, D. C.; Meller, A. Rapid Fabrication of Uniformly Sized Nanopores and Nanopore Arrays for Parallel DNA Analysis. *Adv. Mater.* **2006**, *18* (23), 3149–3153.

(8) Nam, S.-W.; Rooks, M. J.; Kim, K.-B.; Rossnagel, S. M. Ionic Field Effect Transistors with Sub-10 Nm Multiple Nanopores. *Nano Lett.* **2009**, *9* (5), 2044–2048.

(9) Striemer, C. C.; Gaborski, T. R.; McGrath, J. L.; Fauchet, P. M. Charge- and Size-Based Separation of Macromolecules Using Ultrathin Silicon Membranes. *Nature* **2007**, *445* (7129), 749–753.

(10) Lee, A.; Elam, J. W.; Darling, S. B. Membrane Materials for Water Purification: Design, Development, and Application. *Environ. Sci. Water Res. Technol.* **2016**, *2* (1), 17–42.

(11) Singh, G.; Batra, S.; Zhang, R.; Yuan, H.; Yager, K. G.; Cakmak, M.; Berry, B.; Karim, A. Large-Scale Roll-to-Roll Fabrication of Vertically Oriented Block Copolymer Thin Films. *ACS Nano* **2013**, *7* (6), 5291–5299.

(12) Rangou, S.; Buhr, K.; Filiz, V.; Clodt, J. I.; Lademann, B.; Hahn, J.; Jung, A.; Abetz, V. Self-Organized Isoporous Membranes with Tailored Pore Sizes. *J. Memb. Sci.* **2014**, *451*, 266–275.

(13) Bates, F. S.; Fredrickson, G. H. Block Copolymer Thermodynamics: Theory and Experiment. *Annu. Rev. Phys. Chem.* **1990**, *41* (1), 525–557.

(14) Yang, S. Y.; Park, J.; Yoon, J.; Ree, M.; Jang, S. K.; Kim, J. K. Virus Filtration Membranes Prepared from Nanoporous Block Copolymers with Good Dimensional Stability under High Pressures and Excellent Solvent Resistance. *Adv. Funct. Mater.* **2008**, *18* (9), 1371–1377.

(15) Yang, S. Y.; Ryu, I.; Kim, H. Y.; Kim, J. K.; Jang, S. K.; Russell, T. P. Nanoporous Membranes with Ultrahigh Selectivity and Flux for the Filtration of Viruses. *Adv. Mater.* **2006**, *18* (6), 709–712.

(16) Phillip, W. A.; O'neill, B.; Rodwogin, M.; Hillmyer, M. A.; Cussler, E. L. Self-Assembled Block Copolymer Thin Films as Water Filtration Membranes. *ACS Appl. Mater. Interfaces* **2010**, *2* (3), 847–853.

(17) Peinemann, K.-V.; Abetz, V.; Simon, P. F. W. Asymmetric Superstructure Formed in a Block Copolymer via Phase Separation. *Nat. Mater.* **2007**, *6* (12), 992–996.

(18) Dorin, R. M.; Sai, H.; Wiesner, U. Hierarchically Porous Materials from Block Copolymers. *Chem. Mater.* **2014**, *26* (1), 339–347.

(19) Yang, S. Y.; Yang, J.-A.; Kim, E.-S.; Jeon, G.; Oh, E. J.; Choi, K. Y.; Hahn, S. K.; Kim, J. K. Single-File Diffusion of Protein Drugs through Cylindrical Nanochannels. *ACS Nano* **2010**, *4* (7), 3817–3822.

(20) Hillmyer, M. A. Nanoporous Materials from Block Copolymer Precursors. In *Block Copolymers II*; Springer-Verlag: Berlin/Heidelberg, **2005**; *190*, 137–181.

(21) Qiu, X.; Yu, H.; Karunakaran, M.; Pradeep, N.; Nunes, S. P.; Peinemann, K.-V. Selective Separation of Similarly Sized Proteins with Tunable Nanoporous Block Copolymer Membranes. *ACS Nano* **2013**, *7* (1), 768–776.

(22) Nandan, B.; Kuila, B. K.; Stamm, M. Supramolecular Assemblies of Block Copolymers as Templates for Fabrication of Nanomaterials. *Eur. Polym. J.* **2011**, *47* (4), 584–599.

(23) Nam, C.-Y.; Stein, A.; Kisslinger, K.; Black, C. T. Electrical and Structural Properties of ZnO Synthesized via Infiltration of Lithographically Defined Polymer Templates. *Appl. Phys. Lett.* **2015**, *107* (20), 203106.

(24) Nam, C.-Y.; Stein, A.; Kisslinger, K. Direct Fabrication of High Aspect-Ratio Metal Oxide Nanopatterns via Sequential Infiltration Synthesis in Lithographically Defined SU-8 Templates. *J. Vac. Sci. Technol. B, Nanotechnol. Microelectron. Mater. Process. Meas. Phenom.* **2015**, *33* (6), 06F201.

(25) Peng, Q.; Tseng, Y.-C.; Darling, S. B.; Elam, J. W. Nanoscopic Patterned Materials with Tunable Dimensions via Atomic Layer Deposition on Block Copolymers. *Adv. Mater.* **2010**, *22* (45), 5129–5133.

(26) Peng, Q.; Tseng, Y.-C.; Darling, S. B.; Elam, J. W. A Route to Nanoscopic Materials via Sequential Infiltration Synthesis on Block Copolymer Templates. *ACS Nano* **2011**, *5* (6), 4600–4606.

(27) Cummins, C.; Ghoshal, T.; Holmes, J. D.; Morris, M. A. Strategies for Inorganic Incorporation Using Neat Block Copolymer Thin Films for Etch Mask Function and Nanotechnological Application. *Adv. Mater.* **2016**, *28* (27), 5586–5618.

(28) Kamcev, J.; Germack, D. S.; Nykypanchuk, D.; Grubbs, R. B.; Nam, C.-Y.; Black, C. T. Chemically Enhancing Block Copolymers for Block-Selective Synthesis of Self-Assembled

Metal Oxide Nanostructures. *ACS Nano* **2013**, *7* (1), 339–346.

(29) Tseng, Y.-C.; Mane, A. U.; Elam, J. W.; Darling, S. B. Enhanced Lithographic Imaging Layer Meets Semiconductor Manufacturing Specification a Decade Early. *Adv. Mater.* **2012**, *24* (19), 2608–2613.

(30) Tseng, Y.-C.; Peng, Q.; Ocola, L. E.; Elam, J. W.; Darling, S. B. Enhanced Block Copolymer Lithography Using Sequential Infiltration Synthesis. *J. Phys. Chem. C* **2011**, *115* (36), 17725–17729.

(31) Tseng, Y.-C.; Peng, Q.; Ocola, L. E.; Czaplewski, D. A.; Elam, J. W.; Darling, S. B. Enhanced Polymeric Lithography Resists via Sequential Infiltration Synthesis. *J. Mater. Chem.* **2011**, *21* (32), 11722.

(32) Ruiz, R.; Wan, L.; Lille, J.; Patel, K. C.; Dobisz, E.; Johnston, D. E.; Kisslinger, K.; Black, C. T. Image Quality and Pattern Transfer in Directed Self Assembly with Block-Selective Atomic Layer Deposition. *J. Vac. Sci. Technol. B, Nanotechnol. Microelectron. Mater. Process. Meas. Phenom.* **2012**, *30* (6), 06F202.

(33) Segal-Peretz, T.; Winterstein, J.; Doxastakis, M.; Ramírez-Hernández, A.; Biswas, M.; Ren, J.; Suh, H. S.; Darling, S. B.; Liddle, J. A.; Elam, J. W.; et al. Characterizing the Three-Dimensional Structure of Block Copolymers via Sequential Infiltration Synthesis and Scanning Transmission Electron Tomography. *ACS Nano* **2015**, *9* (5), 5333–5347.

(34) Segal-Peretz, T.; Winterstein, J.; Biswas, M.; Liddle, J. A.; Elam, J. W.; Zaluzec, N. J.; Nealey, P. F. Staining Block Copolymers Using Sequential Infiltration Synthesis for High Contrast Imaging and STEM Tomography. *Microsc. Microanal.* **2015**, *21* (S3), 611–612.

(35) Ren, J.; Ocola, L. E.; Divan, R.; Czaplewski, D. A.; Segal-Peretz, T.; Xiong, S.; Kline, R. J.; Arges, C. G.; Nealey, P. F. Post-Directed-Self-Assembly Membrane Fabrication for in

Situ Analysis of Block Copolymer Structures. *Nanotechnology* **2016**, *27* (43), 435303.

(36) Squires, T. M.; Quake, S. R. Microfluidics: Fluid Physics at the Nanoliter Scale. *Rev. Mod. Phys.* **2005**, *77* (3), 977–1026.

(37) Ham, S.; Shin, C.; Kim, E.; Ryu, D. Y.; Jeong, U.; Russell, T. P.; Hawker, C. J. Microdomain Orientation of PS- b -PMMA by Controlled Interfacial Interactions. *Macromolecules* **2008**, *41* (17), 6431–6437.

(38) Gu, W.; Hong, S. W.; Russell, T. P. Orienting Block Copolymer Microdomains with Block Copolymer Brushes. *ACS Nano* **2012**, *6* (11), 10250–10257.

(39) Han, E.; Stuen, K. O.; Leolukman, M.; Liu, C.-C.; Nealey, P. F.; Gopalan, P. Perpendicular Orientation of Domains in Cylinder-Forming Block Copolymer Thick Films by Controlled Interfacial Interactions. *Macromolecules* **2009**, *42* (13), 4896–4901.

(40) Black, C. T.; Guarini, K. W. Structural Evolution of Cylindrical-Phase Diblock Copolymer Thin Films. *J. Polym. Sci. Part A Polym. Chem.* **2004**, *42* (8), 1970–1975.

(41) Ji, S.; Liu, C.-C.; Liao, W.; Fenske, A. L.; Craig, G. S. W.; Nealey, P. F. Domain Orientation and Grain Coarsening in Cylinder-Forming Poly(Styrene- b -Methyl Methacrylate) Films. *Macromolecules* **2011**, *44* (11), 4291–4300.

(42) Han, E.; Stuen, K. O.; La, Y.-H.; Nealey, P. F.; Gopalan, P. Effect of Composition of Substrate-Modifying Random Copolymers on the Orientation of Symmetric and Asymmetric Diblock Copolymer Domains. *Macromolecules* **2008**, *41* (23), 9090–9097.

(43) Liu, C.-C.; Han, E.; Onses, M. S.; Thode, C. J.; Ji, S.; Gopalan, P.; Nealey, P. F. Fabrication of Lithographically Defined Chemically Patterned Polymer Brushes and Mats. *Macromolecules* **2011**, *44* (7), 1876–1885.

(44) Delgadillo, P. A. R. Implementation of a Chemo-Epitaxy Flow for Directed Self-Assembly

on 300-Mm Wafer Processing Equipment. *J. Micro/Nanolithography, MEMS, MOEMS* **2012**, *11* (3), 031302.

(45) Welander, A. M.; Craig, G. S. W.; Tada, Y.; Yoshida, H.; Nealey, P. F. Directed Assembly of Block Copolymers in Thin to Thick Films. *Macromolecules* **2013**, *46* (10), 3915–3921.

(46) Suh, H. S.; Kang, H.; Nealey, P. F.; Char, K. Thickness Dependence of Neutral Parameter Windows for Perpendicularly Oriented Block Copolymer Thin Films. *Macromolecules* **2010**, *43* (10), 4744–4751.

(47) Durand, W. J.; Carlson, M. C.; Maher, M. J.; Blachut, G.; Santos, L. J.; Tein, S.; Ganesan, V.; Ellison, C. J.; Willson, C. G. Experimental and Modeling Study of Domain Orientation in Confined Block Copolymer Thin Films. *Macromolecules* **2016**, *49* (1), 308–316.

(48) Busch, P.; Rauscher, M.; Moulin, J.-F.; Müller-Buschbaum, P. Debye–Scherrer Rings from Block Copolymer Films with Powder-like Order. *J. Appl. Crystallogr.* **2011**, *44* (2), 370–379.

(49) Vu, T.; Mahadevapuram, N.; Perera, G. M.; Stein, G. E. Controlling Domain Orientations in Thin Films of AB and ABA Block Copolymers. *Macromolecules* **2011**, *44* (15), 6121–6127.

(50) Singh, A.; Knaepen, W.; Sayan, S.; el Otell, Z.; Chan, B. T.; Maes, J. W.; Gronheid, R. Impact of Sequential Infiltration Synthesis on Pattern Fidelity of DSA Lines. In *Proc. SPIE*; Wallow, T. I., Hohle, C. K., Eds.; 2015; Vol. 9425, p 94250N.

(51) Nam, C.-Y.; Stein, A.; Kisslinger, K.; Black, C. T. Electrical and Structural Properties of ZnO Synthesized via Infiltration of Lithographically Defined Polymer Templates. *Appl. Phys. Lett.* **2015**, *107* (20), 203106.

(52) Biswas, M.; Libera, J. A.; Darling, S. B.; Elam, J. W. Kinetics for the Sequential Infiltration

Synthesis of Alumina in Poly(Methyl Methacrylate): An Infrared Spectroscopic Study. *J. Phys. Chem. C* **2015**, *119* (26), 14585–14592.

(53) Biswas, M.; Libera, J. A.; Darling, S. B.; Elam, J. W. New Insight into the Mechanism of Sequential Infiltration Synthesis from Infrared Spectroscopy. *Chem. Mater.* **2014**, *26* (21), 6135–6141.

(54) Ileri, N.; Faller, R.; Palazoglu, A.; Létant, S. E.; Tringe, J. W.; Stroeve, P. Molecular Transport of Proteins through Nanoporous Membranes Fabricated by Interferometric Lithography. *Phys. Chem. Chem. Phys.* **2013**, *15* (3), 965–971.

(55) Osmanbeyoglu, H. U.; Hur, T. B.; Kim, H. K. Thin Alumina Nanoporous Membranes for Similar Size Biomolecule Separation. *J. Memb. Sci.* **2009**, *343* (1–2), 1–6.

(56) Stroeve, P.; Rahman, M.; Naidu, L. D.; Chu, G.; Mahmoudi, M.; Ramirez, P.; Mafe, S. Protein Diffusion through Charged Nanopores with Different Radii at Low Ionic Strength. *Phys. Chem. Chem. Phys.* **2014**, *16* (39), 21570–21576.

(57) Dickey, E.; Barrow, W. A. High Rate Roll to Roll Atomic Layer Deposition, and Its Application to Moisture Barriers on Polymer Films. *J. Vac. Sci. Technol. A Vacuum, Surfaces, Film.* **2012**, *30* (2), 021502.

CHAPTER 3: STUDYING THE EFFECTS OF CHEMISTRY AND GEOMETRY ON DSA HOLE-SHRINK PROCESS IN THREE DIMENSIONS

3.1 Abstract

Acquiring three-dimensional information becomes increasingly important for the development of block copolymer (BCP) directed self-assembly (DSA) lithography, as 2D imaging is no longer sufficient to describe the 3D nature of DSA morphology and probe hidden structures under the surface. In this study, using post-DSA membrane fabrication technique and STEM (scanning transmission electron microscopy) tomography we were able to characterize the 3D structures of BCP in graphoepitaxial DSA hole shrink process. Different DSA structures of singlets formed in templated holes with different surface chemistry and geometry were successfully captured and their 3D shapes were reconstructed from tomography data. The results reveal that strong polystyrene-preferential sidewalls are necessary to create vertical DSA cylinders and that template size outside of process window could result in defective DSA results in three dimensions. Our study as well as the established 3D metrology would greatly help to develop a fundamental understanding of the key DSA factors for optimizing the graphoepitaxial hole shrink process.

3.2 Introduction

Directed self-assembly (DSA) of block copolymers (BCP) has been widely investigated as a potential patterning solution to extend lithography to generate smaller and denser features[1,2]. Graphoepitaxial DSA of cylinder-forming BCP is a promising implementation of DSA to fabricate uniform holes well below the conventional lithography resolution.[3] In a typical DSA hole shrink process, the guide holes matching the BCP size are firstly made using conventional lithographic method. Then, a cylinder forming polystyrene-block-poly(methyl methacrylate) (PS-*b*-PMMA) is spin-coated and phase separated in the confined space. During annealing, vertical PMMA

cylindrical domains are formed in the center of the hole guide patterns. After selectively removing PMMA block, the shrinkage of hole pattern dimensions depending on the molecular weight of PS-*b*-PMMA is achieved.[3,4]

Currently, most studies are evaluating the DSA hole shrink process based on observations from 2D top view images obtained from scanning electron microscopes (SEM), like statistical studies of process window[5]. The insight of three-dimensional BCP morphologies inside the holes is limited. Judging from top view images solely could result in the misinterpretations when analyzing the defectively of DSA hole shrink process because the defects might be hidden under the surface.[6] Although some simulation studies have predicted that the three-dimensional DSA structure is affected by factors including the size of guide holes, the compositions of BCP and the affinity of surface[7–10], it is often difficult to evaluate the accuracy of these simulation results due to the lack of direct comparison from experimental results.[6] Therefore, it is very valuable to obtain precise 3D information of BCP assembled inside the holes.

Here, we developed a 3D metrology for graphepitaxial hole shrink process using post-DSA membrane fabrication techniques and STEM tomography[11,12]. The self-assembly of PS-*b*-PMMA cylinders were directed by guide holes made of spin-on carbon (SOC) on silicon nitride coated Si substrate, which was then made into membrane sample for TEM characterization. Two different brushes were used to modify the affinity of the sidewall and bottom surface separately. The effect of surface modification on confined cylinder morphology was studied using STEM tomography. By comparing the reconstruction results with simulated morphologies, we were able to predict how different surface conditions would result in the defective DSA structure. A similar 3D metrology was applied to the 300 mm track-processed wafer. 3D structures of singlets with

different template size were reconstructed from tomography series. Different defective morphologies when templates were too small or too large were analyzed.

3.3 Experimental Section

In this section we describe the DSA hole shrink sample fabrication followed by the TEM sample preparation as shown in Figure 3-1.

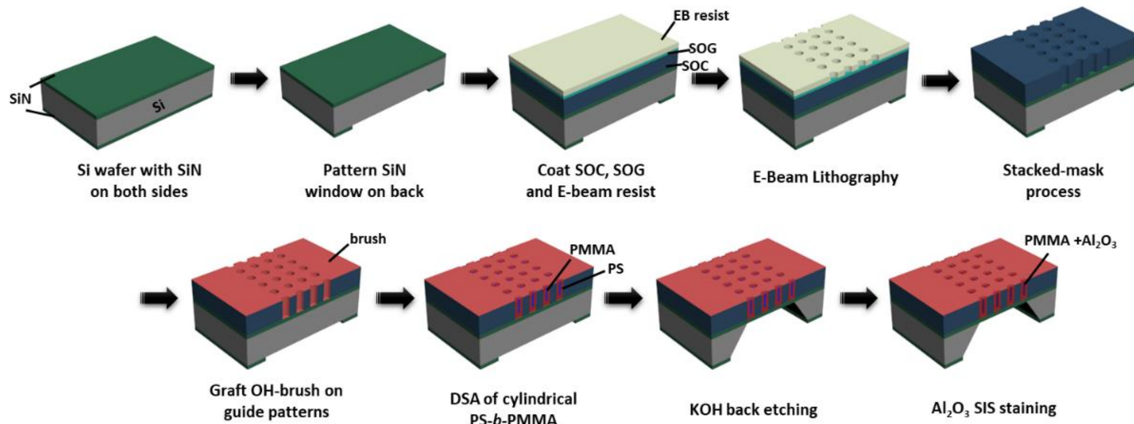

Figure 3-1: Schematic illustration of DSA hole-shrink process and TEM sample preparation

3.3.1 Materials

Spin-on-carbon (SOC) and spin-on-glass (SOG) solutions were provided by Tokyo Ohka Kogyo Co. (TOK) and used as received. GL-2000-12 E-beam resist was purchased from Gluon. Two polystyrene-based brushes A and B with different end groups were synthesized by TOK and used as received. Cylinder-forming PS-b-PMMA (L_0, center-to-center periodicity = 38 nm) as well as a lamella-forming PS-b-PMMA (L_0 = 32 nm) were synthesized by TOK and used as received. 200 μm thick Silicon wafers (N-type doped, ⟨100⟩ orientation, double-side polished) coated with 30 nm thick low-stress silicon nitride (SiN_x) on both sides were purchased from Pure Wafer.

3.3.2 Graphoepitaxy process flow

The templated DSA approach in this study is similar to the one developed by imec.[13] The substrate was spin coated with ~100 nm of SOC and ~30 nm of SOG and ~60 nm of e-beam resist. E-beam lithography was performed to write hole patterns with ~55 nm in diameter and 110 nm pitch. The hole patterns were transferred from resist layer into the SOG and then from SOG to SOC through dry etch using CF_4 and O_2 gas respectively. The SOG was removed by buffered oxide etchant. Brush A or B was grafted on the templates by spin-coating from solution, annealing at 280 °C for 1 min and organic solvent rinsing. The cylinder-forming PS-*b*-PMMA was spin coated on the templates to a film thickness of approximately 20 nm (as measured from a similarly cast film on bare silicon) and annealed at 250 °C for 1 min under a N_2 environment. The DSA samples made from 300 mm track-processed wafer was prepared in imec using photolithography and different brushes and BCP as described in literature.[14]

3.3.3 Characterization of surface properties

Wafers coated with flat SOC and SiN_x films and gone through the same O_2 etch process are used to mimic the bottom and sidewall surface. Brush A and B were applied to different substrates separately. The lamella-forming PS-b-PMMA (L_0 = 32 nm) was spin-coated to form 40 nm thick films on brush grafted substrates. The samples were thermally annealed at 180°C for 15 min. Optical characterization was performed with an Olympus BX60 microscope. The scanning electron microscopy was performed with a Carl Zeiss Merlin SEM.

3.3.4 TEM sample preparation

The aforementioned DSA hole shrink samples were prepared on the front side of SiN_x coated wafer, and were made into TEM membrane sample using the post-DSA membrane fabrication method~~s as~~ reported in an earlier paper.[11] SiN_x on the back side of wafer was patterned by optical

lithography as the first step (Figure 3-1). After performing hole shrink DSA on the front side, wafers were back etched in KOH solution with front side sealed and protected to make several 3 mm × 3 mm TEM samples with target pattern area at the center of 1 mm × 200 μm large SiN_x windows for TEM imaging. The 300 mm track-processed was made into TEM samples using the same approach, except the Si wafer thickness is 800 μm and the SiN_x film thickness is 15 nm.

3.3.5 STEM tomography and 3D reconstruction

We use the similar sample staining and STEM tomography methods as described in an earlier paper.[12,15] Al_2O_3 sequential infiltration synthesis (SIS) was performed on each TEM samples using alternating exposures to trimethylaluminum (TMA) and deionized H_2O to selectively stain PMMA and provide imaging contrast and stability. STEM tomography was performed using a field-emission gun TEM (FEI Tecnai) operated at 200 kV. The camera length is 300 mm and samples were imaged using high angle annular dark field detector. STEM Images were collected from hole shrink samples with holder tilting from -70° to +70° with 2° or 3° angular interval and dynamic focus. The range of tilting angles of 800 μm thick samples was narrowed down to about -54° to +54°. The tilt series were then aligned and reconstructed into *xy* slices stacking along *z* direction using Inspect3D software.

Segmentation (thresholding) of the reconstructed image stacks was performed in ImageJ. Binary signals corresponding to stained PMMA domains and SOC templates were separated into two stacks. The stack of PS domains was generated by filling the binary signals of the SOC templates (from hollow circles to solid circles). The rendered 3D structures were visualized in tomviz software when displaying the contours of PMMA stack colored in blue and PS stack colored in red simultaneously**.**

3.3.6 Simulation

The simulation results presented in this work are based on the standard theoretically informed coarse-grained model.[16–18] This model has previously been shown to be in quantitative with experimental results.[19,20] The cylindrical confinement is imposed by hard walls; the sidewall and bottom substrate interact with the polymer according to a term parametrized by a proportionality constant A, the magnitude of which dictates the strength of substrate interactions. Full details are available in the a previous publication[21].

3.4 Results and Discussion

3.4.1 3D metrology for DSA hole shrink process

The direct observation of three-dimensional morphologies of PS-*b*-PMMA cylinders within templated holes is rarely reported mainly due to the challenges of sample preparation. Several studies used cross-sectional TEM to measure the amount of residual PS layer between PMMA cylinder and the bottom of templates.[6,8] However, as a destructive method, shrinkage and mismatch of thickness is often found as the issue. Okabe K *et al.* used FIB Pt deposition and milling to prepare cross-sectional TEM samples. Using elemental mapping and 3D reconstruction, they successfully captured a noticeable amount of PS residual layer under the Pt filling.[6] Although FIB is versatile to make site-specific TEM samples, it requires the removal of material and protecting polymers from FIB damage could be difficult. A reduction in SOG and SOC thickness as large as 40 nm was observed implying the potential compression of BCP structure as well.[6] Therefore, it is important to develop a 3D metrology with minimal damage to the polymer assemblies as well as SOC templates during the sample preparation. Dixit D *et al*. reported that they used a ellipsometry-based scatterometry to optically characterize DSA hole shrink samples, which can non-destructively predict dimensional changes.[22] However, this method is limited to

characterize local and detailed DSA-induced defects. Without comparing to 3D real space information, it is difficult to evaluate the accuracy of optical models they applied.

Recently, STEM tomography has been developed to probe different BCP 3D structures and it is especially suitable for capturing heterogeneous and complicated morphologies.[12,15,23] In this study, we use an established TEM sample preparation approach based on the back-etching of SiN_x coated <100> Si wafers[11]. The template made of SOC as well as block polymer films on the front side of wafer are perfectly preserved. Using SIS staining, the shape of polymer interface could be clearly revealed, which avoids any potential damage caused by selective removal of polymer domains and metal deposition. Although the field of view in STEM tomography is limited (1 µm ×1 µm in this study) to get high resolution images, the 3D volume of about thirty holes could be captured in each tomography series. Therefore, it offers a much larger field of view than regular cross-sectional images and gives more representative and statistical data. With all these advantages, the 3D metrology used in this study could be a high throughput method to acquire the detailed information of DSA hole shrink process in all dimensions.

3.4.2 Effects of surface chemistry

Previous simulation studies have predicted that both the surface chemistry and geometry of cylindrical templates play important role in guiding the DSA of BCP cylinders.[8,9] In terms of surface chemistry, defect-free DSA is predicted when sidewall is wetting to PS and bottom is non-preferential to PS and PMMA.[8,9] The challenge to reach this ideal situation is that, during SOC etch step both sidewall and bottom surface are exposed to oxygen-containing plasma and that both could be easily modified by OH terminated polymer brush. There are differences in materials though: the sidewall surface is plasma exposed SOC and the bottom surface is plasma exposed SiN_x (or other substrates). Doise J *et al.* developed a dual-brush process and could independently

modify the sidewall and bottom surface by consecutively grafting two brushes with distinct end-groups.[14] In our study of surface chemistry effects, only one brush was used in each DSA sample, but the surface chemistry was controlled by kinetically grafting of the polymer brush. Two polystyrene based brush A and B with different end groups were found that when grafted at high temperature they could modify the sidewall and bottom surface differently.

We follow Doise J *et al.*'s approach[14] to prepare SOC and SiN_x substrates mimicking sidewall and bottom surface and determine the surface affinity. The schematic of the hole and island test is shown in Figure 3-2 (a). Films of a lamella-forming PS-*b*-PMMA are prepared on SOC and SiN_x modified by brush A or B. The film thickness is carefully controlled to about 40 nm (1.25 L_0). Based on previously reported studies[14,24], perpendicular oriented BCP microdomains are formed and the film is flat macroscopically when the substrate is non-preferential to PS and PMMA. In contrast, preferential wetting of PS or PMMA at substrates leads to parallel oriented lamella. With PS domain on the top surface when thermally annealed at 180 °C, islands like terraced topography is observed optically for PS-preferential substrates and holes like terraced topography is formed for PMMA preferential substrates. The characterization results of SOC and SiN_x modified by brush A and B are shown in Figure 3-2 (b). Both substrates show holes like terraces in optical micrographs as they wet PMMA after O_2 etch. Islands are observed on the SOC sidewall surfaces modified by both brush A and B, and the SiN_x bottom surface modified by brush A only, indicating the PS-wetting behavior on these three surfaces. The SiN_x bottom surface modified by brush B shows flat surface optically and perpendicular lamella morphology in SEM, corresponding to the non-preferential wetting.

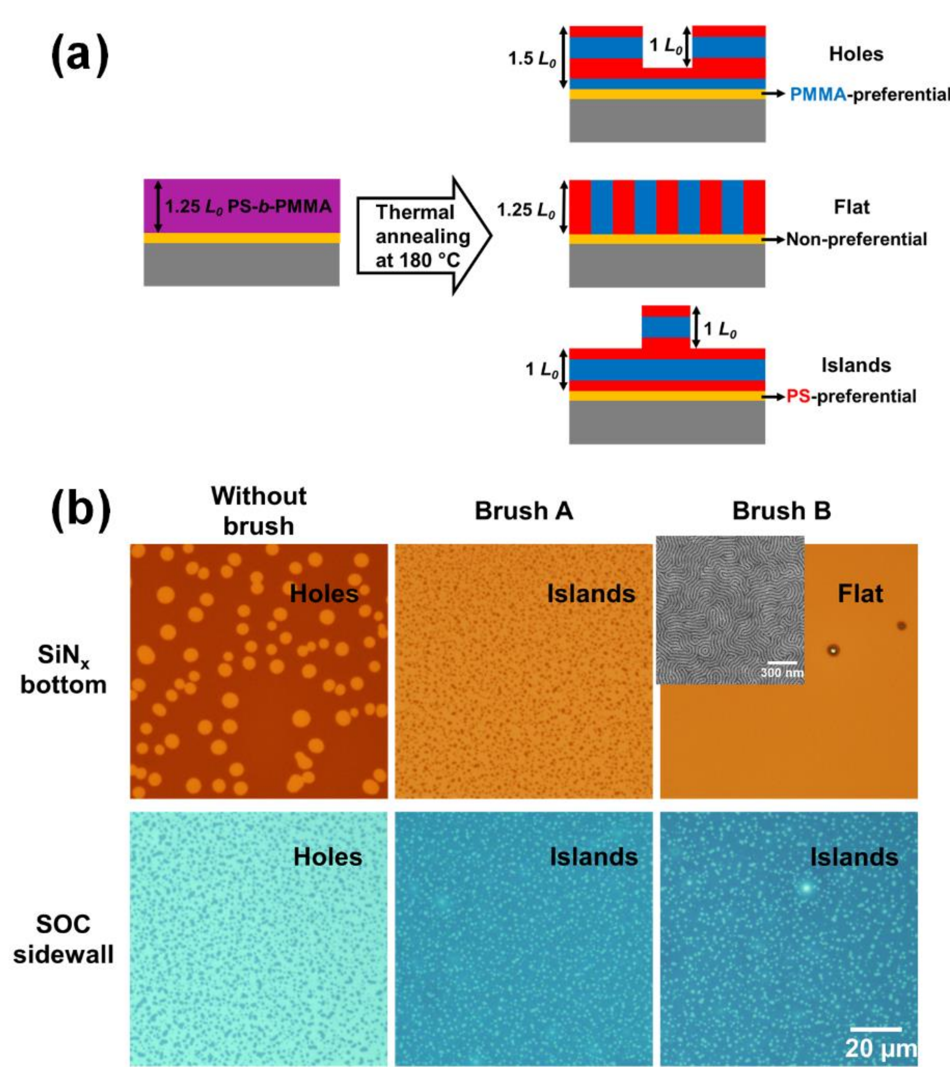

Figure 3-2: (a) Schematic of 1.25 L_0 thick lamella-forming PS-*b*-PMMA films thermally annealed at 180 °C on substrates with different affinity to PS or PMMA. (b) Optical micrographs of 40 nm thick lamellar PS-b-PMMA ($L_0 = 32$nm) thin films on the mimicked SiN_x bottom surface and SOC sidewall surface before and after applying brush A or B. The inset is an SEM image of the perpendicular lamella morphology of the optically flat film.

Table 3-1: Summary of wetting behaviors of bottom and sidewall surfaces

	Without brush	Brush A	Brush B
SiN_x Bottom	PMMA-preferential	PS-preferential	non-preferential
SOC sidewall	PMMA-preferential	PS-preferential	PS-preferential

As summarized in Table 3-1, the brush A makes both sidewall and bottom surface PS-preferential, while brush B makes sidewall surface preferential to PS block and bottom surface non-preferential to PS and PMMA blocks. Two DSA samples was made on SiN_x membrane for TEM characterization with identical DSA procedure except using brush A or B to modify the surface of templates. As shown in Figure 3-3, there is no significant difference in this two samples in top-down SEM images. Both show successful DSA singlets. The bright domain inside of each hole corresponds to the Al_2O_3-stained PMMA cylinder domain while the outer bright domain corresponds to the Al_2O_3-stained outline of the SOC template. The staining effect of the sidewall surface might result from polar components generated on the plasma exposed area during SOC etch. The 2D STEM images revealed more distinct cylinders structures between these two samples. PMMA cylinders in brush A modified sample appear to be more centered and isolated, while in brush B modified samples they show connections to template sidewalls in many holes.

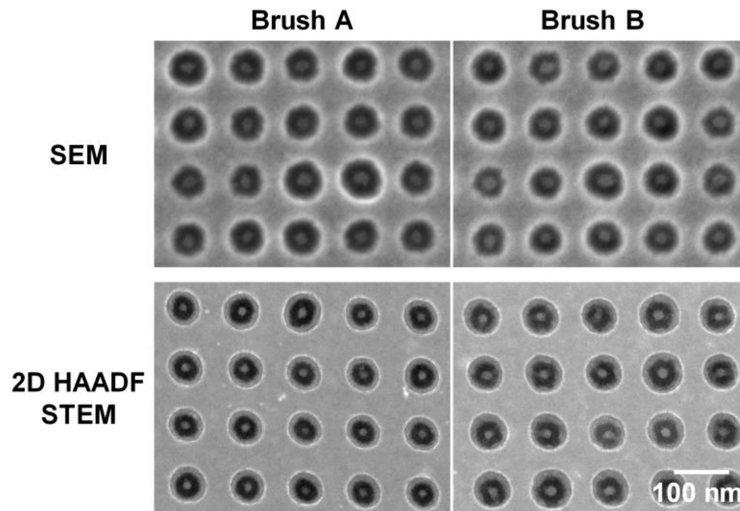

Figure 3-3: Top-down SEM and 2D STEM images of two DSA samples using different brush. In each prepatterned hole, the brighter domains are Al_2O_3-stained PMMA or the sidewall surface and the darker area is PS.

Full STEM tomography is performed to generate entire 3D structures of these two samples. Figure 3-4 shows the reconstruction results. For each sample, three *xy* slices (parallel to the

substrate) displaying 4 × 4 DSA holes are taken from different heights z of the reconstruction volumes where $z = 0$ is defined as the approximate height of bottom of prepatterned holes (or top surface of SiN_x). The 3D visualization of one DSA hole from each sample shown in Figure 3-4 has the Al_2O_3-stained PMMA block colored in blue and the PS block colored in red.

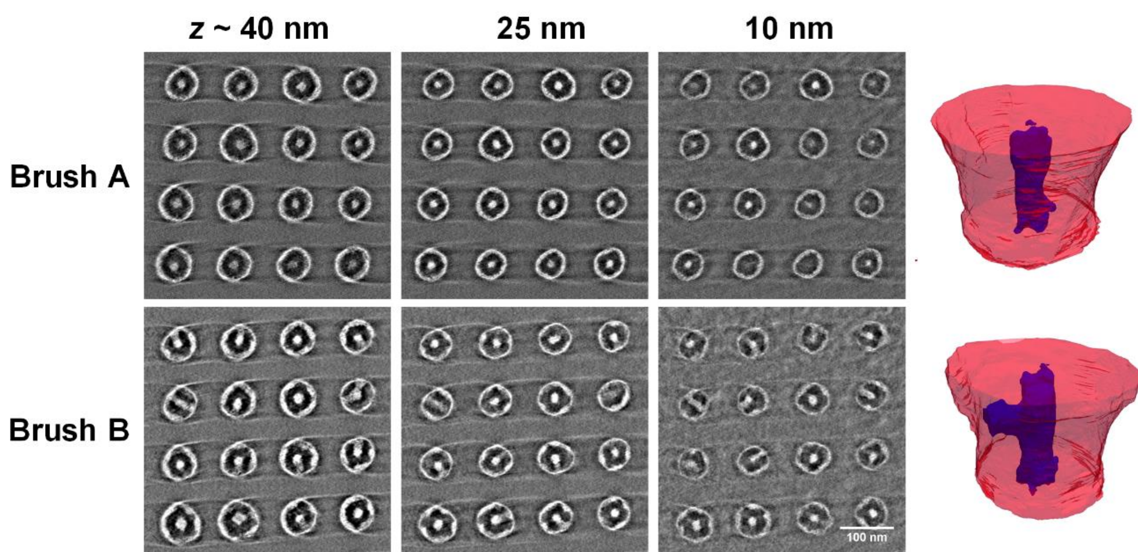

Figure 3-4: STEM tomography reconstruction results of two DSA samples using different brush for surface modification. *xy* slices were taken at three different sample heights z. The brighter domains are Al_2O_3-stained PMMA or the sidewall surface and the darker domains are PS and SOC template. In the 3D visualization, Al_2O_3-stained PMMA is in blue color and PS is in red color.

For the DSA sample using brush A, all PMMA cylinders are at about the center of the template without connecting to sidewall from top to bottom. In the slice at $z = 10$ nm which is close to bottom substrate, only about seven out of sixteen holes ~~still~~ show signals from well-defined PMMA cylinders. It indicates the existence of PS residual layers in the bottom of about 50% of DSA holes. As for the other DSA sample using brush B, the morphologies are distinct through BCP thickness. In the slice taken at $z = 40$ nm where it is slightly beneath the BCP top surface, most of the PMMA cylinders are still relatively close to the center of template while few of them start showing irregular shape and connecting to sidewalls. At $z = 25$ nm where it is approximately

at the height of half of the filled BCP thickness, the bridging to sidewall could be found in most of DSA holes. When $z = 10$ nm, the cylinder domains are ~~still~~ very distorted, but all the holes still show signals from PMMA. This height evolution shows that the brush B sample has more distorted PMMA cylinders and it exhibit many bridge-like defects connecting to SOC sidewall, but all PMMA cylinders reach to bottom substrates and there are much less PS residual defects. The 3D rendering shows the representative DSA results of each brush: the brush A gives vertical cylinder domains; the brush B gives bridging defects connecting to sidewall.

The fact that the DSA sample using brush A has more PS residue defects could be attributed to its PS-preferential bottom surface. For brush B, its non-preferential bottom surface leads to through-film PMMA domains in majority. However, the existence of bridging to sidewalls indicates the wetting behavior of brush B modified sidewall is different. In the ideal DSA singlet, the area fraction of PS (f_{PS}) at the sidewall interface should be 100% when the sidewall surface has much stronger affinity to PS. The bridging defects happen when f_{PS} needs to be decreased to reach minimum interfacial free energy, which implies that the preferentiality of brush B modified sidewall surface to PS decreased.

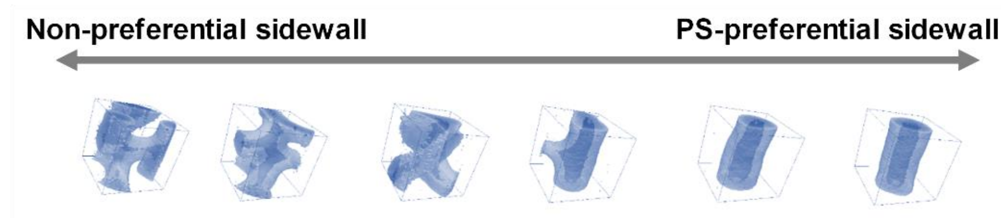

Figure 3-5: Simulation results using coarse-grained model where the volume franction of PMMA is 0.3 and the diameter of confinement is 50 nm (1.32 L0). Only the PMMA block is presented in blue color.

To better understand which surface wetting behavior leads to the bridging defects, a coarse-grained model is used to simulate the DSA results in cylindrical confinement with non-preferential

bottom and altering attraction of sidewall to PS as shown in Figure 3-5. We use the same simulation method described in a previous study.[21] When the sidewall surface is changing from strongly PS-preferential to non-preferential, in simulation the morphology of PMMA changes from a vertical cylinder domain in the center to an expanded and distorted shape with increasing contact area to sidewall. In the middle point where the sidewall surface is slightly PS-preferential, the simulated morphology has vertical cylinder with bridging defect reaching to sidewall, which is similar with our experimental observations of the brush B sample.

Comparing the 3D structures of DSA samples observed from tomography to the simulated morphologies, a more precise description of the surface properties of those two samples would be: brush A makes both sidewall and bottom surface strongly PS-preferential; brush B makes the bottom non-preferential and the sidewall ~~only~~ slightly PS-preferential. It is likely that, when trying to prepare non-preferential bottom surface using a single-brush process, the attraction of sidewall to PS is often sacrificed. When simulation studies encourage to use non-preferential bottom surface to eliminate PS residual layer, it is worth noting that the surface chemistry of sidewall is crucial as well[7,8,10]. It is necessary to keep sidewall surface in the strongly PS preferential region to avoid any distortion of vertical PMMA cylinders.

3.4.3 Effects of geometry

The geometry of graphoepitaxial template also has great impact on the DSA results. The diameter of template must match the periodicity of BCP to form singlets. When sidewall wets the majority block the critical dimension (CD) required is around $1\times L_0$.[25] Considering the thickness of brush grafted to template surface, the CD is often slightly larger than $1\times L_0$ and with certain tolerance judged from the hole open yield.[4,26] The matching between BCP periodicity and CD of template is considered very important as holes too small or too large could result in more PS

residual layer in the bottom and missing holes after pattern transfer.[4] Here we probe several DSA pattern area with different template size using STEM tomography to better understand how the template size affect the quality of DSA in three dimensions.

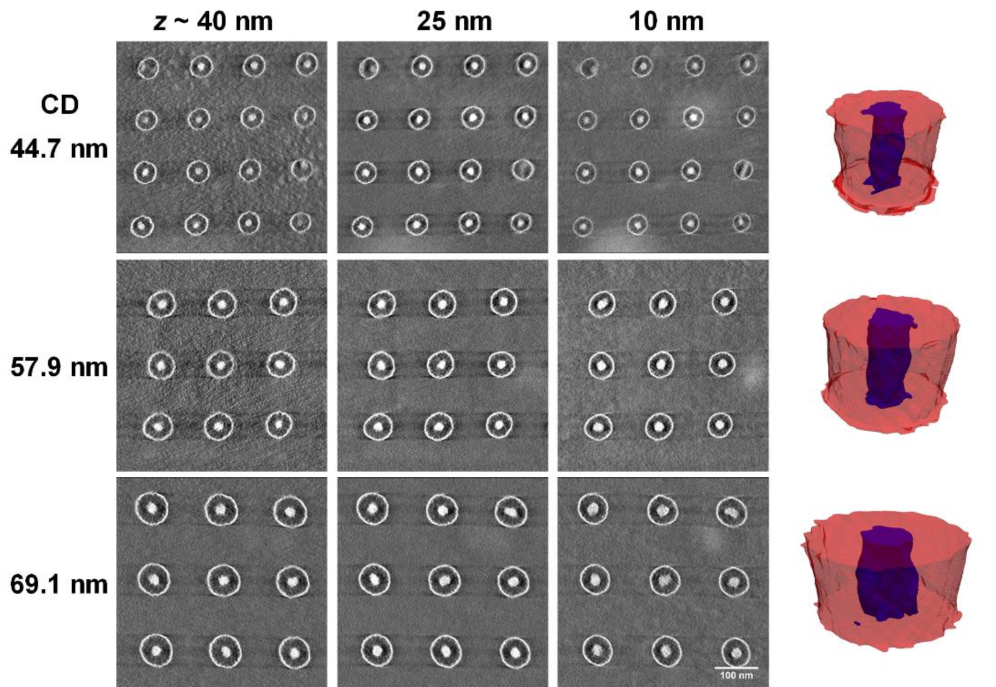

Figure 3-6: STEM tomography results of singlets with different template CD and the representative 3D rendering.

Figure 3-6 shows the tomography results of three DSA area with template CD of 44.7 nm, 57.9 nm and 69.1 nm (as measured from 2D STEM image). This TEM sample is prepared from a 800 μm thick track-processed wafer. The wafer thickness limits the maximum tilting angle in tomography series to 54°. But the reconstruction results are still of good quality and high resolution. These DSA patterns were made through dual-brush process to independently make sidewall surface PS-preferential and bottom surface non-preferential.[14] The reported CD process window for wafer prepared with same DSA conditions is about 47-58 nm.[14] The three pattern area selected has CD smaller than, within, and larger than the reported CD window respectively. Again, *xy* slices

were taken at three different sample heights: close to top of the film at z ~ 40 nm, middle of the film at z ~ 25 nm and relatively bottom of the film at z ~ 10 nm. For all three DSA patterns, PS-residual layer is not observed. Signals from PMMA cylinders are very clear even in the bottom of the film. In the template with CD of 44.7 nm, two out of sixteen DSA holes are defective without well-defined vertical cylinders. When CD is 57.9 nm, all three xy slices look very similar indicates the DSA cylinders are in circular shape and very uniform throughout the thickness. For the largest CD (69.1 nm), most of the DSA cylinders are circular but we notice some cylinders start to show more irregular shape. In the hole at the top right corner, the shape of PMMA cylinder becomes more oval when approaching to the bottom .

These observations verify that, even when the CD of template is outside of the optimized process window, the dual-brush process successfully prevents the formation of PS-residual layer in the bottom. Comparing with the single brush process used in the surface chemistry study, the dual-brush process is more effective to control the sidewall and bottom surface separately and leads to better DSA quality. In terms of the geometry factor, when the CD is smaller than the process window, there isn't obvious PS residual layer in the bottom. However, the DSA morphology goes through a more dramatic change. In some holes the vertical cylinder can't even form, which could be the real cause to the missing singlets[13] after pattern transfer. When is CD is slightly larger than the process window, some cylinders are no longer circular. If this distortion happens in most of the film thickness, it could be etched into underlying substrate, which is not ideal for pattern transfer either.

3.5 Summary

In our study, the DSA hole shrink samples are prepared on SiN_x membrane without damaging polymers and templates. STEM tomography is used to characterize DSA morphologies in three

dimensions with high resolution. Different DSA structures are revealed when the surface of e-beam patterned template is modified differently. Compared to the coarse-grained simulation results, bridging defects connecting the PMMA cylinder with sidewall show up when the sidewall surface is weakly PS-preferential. It is thus important to make sure the attraction of sidewall to PS is still strong enough when trying to make bottom surface non-preferential, which might be more difficult for single-brush process compared to dual-brush process. A singlet DSA hole shrink TEM sample with different template CD sizes was prepared from a 300 mm track-processed wafer and characterized using tomography in a similar approach. Based on collected 3D images, we find that the dual-brush process could effectively avoid PS-residual defects in the bottom over a wide CD range. Several types of defective DSA morphologies are identified as potential attributors to observed pattern transfer defects when CD is outside of the process window.

3.6 References

(1) Ruiz, R.; Kang, H.; Detcheverry, F. A.; Dobisz, E.; Kercher, D. S.; Albrecht, T. R.; De Pablo, J. J.; Nealey, P. F. Density Multiplication and Improved Lithography by Directed Block Copolymer Assembly. *Science (80-.).* **2008**, *321* (5891), 936–939.

(2) Jeong, S. J.; Kim, J. Y.; Kim, B. H.; Moon, H. S.; Kim, S. O. Directed Self-Assembly of Block Copolymers for next Generation Nanolithography. *Materials Today*. **2013**, 468–476.

(3) Yi, H.; Bao, X. Y.; Zhang, J.; Bencher, C.; Chang, L. W.; Chen, X.; Tiberio, R.; Conway, J.; Dai, H.; Chen, Y.; et al. Flexible Control of Block Copolymer Directed Self-Assembly Using Small, Topographical Templates: Potential Lithography Solution for Integrated Circuit Contact Hole Patterning. *Adv. Mater.* **2012**, *24* (23), 3107–3114.

(4) Seino, Y.; Yonemitsu, H.; Sato, H.; Kanno, M.; Kato, H.; Kobayashi, K.; Kawanishi, A.; Azuma, T.; Muramatsu, M.; Nagahara, S.; et al. Contact Hole Shrink Process Using

Graphoepitaxial Directed Self-Assembly Lithography. *J. Micro/Nanolithography, MEMS, MOEMS* **2013**, *12* (3), 033011–033011.

(5) Gharbi, A.; Tiron, R.; Argoud, M.; Chevalier, X.; Barros, P. P.; Nicolet, C.; Navarro, C. Contact Holes Patterning by Directed Self-Assembly of Block Copolymers: Process Window Study. *J. Micro/Nanolithography, MEMS, MOEMS* **2015**, *14* (2), 023508–023508.

(6) Okabe, K.; Yi, H.; Tung, M. C.; Tiberio, R.; Bekaert, J.; Gronheid, R. Cross-Sectional Imaging of Directed Self Assembled Block Copolymers. *SPIE* **2015**, *9423*, 1–9.

(7) Iwama, T.; Laachi, N.; Delaney, K. T.; Kim, B.; Hur, S.; Bristol, R.; Shykind, D.; Weinheimer, C. J.; Fredrickson, G. H. The Hole Shrink Problem: Directed Self-Assembly Using Self-Consistent Field Theory. *J. Photopolym. Sci. Technol.* **2013**, *26* (1), 15–20.

(8) Yoshimoto, K.; Fukawatase, K.; Ohshima, M.; Naka, Y.; Maeda, S.; Tanaka, S.; Morita, S.; Aoyama, H.; Mimotogi, S. Optimization of Directed Self-Assembly Hole Shrink Process with Simplified Model. *J. Micro/Nanolithography, MEMS, MOEMS* **2014**, *13* (3), 031305.

(9) Peters, B. L.; Rathsack, B.; Somervell, M.; Nakano, T.; Schmid, G.; De Pablo, J. J. Graphoepitaxial Assembly of Cylinder Forming Block Copolymers in Cylindrical Holes. *J. Polym. Sci. Part B Polym. Phys.* **2015**, *53* (6), 430–441.

(10) Laachi, N.; Delaney, K. T.; Kim, B. J.; Hur, S.-M.; Bristol, R.; Shykind, D.; Weinheimer, C. J.; Fredrickson, G. H. Self-Consistent Field Theory Investigation of Directed Self-Assembly in Cylindrical Confinement. *J. Polym. Sci. Part B Polym. Phys.* **2015**, *53* (2), 142–153.

(11) Ren, J.; Ocola, L. E.; Divan, R.; Czaplewski, D. A.; Segal-Peretz, T.; Xiong, S.; Kline, R. J.; Arges, C. G.; Nealey, P. F. Post-Directed-Self-Assembly Membrane Fabrication for in Situ Analysis of Block Copolymer Structures. *Nanotechnology* **2016**, *27* (43), 435303.

(12) Segal-peretz, T.; Zhou, C.; Ren, J.; Dazai, T.; Ocola, L. E.; Divan, R. N. S.; Nealey, P. F. Three Dimensional Assembly in Directed Self-Assembly of Block Copolymers. *J. Photopolym. Sci. Technol.* **2016**, *29* (5), 653–657.

(13) Doise, J.; Bekaert, J.; Chan, B. T.; Hori, M.; Gronheid, R. Via Patterning in the 7-Nm Node Using Immersion Lithography and Graphoepitaxy Directed Self-Assembly. *J. Micro/Nanolithography, MEMS, MOEMS* **2017**, *16* (2), 023506.

(14) Doise, J.; Chan, B. T.; Hori, M.; Gronheid, R. Dual Brush Process for Selective Surface Modification in Graphoepitaxy Directed Self-Assembly. **2017**, *16* (3), 101460R.

(15) Segal-Peretz, T.; Winterstein, J.; Doxastakis, M.; Ramírez-Hernández, A.; Biswas, M.; Ren, J.; Suh, H. S.; Darling, S. B.; Liddle, J. A.; Elam, J. W.; et al. Characterizing the Three-Dimensional Structure of Block Copolymers via Sequential Infiltration Synthesis and Scanning Transmission Electron Tomography. *ACS Nano* **2015**, *9* (5), 5333–5347.

(16) Matsen, M. W.; Schick, M. Stable and Unstable Phases of a Linear Multiblock Copolymer Melt. *Macromolecules* **1994**, *27* (24), 7157–7163.

(17) Fredrickson, G. *The Equilibrium Theory of Inhomogeneous Polymers*; 2007.

(18) Detcheverry, F.; Pike, D.; Nealey, P.; Müller, M.; De Pablo, J. Monte Carlo Simulation of Coarse Grain Polymeric Systems. *Phys. Rev. Lett.* **2009**, *102*, 2–5.

(19) Detcheverry, F. A.; Kang, H.; Daoulas, K. C.; Müller, M.; Nealey, P. F.; De Pablo, J. J. Monte Carlo Simulations of a Coarse Grain Model for Block Copolymers and Nanocomposites. *Macromolecules* **2008**, *41* (13), 4989–5001.

(20) Detcheverry, F. A.; Liu, G.; Nealey, P. F.; De Pablo, J. J. Interpolation in the Directed Assembly of Block Copolymers on Nanopatterned Substrates: Simulation and Experiments. *Macromolecules* **2010**, *43* (7), 3446–3454.

(21) Bezik, C. T.; Garner, G. P.; de Pablo, J. J. Mechanisms of Directed Self-Assembly in Cylindrical Hole Confinements. *Macromolecules* **2018**, *51* (7), 2418–2427.

(22) Dixit, D.; Green, A.; Hosler, E. R.; Kamineni, V.; Preil, M. E.; Keller, N.; Race, J.; Chun, J. S.; O'Sullivan, M.; Khare, P.; et al. Optical Critical Dimension Metrology for Directed Self-Assembly Assisted Contact Hole Shrink. *J. Micro/Nanolithography, MEMS, MOEMS* **2016**, *15* (1), 014004.

(23) Segal-Peretz, T.; Ren, J.; Xiong, S.; Khaira, G.; Bowen, A.; Ocola, L. E.; Divan, R.; Doxastakis, M.; Ferrier, N. J.; De Pablo, J.; et al. Quantitative Three-Dimensional Characterization of Block Copolymer Directed Self-Assembly on Combined Chemical and Topographical Prepatterned Templates. *ACS Nano* **2017**, *11* (2), 1307–1319.

(24) Suh, H. S.; Kang, H.; Nealey, P. F.; Char, K. Thickness Dependence of Neutral Parameter Windows for Perpendicularly Oriented Block Copolymer Thin Films. *Macromolecules* **2010**, *43* (10), 4744–4751.

(25) Doise, J.; Bekaert, J.; Chan, B. T.; Gronheid, R.; Cao, Y.; Hong, S.; Lin, G.; Fishman, D.; Chakk, Y.; Marzook, T. Implementation of Surface Energy Modification in Graphoepitaxy Directed Self-Assembly for Hole Multiplication. *J. Vac. Sci. Technol. B, Nanotechnol. Microelectron. Mater. Process. Meas. Phenom.* **2015**, *33* (6), 06F301.

(26) Delgadillo, P. A. R. Implementation of a Chemo-Epitaxy Flow for Directed Self-Assembly on 300-Mm Wafer Processing Equipment. *J. Micro/Nanolithography, MEMS, MOEMS* **2012**, *11* (3), 031302.

CHAPTER 4: COMBINING DOUBLE PATTERNING WITH SELF-ASSEMBLED BLOCK COPOLYMER LAMELLAE TO FABRICATE 10 NM FULL-PITCH LINE/SPACE PATTERNS

4.1 Abstract

Directed self-assembly of block copolymers and self-aligned double patterning are two commonly used pitch scaling techniques to increase the density of lithographic features. In this work, the combination of both these pitch scaling techniques was investigated to pattern at even higher densities. In this process, the line/space patterned formed by the directed self-assembly of a high-χ block copolymer were used to template mandrels and a thin aluminium oxide spacer film was deposited by atomic layer deposition. By this method, a total pitch scaling factor of 8, equivalent to a 10.5 nm full pitch, was reached. The types of defects and the roughness evolution of the process were discussed.

4.2 Introduction

The hard disk drive industry is facing challenges to further extend the capability of conventional recording media.[1] According the technology roadmap given by the Advanced Storage Technology Consortium (ASTC, http://www.idema.org/?page id=3193), energy assisted recording such as heat-assisted magnetic recording (HAMR)[2,3] is targeted to increase the areal density above 2 Tb/in^2. To go beyond 5 Tb/in^2, the targeted innovation is the heated-dot magnetic recording (HDMR) technology augmented by bit patterned media (BPM). BPM cuts a continuous magnetic layer to the size of one bit, which helps to maintain high signal-to-noise ratio and good thermal stability while increasing bit density.[4–6] The reduction in the bit size is a challenge for existing lithography techniques. The density of 5 Tb/in^2 corresponds to an 11 nm bit period. Increasing the density to 10 Tb/in^2 requires a further reduction of bit period to 8 nm, which is beyond the capabilities of

even cutting-edge semiconductor fabrication processes.[7] Media fabrication based on nanoimprint lithography has been developed to increase the throughput and reduce the cost.[6,8,9] However, due to the bit size variation and low throughput of techniques as advanced as e-beam lithography, it is difficult to generate highly uniform dots arrays with a density higher than 5 Tb/in^2 when fabricating a nanoimprint master template.[10]

Directed self-assembly (DSA) of block copolymers (BCPs)[11,12] and self-aligned double patterning (SADP)[13,14] are promising potential solutions for patterning high resolution unidirectional lines. Both technologies are commonly used to increase the feature density of lithographic templates. It has been shown that DSA based on poly(styrene-*b*-methyl methacrylate) (PS-*b*-PMMA) can be used to create a 28 nm pitch line/space pattern on 84 nm pitch chemical contrast pattern prepared by 193 nm immersion photolithography (193i).[15] The combination of 193i and SADP has been used in high volume manufacturing to convert 80 nm pitch photoresist lines to 40 nm pitch line/space patterns.[16] However, it remains challenging to reliably pattern 10 nm pitch features using these techniques. For DSA on the 193i prepattern which has a resolution limit of approximately 70-80 nm[17], a multiplication factor as large as 8 would be necessary. It is important to note that challenges arise not only from the limited selection of suitable BCP materials[18], but also from the increase in defect density when the density multiplication factor increases.[19,20] On the other hand, SADP alone is not enough to shrink the photolithographic resolution to 10 nm. Self-aligned quadruple patterning (SAQP), or even self-aligned octuple patterning (SAOP) would be needed, both of which would necessitate a number of additional etching and deposition steps with extremely narrow process tolerances.[21,22] One potential path to further subdivide the pitch is extending the DSA lithography with a subsequent SADP process.[6] This strategy has been studied using PS-*b*-PMMA.[23,24] Due to its relatively small Flory Huggins

parameter, χ the PS-*b*-PMMA alone has a resolution limit around 22 nm full pitch.[25] Dallorto et al.[23,24] demonstrated that the pitch for a self-assembled PS-*b*-PMMA system could be reduced from 30 nm to 15 nm upon applying an additional SADP step. To further reduce the pitch and achieve even higher bit areal density, using this approach combined with "high χ" block copolymers other than PS-*b*-PMMA in the first DSA step could be effective.

In this study, we investigate the potential to create a unidirectional line/space pattern with a pitch as small as 10.5 nm by combining DSA of a high χ block copolymer and the SADP approaches. The high χ block copolymer used here is a lamellar poly(2-vinylpyridine-b-styrene-b-2-vinylpyridine) (P2VP-*b*-PS-*b*-P2VP) with a pitch (L_0) of about 21 nm. After the DSA step, the P2VP domains can be converted into hard mask materials using a process called sequential infiltration synthesis (SIS).[26,27] By this technique, trimming mandrels to the desired width following spacer deposition can be easily accomplished because the resulting AlO_x line dimensions are controllable. We further simplified this process by using spin-on films as sacrificial layers. Starting from 84 nm pitch prepattern, a total density multiplication factor of 8 was demonstrated. In addition, the defectivity and line roughness were thoroughly investigated to identify the manufacturing challenges.

4.3 Experimental

4.3.1 Stack preparation

The stack for SADP was prepared by spin-coating SOC solution TOK-CDN018R (TOK) on a Si substrate and baking it at 205°C for 1 min to form a 15 nm thick SOC layer. Then, a SOG solution TOK-CDN020R (TOK) was spin-coated and baked at 205°C for 1 min to form a 10 nm thick SOG layer on top of the SOC. Both these prepared SOC and SOG films are inert to the organic solvents used in this study. The SOC is inert to buffered oxide etchant (BOE) wet

chemistry. The SOG layer was hydrophobic after baking and was descummed in oxygen plasma for 10 s to ensure good wetting of polymer films.

4.3.2 DSA sample preparation

The DSA pattern of P2VP-*b*-PS-*b*-P2VP was prepared using a similar method as reported previously.[9,28] The 8 nm thick crosslinkable PS mat was prepared on the SOG/SOC stack by spin coating it with TOK-CIN01-01R (obtained from TOK), followed by crosslinking at 250 °C for 10 min under N_2. A 60 nm thick gl-2000 (Gluonlab) e-beam resist layer was coated on the PS mat and patterned with 84 nm pitch lines by a JEOL 9300 E-beam lithography system with different doses and then developed in *n*-amyl acetate for 15 s. O_2 plasma based reactive ion etching (RIE) in a PlasmaTherm ICP Fluorine Etch was used to etch and trim the PS mat using the e-beam resist patterns as mask. The remaining e-beam resist was stripped in *N*-methyl pyrrolidone. The exposed SOG was modified by low molecular weight hydroxyl-terminated PS brush (PS-OH, M_n = 1.2 kg/mol, purchased from Polymer Source). 20 nm of P2VP-*b*-PS-*b*-P2VP (M_n = 12k-*b*-23k-*b*-12k, purchased from Polymer Source) was coated and annealed in acetone vapor for 1 hour with swelling ratio kept at ~42%. Al_2O_3 sequential infiltration synthesis (SIS) was performed by exposing samples with trimethylaluminum (TMA)/H_2O vapor alternatively at 90°C in in Arradiance Gemstar ALD system to selectively grow Al_2O_3 in polar P2VP domains. The polymers were then removed by O_2 plasma to generate dense AlO_x lines.

4.3.3 SADP

AlO_x lines were transferred first into SOG, then into SOC, using CF_4 and O_2 based RIE respectively. The SOG and AlO_x were stripped by dipping in buffered oxide etchant for 15 s. The samples were then thoroughly rinsed in water. The SOC lines were left as mandrels. For spacer deposition, 5 nm of ALD Al_2O_3 film were conformally deposited onto the SOC mandrels. The

spacers were etched back using an inductively coupled plasma (ICP) RIE with a mixture gas of BCl_3 and Ar. Afterward, the SOC was removed by O_2 plasma.

4.3.4 Characterization and image analysis

Scanning electron microscopy (SEM) was performed on a Carl Zeiss Merlin SEM using the InLens detector at 2 kV voltage. Raw SEM images were denoised and thresholded using a Python script[29]. From the thresholded images, the edges and centers of domains were extracted. The placement error was defined as the deviation of the line center about the mean placement for each line. The line width error was defined as the deviation of the edges about the closest center of the line, and line edge error was defined as the deviation of the edges about the mean position of the line. These deviations are naturally binned as they are defined by the pixel grid of the SEM. The line edge roughness (LER), line width roughness (LWR) and line placement roughness (LPR) were calculated respectively by fitting their deviations with a simple gaussian.[23]

4.4 Results and discussion

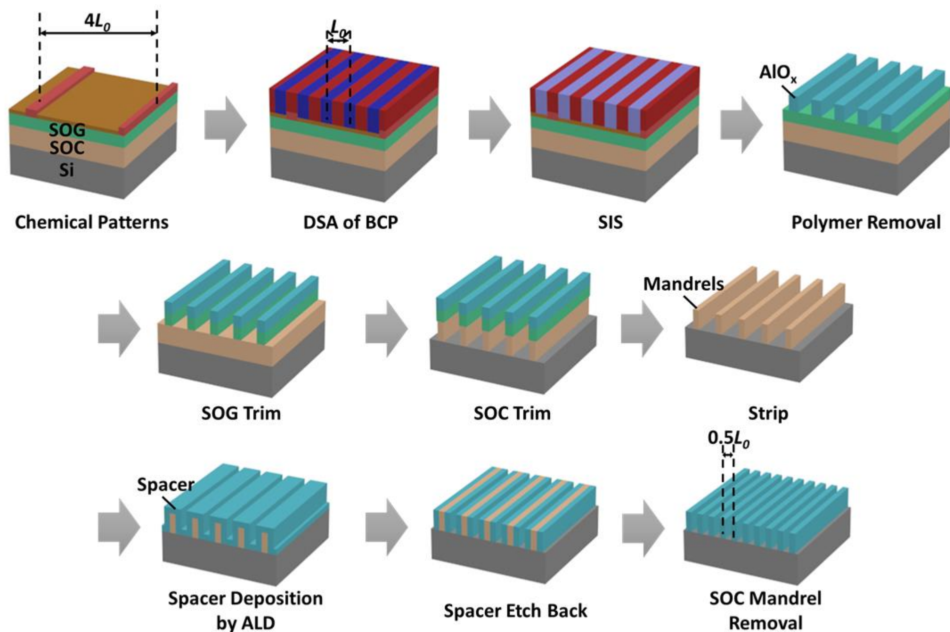

Figure 4-1: Process flow of combining DSA and SADP approaches to reach the total density pitch scaling factor of 8

4.4.1 Fabrication process of combining DSA and SADP approaches

Figure 4-1 depicts the process flow of forming 8 times denser line/space patterns through DSA and SADP. DSA of P2VP-*b*-PS-*b*-P2VP was performed on chemical patterns using LiNe flow[11,30] on a substrate coated with SOG/SOC films. Starting with guiding stripes patterned by e-beam lithography with a pitch of 4 L_0, the BCP lamella formed a DSA pattern with a pitch of L_0 on top.[28] A multiplication factor of 4 was achieved. P2VP domains were selectively converted to AlO_x lines by sequential infiltration synthesis (SIS) and O_2 plasma treatment.[9,31] SOG/SOC layers were etched and trimmed by dry etch with AlO_x lines as the etch mask. After stripping AlO_x and SOG by wet etch, SOC mandrels were left. For spacer deposition, an Al_2O_3 film was conformally deposited onto the SOC mandrels by ALD. After the spacer etch back, the SOC mandrels were removed, leaving two spacer lines for each mandrel line. This SADP process provided another factor of 2 using the mandrels defined by the DSA pattern. A total density multiplication factor of 8 was realized.

The SADP process utilizing ALD spacers we used in this study was adapted from techniques reported by Doerk *et al*[23] and Dallorto *et al*[24]. Instead of using 20-25 nm sputtered carbon and 5-7 nm SiO_2,[23,24] we used ~15 nm SOC and ~10 nm SOG to assist the pattern transfer from BCP pattern to SOC mandrels. The thickness was adjusted based on the L_0 of BCP. One crucial step in SADP is trimming the width of the mandrels to about 0.25 L_0, which requires the BCP has good pattern transfer capability. Previously, P2VP-*b*-PS-*b*-P2VP combined with sequential infiltration synthesis has been used to pattern lines with tunable line width.[31] The thin SOG layer is necessary to protect the SOC when removing the polymers and forming AlO_x lines in oxygen plasma after SIS. The SOC mandrels can be further trimmed during dry etch to decrease the width of mandrels

with AlO_x/SOG masks. We would like to emphasize that the spin-on films are much easier to prepare compared to the sputtered films in earlier studies[23,24], but work almost identically.

We first tested the SADP process on self-assembled P2VP-*b*-PS-*b*-P2VP pattern. Figure 4-2 shows the spacer lines formed after SADP. The peak in 2D fast Fourier transform (FFT) pattern verifies that the pitch of spacer lines is 10.5 nm (0.5 L_0). It is worth noting that, although from top-down SEM (Figure 4-2(a)) the spacer lines are evenly distributed, there is "pitch-walking" (alternating pitch distribution) visible in the cross-sections (Figure 4-2(b)). The pitch-walking is caused by the slope of mandrel sidewalls and spacer lines tilting towards the trench side, and it makes further pattern transfer more difficult. By optimizing the SOC etching and improving the mechanical stability of spacer lines, the problem of pitch-walking might be solved. However, optimizing the process at such small dimensions in lab-scale experiments is prohibitively nontrivial, and thus not included in this work. The discussion below is only based on the top-down lateral observations.

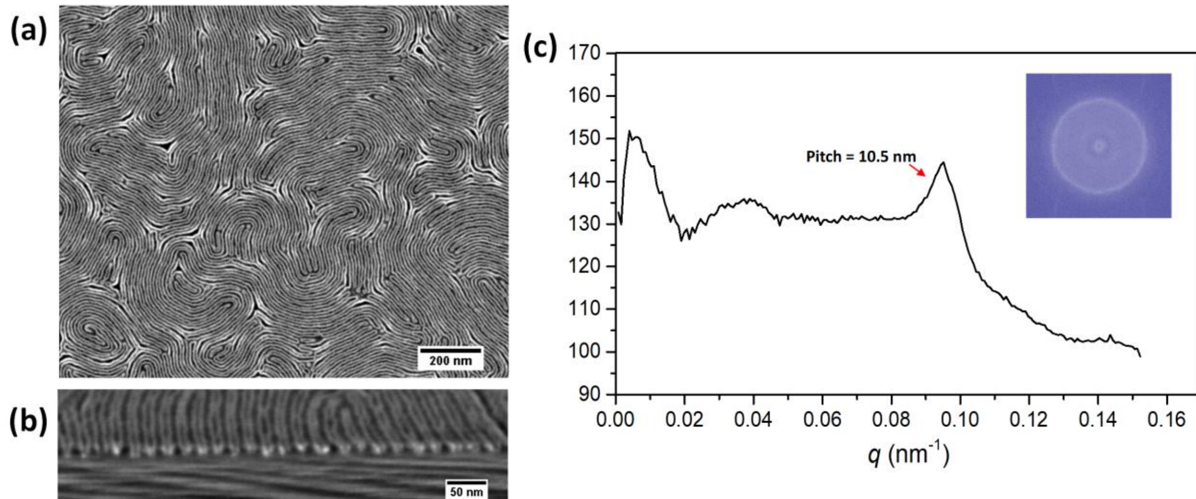

Figure 4-2: SADP results using solvent annealed P2VP-*b*-PS-*b*-P2VP self-assembly patterns. Top-down (a) and cross-sectional (b) SEM images of the Al_2O_3 spacer lines. (c) FFT spectrum showing the pitch of the Al_2O_3 spacer lines are 10.5 nm.

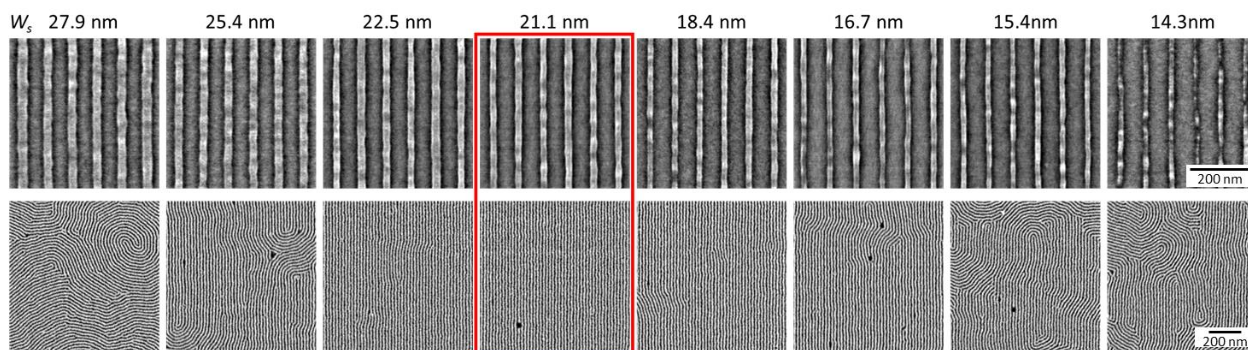

Figure 4-3: DSA result of solvent annealed P2VP-*b*-PS-*b*-P2VP (L_0=21 nm) on 84 nm pitch chemical pattern made by E-beam lithography with guiding stripes trimmed to different width W_s. DSA was successful when W_s =21.1 nm (red frame).

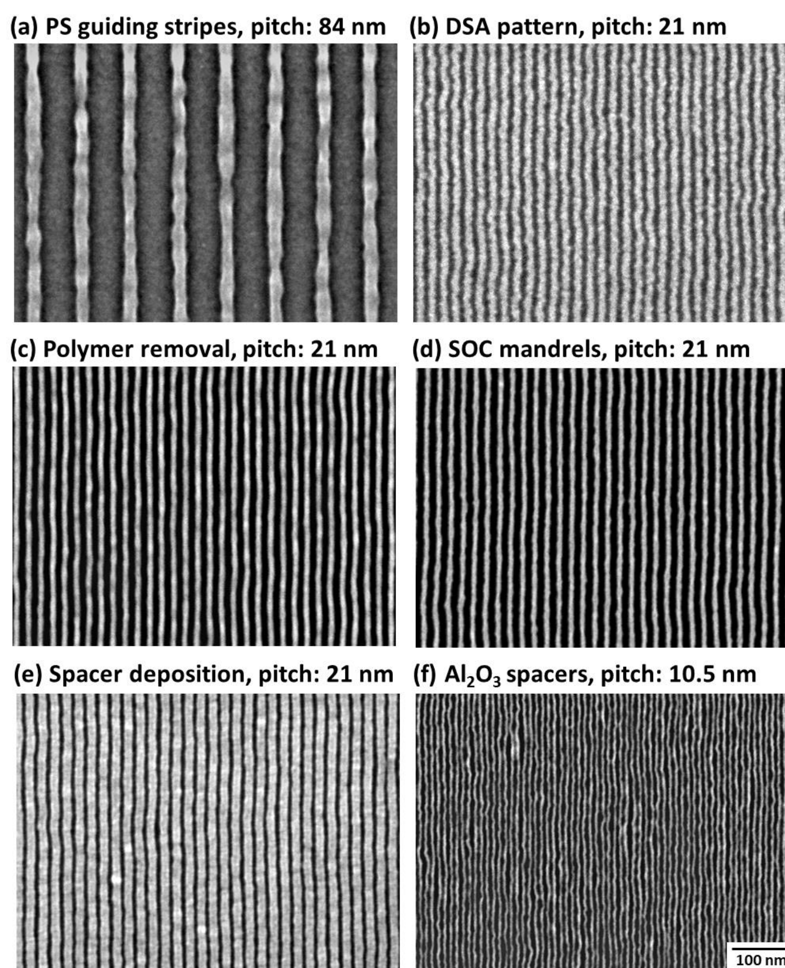

Figure 4-4: Representative top-down SEM images and corresponding full-pitch of line/space patterns of (a) E-beam patterns after trim etch; (b) DSA of P2VP-*b*-PS-*b*-P2VP after SIS; (c) AlO_x lines after polymer removal; (d) SOC mandrels; (e) ALD spacer deposited on mandrels; (f) final Al_2O_3 spacer lines after etching back

To apply the developed SADP process to oriented line and space patterns, the same P2VP-*b*-PS-*b*-P2VP was first directed self-assembled on chemical patterned made by e-beam lithography using a reported procedure.[28] As shown in Figure 4-3, the degree of alignment changed with the width of e-beam patterned guiding stripes W_s. When W_s is around 21.1 nm as measured from top-down SEM images, the DSA was successful and free of dislocation defects over a large area. This DSA pattern was used for the further SADP process, the results of which are presented in Figure 4-4.

Beginning this process with 84 nm pitch guiding stripes (patterned by e-beam lithography) resulted in post-DSA lines that increased in spatial density by a factor of four. These DSA lines were then successfully transferred into the SOC layer to form SOC mandrels, which were spaced at an identical pitch to L_0, 21 nm. After ALD spacer deposition and etch back, each mandrel line was split into two spacer lines, which reduced the pitch to 10.5 nm. To ensure the spacer lines are distributed symmetrically, it is critical to trim the SOC mandrels to correct dimensions. Figure 4-5 shows an example of the SADP results when the SOC mandrels were not trimmed enough. When the width of SOC mandrels approaches ~9 nm, they begin to merge after ALD spacer deposition, which results in the final spacer lines pitch walking and bridging between every two lines.

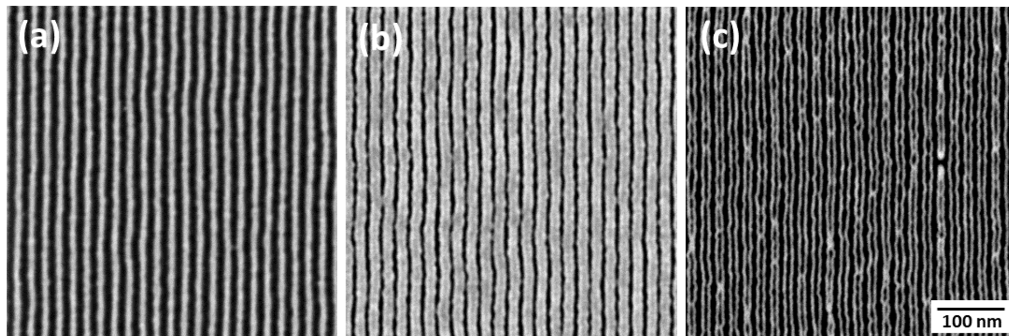

Figure 4-5: Top-down SEM images of (a) SOC mandrels with average line width of ~9 nm and (b) the morphology after 5 nm ALD Al_2O_3 spacer deposition and (c) the resulting Al_2O_3 spacer lines after etching back

4.4.2 Defect tracking

SEM observation was used to assembly a gallery of possible defects at each processing step. Figure 4-6 illustrates the major defect modes. For the DSA film (Figure 4-6(a)), typical defect types included P2VP line breakage, as well as gaping between adjacent P2VP stripes corresponding to abnormally wide points in a PS domain. Defects of the latter type could arise from impurities in the source polymer. The line breakage defects persist through the entire P2VP thickness (as reported by Segal-Peretz *et al.*[28]), and are recognized as one of the most common defects in PS-*b*-PMMA DSA flow[32].Neither defect type is eliminated during subsequent processing steps, including polymer removal, SOC mandrel formation, and spacer deposition (Figure 4-6(b-d)). Both the merged and the broken SOC mandrel lines lead to breakage and pairs of end loops in spacer lines. On the contrary, some SOC mandrels with residues start to merge and make contact after spacer deposition and lead to continuous but bridging spacer lines.

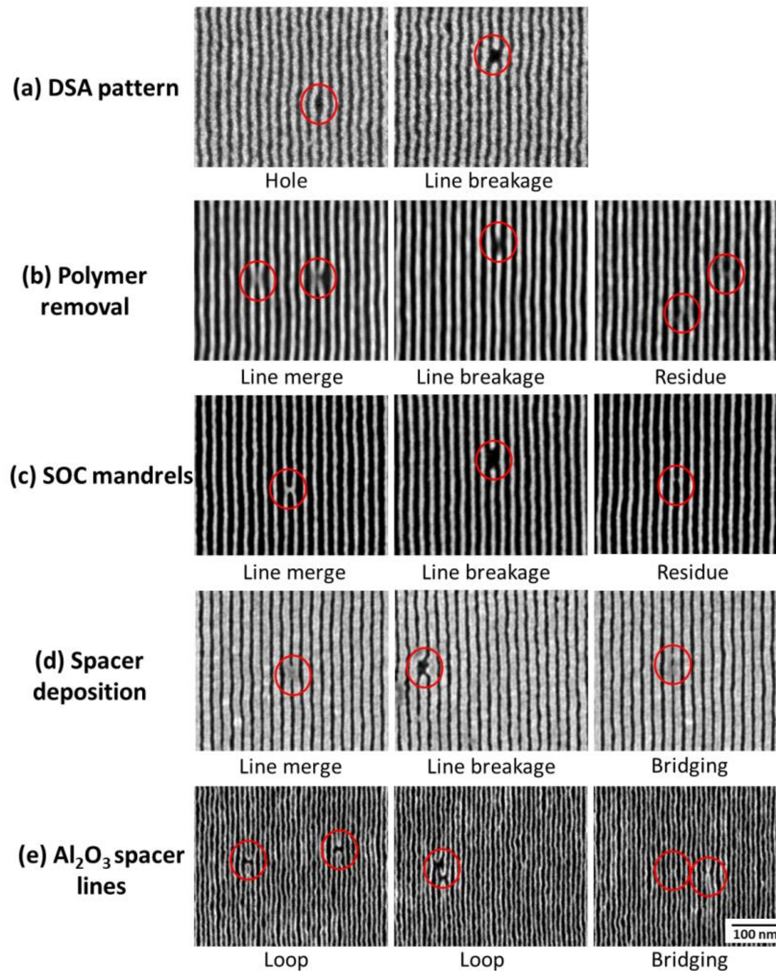

Figure 4-6: Defect gallery collected from SEM images of (a) DSA pattern, (b)polymer removal, (c) SOC mandrels, (d) spacer deposition and (e) Al_2O_3 spacer lines

It is important to note that defect analysis for this combined process is much more challenging than for either process individually, as both DSA and SADP give rise to different types of defects. For DSA specifically, high defect density has long been the major concern in applying it to industrial high-volume manufacturing.[32] Recent studies have suggested that the defects that form during the DSA process, in addition to being due in part to material impurities, could be kinetically trapped metastable states during annealing.[32–34] The conjugation of both these factors, and the uncertainty regarding the specific nature of how defects are formed and eliminated in DSA structures, makes defect analysis and application toward manufacturing particularly challenging.

Defects arising from the SADP step are relatively more trackable as the process is widely studied and popular in semiconductor manufacturing, but the extremely small feature size makes the defect analysis of this step very difficult.[35] For this combined DSA and SADP patterning method to be applied to high volume semiconductor manufacturing, the process must be further optimized to minimize defects. Advanced high-volume metrology techniques with resolutions suitable for the length scales of the defects must be developed.

4.4.3 Line roughness analysis

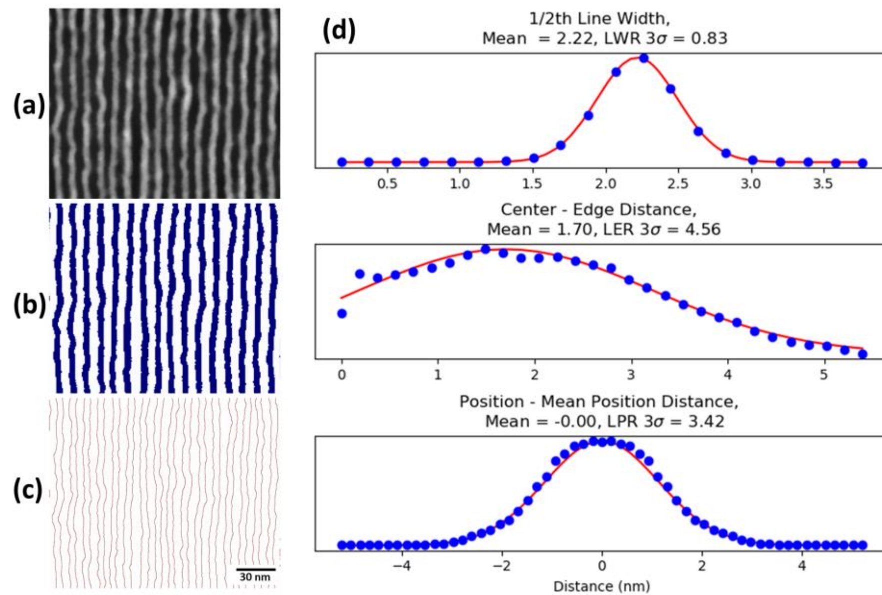

Figure 4-7: Example image of ALD spacer lines for roughness analysis: (a) the original SEM image, (b) binary image after thresholding, (c) extracted line edges. (d) The binned distribution of LWR, LER and LPR (blue) and fitting curves (red) measured from SEM image

In addition to defect analysis, it is important to characterize the roughness of spacer lines, which is directly related to the uniformity of bit size and placement. A bit size distribution and placement accuracy of less than 5% is required to ensure good write synchronization and bit addressability at ultra-high bit densities.[6,36,37] To evaluate and quantify the roughness of line and space patterns, we calculated line width roughness (LWR), line edge roughness (LER) and line placement roughness (LPR) from SEM images taken at each process step. LWR estimates the uniformity of the

dimension of lines, which influences the uniformity of future bit size. LPR describes the waviness of lines, which causes bit placement error. The waviness of edges is also important, as the edge roughness of mandrel lines directly relates to the placement roughness of spacer lines, so it is necessary to take LER into account as well. Figure 4-7 shows how we extract the edges and calculate three different roughness using the raw SEM image of ALD spacer lines as an example. The same approach was applied to six different steps in accordance with Figure 4-4. The 3σ values for LWR, LER and LPR are displayed in Figure 4-8 and Table 4-1.

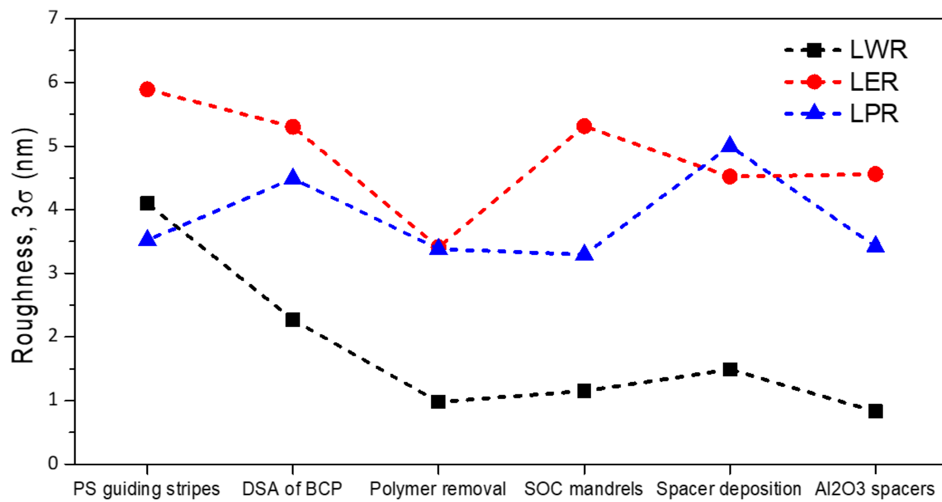

Figure 4-8: Measured line roughness at each process step

Table 4-1: Measured line width and line roughness values after each process

	Line width (nm)	LWR, 3σ (nm)	LER, 3σ (nm)	LPR, 3σ (nm)
PS guiding stripes	21.08	4.10	5.89	3.52
DSA of BCP	10.00	2.27	5.30	4.49
Polymer removal	9.06	0.98	3.41	3.38
SOC mandrels	7.92	1.15	5.31	3.29
Spacer deposition	12.40	1.49	4.52	5.00
Al_2O_3 spacers	4.52	0.83	4.56	3.42

The LWR decreased over 75%: The 3σ of spacer lines is as small as 0.75 nm compared to 4.1 nm for the initial e-beam patterned lines. The LWR significantly improved in the DSA pattern as

measured after SIS and polymer removal. LWR slightly increased when transferring lines to SOC mandrels and Al_2O_3 spacer deposition but decreased again when forming spacer lines. Both the BCP domain size and ALD deposition thickness were highly uniform which attributed to the trend of LWR decreasing. The 1σ of the spacer line width distribution is 6.1% of the average spacer line width, which is close to the tolerance for bit size uniformity to ensure the narrow switching field distribution.[37]

However, both LER and LPR remained at a high level throughout the whole process. The sidewalls of the e-beam exposed guiding stripe pattern were quite rough (3σ LER: 5.89 nm). As the DSA is believed to be mainly guided by the sloped sidewalls of the guiding stripes, the position of BCP lamella varied accordingly[28,38]. The LER and LPR were neither improved after SADP. Because the pitch of spacer lines was much smaller, the 1σ distribute on position of the spacer lines distribution is as high as 10.9% of the pattern pitch. Such high LPR will result in overwriting adjacent bits and poor bit addressability. It is more of challenge to reduce the LPR of spacer lines because the root cause is the roughness of the e-beam lithography template. Xiong et al. found that the roughness of DSA lines changes as the BCPs are stretched /compressed.[9] For the BCP used in this study, 3σ LER and LPR after DSA, SIS and polymer removal were less than 2 nm when they optimized the guiding stripes.[9] Assuming the LPR of spacer lines remains similarly, it is promising to drop the 1σ of the spacer lines' position distribution down to around 6.3% of the pitch size, which is close to the tolerance for bit placement accuracy.

4.5 Summary and conclusions

In conclusion, we demonstrated that combining the block-copolymer DSA and SADP processes that line and space patterns with a full-pitch as small as 10.5 nm can be fabrication Starting with DSA of a high χ BCP (L_0 = 21 nm) on 84 nm pitch chemical contrast pattern prepared by e-beam

lithography, mandrel lines made of spin-on-carbon material were transferred from assembled lamellae followed by vapor infiltration of hard mask material. After depositing and etching back ALD Al_2O_3 spacers, the number of lines was doubled and a total density multiplication factor of 8 was achieved with respect to the original sparse guiding pattern. This process holds promise to address the challenge of fabricating bit-patterned media with bit densities beyond 5 Tb/in^2.

Analyses of the observed defects and line roughness showed that extensive further work in process optimization will be required in order to meet the tight tolerances in bit size and placement accuracy needed for bit-patterned media. The ALD deposited spacer film resulted in highly uniform line widths with 1σ only as small as 6.3% of the average line width. However, the line position roughness with 1σ 10.9% of the pattern pitch, which is caused by line edge roughness of the e-beam guiding pattern, is far larger than what is required by bit-patterned media. We envision that the pattern quality will improve if the defects and roughness in DSA patterns are greatly reduced by process optimization in future work.

4.6 References

(1) Moser, A.; Takano, K.; Margulies, D. T.; Albrecht, M.; Sonobe, Y.; Ikeda, Y.; Sun, S.; Fullerton, E. E. Magnetic Recording: Advancing into the Future. *J. Phys. D. Appl. Phys.* **2002**, *35* (19), 157–167.

(2) Challener, W. A.; Peng, C.; Itagi, A. V.; Karns, D.; Peng, W.; Peng, Y.; Yang, X.; Zhu, X.; Gokemeijer, N. J.; Hsia, Y.-T.; et al. Heat-Assisted Magnetic Recording by a near-Field Transducer with Efficient Optical Energy Transfer. *Nat. Photonics* **2009**, *3* (4), 220–224.

(3) Pan, L.; Bogy, D. B. Heat-Assisted Magnetic Recording. *Nat. Photonics* **2009**, *3* (4), 189–190.

(4) Stipe, B. C.; Strand, T. C.; Poon, C. C.; Balamane, H.; Boone, T. D.; Katine, J. A.; Li, J.-

L.; Rawat, V.; Nemoto, H.; Hirotsune, A.; et al. Magnetic Recording at 1.5 Pb M−2 Using an Integrated Plasmonic Antenna. *Nat. Photonics* **2010**, *4* (7), 484–488.

(5) Richter, H. J.; Dobin, A. Y.; Heinonen, O.; Gao, K. Z.; v.d. Veerdonk, R. J. M.; Lynch, R. T.; Xue, J.; Weller, D.; Asselin, P.; Erden, M. F.; et al. Recording on Bit-Patterned Media at Densities of 1 Tb/In^{2}and Beyond. *IEEE Trans. Magn.* **2006**, *42* (10), 2255–2260.

(6) Albrecht, T. R.; Arora, H.; Ayanoor-Vitikkate, V.; Beaujour, J.-M.; Bedau, D.; Berman, D.; Bogdanov, A. L.; Chapuis, Y.-A.; Cushen, J.; Dobisz, E. E.; et al. Bit-Patterned Magnetic Recording: Theory, Media Fabrication, and Recording Performance. *IEEE Trans. Magn.* **2015**, *51* (5), 1–42.

(7) Piramanayagam, S. N.; Chong, T. C. *Developments in Data Storage*; Piramanayagam, S. N., Chong, T. C., Eds.; John Wiley & Sons, Inc.: Hoboken, NJ, USA, 2011.

(8) Wan, L.; Ruiz, R.; Gao, H.; Patel, K. C.; Lille, J.; Zeltzer, G.; Dobisz, E. A.; Bogdanov, A.; Nealey, P. F.; Albrecht, T. R. Fabrication of Templates with Rectangular Bits on Circular Tracks by Combining Block Copolymer Directed Self-Assembly and Nanoimprint Lithography. *J. Micro/Nanolithography, MEMS, MOEMS* **2012**, *11* (3), 031405-1.

(9) Xiong, S.; Chapuis, Y.-A.; Wan, L.; Gao, H.; Li, X.; Ruiz, R.; Nealey, P. F. Directed Self-Assembly of High-Chi Block Copolymer for Nano Fabrication of Bit Patterned Media via Solvent Annealing. *Nanotechnology* **2016**, *27* (41), 415601.

(10) Yang, X. M.; Wan, L.; Xiao, S.; Xu, Y.; Weller, D. K. Directed Block Copolymer Assembly versus Electron Beam Lithography for Bit-Patterned Media with Areal Density of 1 Terabit/Inch2and Beyond. *ACS Nano* **2009**, *3* (7), 1844–1858.

(11) Liu, C.-C.; Ramírez-Hernández, A.; Han, E.; Craig, G. S. W.; Tada, Y.; Yoshida, H.; Kang, H.; Ji, S.; Gopalan, P.; de Pablo, J. J.; et al. Chemical Patterns for Directed Self-Assembly

of Lamellae-Forming Block Copolymers with Density Multiplication of Features. *Macromolecules* **2013**, *46* (4), 1415–1424.

(12) Delgadillo, P. A. R. Implementation of a Chemo-Epitaxy Flow for Directed Self-Assembly on 300-Mm Wafer Processing Equipment. *J. Micro/Nanolithography, MEMS, MOEMS* **2012**, *11* (3), 031302.

(13) Lin, B. J. The Ending of Optical Lithography and the Prospects of Its Successors. *Microelectron. Eng.* **2006**, *83* (4–9), 604–613.

(14) Yaegashi, H.; Oyama, K.; Yabe, K.; Yamauchi, S.; Hara, A.; Natori, S. Novel Approaches to Implement the Self-Aligned Spacer Double-Patterning Process toward 11-Nm Node and Beyond. In *Proceedings of SPIE*; Allen, R. D., Somervell, M. H., Eds.; **2011**; 79720B.

(15) Delgadillo, P. A. R. Implementation of a Chemo-Epitaxy Flow for Directed Self-Assembly on 300-Mm Wafer Processing Equipment. *J. Micro/Nanolithography, MEMS, MOEMS* **2012**, *11* (3), 031302.

(16) Ingerly, D.; Agrawal, A.; Ascazubi, R.; Blattner, A.; Buehler, M.; Chikarmane, V.; Choudhury, B.; Cinnor, F.; Ege, C.; Ganpule, C.; et al. Low-k Interconnect Stack with Metal-Insulator-Metal Capacitors for 22nm High Volume Manufacturing. In *2012 IEEE International Interconnect Technology Conference*; IEEE, **2012**; 1–3.

(17) Sanders, D. P. Advances in Patterning Materials for 193 Nm Immersion Lithography. *Chem. Rev.* **2010**, *110* (1), 321–360.

(18) Lane, A. P.; Yang, X.; Maher, M. J.; Blachut, G.; Asano, Y.; Someya, Y.; Mallavarapu, A.; Sirard, S. M.; Ellison, C. J.; Willson, C. G. Directed Self-Assembly and Pattern Transfer of Five Nanometer Block Copolymer Lamellae. *ACS Nano* **2017**, *11* (8), 7656–7665.

(19) Wan, L.; Ruiz, R.; Gao, H.; Albrecht, T. R. Self-Registered Self-Assembly of Block

Copolymers. *ACS Nano* **2017**, *11* (8), 7666–7673.

(20) Ginzburg, V. V; Weinhold, J. D.; Hustad, P. D.; Trefonas III, P. Modeling Chemoepitaxy of Block Copolymer Thin Films Using Self-Consistent Field Theory. *J. Photopolym. Sci. Technol.* **2013**, *26* (6), 817–823.

(21) Owa, S.; Wakamoto, S.; Murayama, M.; Yaegashi, H.; Oyama, K. Immersion Lithography Extension to Sub-10nm Nodes with Multiple Patterning; **2014**; *9052*, 90520O–9052–9.

(22) Natori, S.; Yamauchi, S.; Hara, A.; Yamato, M.; Oyama, K.; Yaegashi, H. Innovative Solutions on 193 Immersion-Based Self-Aligned Multiple Patterning; **2014**; *9051*, 90511E–9051–6.

(23) Doerk, G. S.; Gao, H.; Wan, L.; Lille, J.; Patel, K. C.; Chapuis, Y.-A.; Ruiz, R.; Albrecht, T. R. Transfer of Self-Aligned Spacer Patterns for Single-Digit Nanofabrication. *Nanotechnology* **2015**, *26* (8), 085304.

(24) Dallorto, S.; Staaks, D.; Schwartzberg, A.; Yang, X.; Lee, K. Y.; Rangelow, I. W.; Cabrini, S.; Olynick, D. L. Atomic Layer Deposition for Spacer Defined Double Patterning of Sub-10 Nm Titanium Dioxide Features. *Nanotechnology* **2018**, *29* (40), 405302.

(25) Wan, L.; Ruiz, R.; Gao, H.; Patel, K. C.; Albrecht, T. R.; Yin, J.; Kim, J.; Cao, Y.; Lin, G. The Limits of Lamellae-Forming PS- b -PMMA Block Copolymers for Lithography. *ACS Nano* **2015**, *9* (7), 7506–7514.

(26) Peng, Q.; Tseng, Y.-C.; Darling, S. B.; Elam, J. W. A Route to Nanoscopic Materials via Sequential Infiltration Synthesis on Block Copolymer Templates. *ACS Nano* **2011**, *5* (6), 4600–4606.

(27) Tseng, Y.-C.; Peng, Q.; Ocola, L. E.; Elam, J. W.; Darling, S. B. Enhanced Block Copolymer Lithography Using Sequential Infiltration Synthesis. *J. Phys. Chem. C* **2011**,

115 (36), 17725–17729.

(28) Segal-Peretz, T.; Ren, J.; Xiong, S.; Khaira, G.; Bowen, A.; Ocola, L. E.; Divan, R.; Doxastakis, M.; Ferrier, N. J.; De Pablo, J.; et al. Quantitative Three-Dimensional Characterization of Block Copolymer Directed Self-Assembly on Combined Chemical and Topographical Prepatterned Templates. *ACS Nano* **2017**, *11* (2), 1307–1319.

(29) Ren, J.; Zhou, C.; Chen, X.; Dolejsi, M.; Craig, G. S. W.; Rincon Delgadillo, P. A.; Segal-Peretz, T.; Nealey, P. F. Engineering the Kinetics of Directed Self-Assembly of Block Copolymers toward Fast and Defect-Free Assembly. *ACS Appl. Mater. Interfaces* **2018**, *10* (27), 23414–23423.

(30) Liu, C.-C.; Han, E.; Onses, M. S.; Thode, C. J.; Ji, S.; Gopalan, P.; Nealey, P. F. Fabrication of Lithographically Defined Chemically Patterned Polymer Brushes and Mats. *Macromolecules* **2011**, *44* (7), 1876–1885.

(31) Xiong, S.; Wan, L.; Ishida, Y.; Chapuis, Y.-A.; Craig, G. S. W.; Ruiz, R.; Nealey, P. F. Directed Self-Assembly of Triblock Copolymer on Chemical Patterns for Sub-10-Nm Nanofabrication via Solvent Annealing. *ACS Nano* **2016**, *10* (8), 7855–7865.

(32) Pathangi, H.; Chan, B. T.; Bayana, H.; Vandenbroeck, N.; Heuvel, D. Van Den; Look, L. Van; Rincon-Delgadillo, P.; Cao, Y.; Kim, J.; Lin, G.; et al. Defect Mitigation and Root Cause Studies in 14 Nm Half-Pitch Chemo-Epitaxy Directed Self-Assembly LiNe Flow. *J. Micro/Nanolithography, MEMS, MOEMS* **2015**, *14* (3), 031204.

(33) Hur, S.-M.; Khaira, G. S.; Ramírez-Hernández, A.; Müller, M.; Nealey, P. F.; de Pablo, J. J. Simulation of Defect Reduction in Block Copolymer Thin Films by Solvent Annealing. *ACS Macro Lett.* **2015**, *4* (1), 11–15.

(34) Hur, S.-M.; Thapar, V.; Ramírez-Hernández, A.; Nealey, P. F.; de Pablo, J. J. Defect

Annihilation Pathways in Directed Assembly of Lamellar Block Copolymer Thin Films. *ACS Nano* **2018**, *12* (10), 9974–9981.

(35) Cai, C.; Padhi, D.; Seamons, M.; Bencher, C.; Ngai, C.; Kim, B. H. Defect Gallery and Bump Defect Reduction in the Self-Aligned Double Patterning Module. *IEEE Trans. Semicond. Manuf.* **2011**, *24* (2), 145–150.

(36) Schabes, M. E. Micromagnetic Simulations for Terabit/In2 Head/Media Systems. *J. Magn. Magn. Mater.* **2008**, *320* (22), 2880–2884.

(37) Hellwig, O.; Bosworth, J. K.; Dobisz, E.; Kercher, D.; Hauet, T.; Zeltzer, G.; Risner-Jamtgaard, J. D.; Yaney, D.; Ruiz, R. Bit Patterned Media Based on Block Copolymer Directed Assembly with Narrow Magnetic Switching Field Distribution. *Appl. Phys. Lett.* **2010**, *96* (5), 052511.

(38) Williamson, L. D.; Seidel, R. N.; Chen, X.; Suh, H. S.; Rincon Delgadillo, P.; Gronheid, R.; Nealey, P. F. Three-Tone Chemical Patterns for Block Copolymer Directed Self-Assembly. *ACS Appl. Mater. Interfaces* **2016**, *8* (4), 2704–2712.

CHAPTER 5: THERMAL CONDUCTIVITY REDUCTION IN AMORPHOUS SILICON NITRIDE PHONONIC CRYSTAL FABRICATED USING DIRECTED SELF-ASSEMBLY OF BLOCK COPOLYMERS

5.1 Abstract

The reduction of thermal conductivity in nanostructured crystalline semiconductor materials have been extensively studied. The similar phenomenon in amorphous materials is much less explored, but the thermal management of amorphous solids is equally crucial in various semiconductor electronic devices. Here we present the design and fabrication process of suspending phononic crystal structures made of amorphous silicon nitride. Directed self-assembly of cylinder-forming block copolymer is integrated to pattern highly ordered hexagonal packed holes with 12 nm neck width and 37.5 nm pitch in silicon nitride. The reduction of thermal conductivity at room temperature is 60% smaller than the value predicted based on porosity. In comparison, holes with larger neck width and pitch patterned by e-beam lithography lead to slightly reduced thermal conductivity that is close to classical prediction. We show that the thermal conductivity of amorphous material could also be engineered by phononic crystal nanostructures where the smallest dimension of the structure plays the most import roles. The small and uniform periodic nanostructures obtained by block copolymer patterning could suppress the transport of propagating phonons with broad range of mean-free paths. In addition, by changing the orientation of block copolymer patterned hexagonal holes relative to the heat flow direction, we find that the propagating phonons travel in random directions in amorphous silicon nitride. This is different with the directional phonon transport observed in phononic crystals made of single crystal silicon.

5.2 Introduction

Manipulating thermal properties using nanostructures has attracted great attention recently as it holds promises to enhance the heat to electricity conversion efficiency in thermoelectric devices.[1–3] For non-metals, including semiconductor and insulator materials, the heat is transported dominantly through atomic lattice vibrations known as phonons. Recent experimental and theoretical work has greatly advanced understandings of phonon transport in nanostructured solids.[4] Extensive studies use nanostructures to block phonons with mean free path (MFP) longer than characteristic sizes and thus reduce thermal conductivities.[5–7] If nanostructures don't alter the electric conductivity as significantly, the energy conversion efficiencies in thermoelectric devices could be enhanced.[8,9] Such phenomena have been reported in various nanostructures including nanowires[10–12], porous thin films[5,8], nanocomposites[13] and superlattices[14].

Phononic crystals, which are usually two-dimensional periodic nanopores or nanomesh fabricated by top-down process with high precision, have been used as good test beds to study the nanoscale thermal transport.[4] The dependence of thermal conductivities on the characteristic size in phononic crystal patterning has been reported.[7,15,16] It is important to note that, phonon wave interference or coherent phonon scattering in phononic crystals only happens when phonon wavelength matches the periodicity of holes and is much longer than surface roughness at boundaries.[17–19] At room temperature, most studies state that the incoherent phonon scattering is the dominating factor to explain the reduced thermal conductivities, as the heat-carrying phonons have wavelength much shorter than the periodicity of phononic crystals.[7,17,20,21] The observed lower thermal conductivity when the characteristic size is smaller has been mainly attributed to the transport of more long MFP phonons being surpressed.[4,5,8,21–23]

Based on such incoherent phonon scattering mechanism, one can achieve lower thermal conductivity and potentially better device performance by further reducing the size of nanopores in phononic crystal patterning, which however limited by certain technical barriers such as the patterning resolution in conventional lithographic techniques. Block copolymers (BCPs) that could self-assemble into various well-ordered nanoscale features as small as few nanometers have been used for high-resolution patterning in different applications with easy implementation and low cost.[24] Using asymmetric diblock copolymers which form perpendicular cylinder nanostructures in thin films, high-resolution holes can be used as pattern transfer masks after selectively removing cylindrical nanodomains.[25,26] Lim et al. used cylinder forming poly(styrene-*b*-2-vinylpyridine) (PS-*b*-P2VP) to pattern single crystal Si thin films with holes at a fixed pitch size of 60 nm and neck size as small as 16 nm, and observed significantly reduced thermal conductivity.[27] However, the existing studies of utilizing BCP patterned nanostructures to impede thermal phonon transport merely used self-assembled patterns with short-range order in lateral arrangement.[5,6,27] The directionality of phonon could be interrupted due to the random orientation in different grains or by defects at grain boundaries in self-assembled pattern.

The nanoscale heat transfer in crystalline materials, such as single crystal Si, has been extensively studied. In comparison, the understanding of thermal transport mechanisms in amorphous materials is much less developed.[28] The heat propagation in disordered solids is much more complicated considering the lack of symmetry in lattice structure.[28] Based on earlier models, in amorphous solids, heat is conducted through overlapping thermal energy between neighbouring atoms vibrating independently.[29–31] Phonons in fully disordered atomic lattice should have extremely short MFP at the scale of atomic spacing. How could phononic crystal patterning with nanoscale features affect the transport of such short MFP phonons in amorphous solids? From the

application perspective, amorphous materials are widely used for a variety of electronic devices. Controlling their thermal properties at nanoscale is crucial to optimize the thermal design of devices.[28,32,33] For example, silicon nitride (SiN_x) is commonly used for suspended structures in many MEMS devices.[34] Therefore, it not only is of fundamental interest but also could impact device performance in applications to study if the same impeded phonon transport due to phononic crystal patterning would occur in amorphous materials.

In this study, we demonstrated the how phononic crystals, especially those with very small characteristic size patterned by block copolymer lithography, work for amorphous SiN_x film. We described the design and fabrication process of micromachined suspending SiN_x bridges to reliably measure in-plane thermal conductivity through thermoreflectance. To eliminate defects in self-assembled BCP layer and preserve the potential directionality of propagating phonons, we employed chemical patterns to direct the self-assembly (DSA) of block copolymer cylinders. Hexagonal packed holes patterned by DSA cylinders with very small periodicity and neck width (p = 37.5 nm, n =12 nm) and perfect long-range two-dimensional order were successfully created in amorphous silicon nitride. In comparison, reference sample patterned by e-beam lithography with p = 800 nm and n =321 nm caused relatively small reduction in thermal conductivity. We show clear evidence that phononic crystals with small characteristic size could suppress phonon propagation even in amorphous materials. We further investigated the directionality of phonon in amorphous silicon nitride. By rotating the DSA pattern, the phononic crystal patterns rotated with different angles relative to the overall heat flow directional, which resulted different extent of blockage of phonon pathways. The thermal conductivity of these samples was reduced similarly, indicating the weak directionality of phonons in amorphous SiN_x.

5.3 Experimental Section

5.3.1 Materials

Silicon wafers (4″, N-type, ⟨100⟩ orientation) coated with 70 nm thick low-stress silicon nitride film were purchased from WRS materials. AR-P 6200.04 (CSAR 62) e-beam resist was purchased from ALLRESIST. AZ MiR 703 photoresist and AZ 1:1 developer were purchased from EMD Performance Materials and used as received. Spin-on-carbon (SOC) and spin-on-glass (SOG) solutions were provided by Tokyo Ohka Kogyo Co. (TOK) and used as received. Cylinder-forming poly(styrene-block-methyl methacrylate) (PS-*b*-PMMA, C2050, M_n = 20.2-50.5 kg/mol, PDI = 1.07, L0 ~38nm) and hydroxyl terminated polystyrene (PS-OH, M_n = 6 kg/mol, PDI = 1.05) were purchased from Polymer Source, Inc. Poly(styrene-co-methyl methacrylate-co-glycidyl methacrylate) (PS-*r*-PMMA-r-PGMA) containing 4 mol % of glycidyl methacrylate and 63 mole % of styrene was synthesized by reversible addition fragmentation chain transfer (RAFT) polymerization (denoted as 63S).

5.3.2 Sample preparation

Patterning silicon nitride using directed self-assembly of block copolymer

The substrate was spin coated with ~100 nm of SOC and then ~30 nm of SOG. The wafer was baked at 205 °C for 1 min after each film. Then an 8 nm 63S mat film was prepared by spin-coating 0.3 wt% of 63S in toluene solution at 2000 rpm and crosslinking at 230 °C for 20 min in N_2 atmosphere. 80 nm AR-P 6200.04 e-beam resist was coated and baked at 150 °C for 1 min. Hexagonal packed dots pattern with pitch around 75 nm was written by a Raith EBPG5000 Plus e-beam writer using 100 kV accelerating voltage and 1 nA beam current. The e-beam pattern was developed in *n*-amyl acetate for 1 min and then etched into 63S mat with O_2 reactive ion etch (RIE) in a PlasmaTherm RIE instrument for 15 s. The e-beam resist was then stripped in 1-Methyl-2-

pyrrolidinone (NMP). PS-OH was spin-coated from 1wt% toluene solution at 1500 rpm and the wafer was baked at 230 °C for 30 min to graft the PS-OH brush to the exposed SOG film in the e-beam patterned area. Unreacted brush was rinsed off using NMP and toluene. Subsequently, the block copolymer (C2050) was spin-coated on the substrate from 2 wt% toluene solution at 1500 rpm, yielding an ~80 nm film and thermally annealed at 270 °C for 2 h. The BCP film was converted into porous AlO_x nanostructures using sequential infiltration synthesis (SIS) followed by O_2 RIE as published in the previous study of the same BCP[35]. Using RIE with CF_4 gas, the BCP templated AlO_x holes were etched into SOG. The wafer was immersed in diluted KOH solution to remove AlO_x. Photolithography was performed using a Heidelberg MLA150 Direct Write Lithographer, AZ MiR 703 photoresist and AZ 1: 1 developer to expose 28 μm by 28 μm squares designed for the phononic crystal areas. Some devices didn't have photolithography pattern in this step as reference samples without phononic crystal patterning. The wafer was then etched in RIE using O_2 gas to transfer the holes from the exposed SOG to SOC. The photoresist was stripped in NMP. Later a mixture of CHF_3 and O_2 gas was used to etch the holes into SiN_x film while the SOG film was removed together. The wafer was then cleaned in oxygen plasma for 1 min, which removed all SOC film.

Patterning silicon nitride using e-beam lithography

The same SOG/SOC films were prepared on the silicon nitride coated wafer to make e-beam patterned phononic crystals. 80 nm AR-P 6200.04 e-beam resist was coated and baked at 150 °C for 1 min. Hexagonal packed dots patterns with 800 nm pitch were written in 50 μm by 50 μm square areas by the Raith EBPG5000 Plus e-beam writer using 100 kV accelerating voltage and 3 nA beam current. The e-beam patterned area was developed in n-amyl acetate for 1 min and then

etched into SOG with CF_4 based RIE. Afterwards, the holes were transferred down to silicon nitride following the same photolithography, dry etch and wafer cleaning procedure.

Fabricating suspending silicon nitride phononic crystals

The phononic crystal devices were fabricated using a microfabrication process shown in Figure 5-1. After silicon nitride is patterned with holes using block copolymer or e-beam lithography, AZ MiR 703 photoresist was coated on the wafer and patterned in Heidelberg MLA150 Direct Write Lithographer. 100 nm Al was deposited on the resist using Angstrom EvoVac Electron Beam Evaporator and lifted off in NMP at 80°C, which formed three aluminum pads for each phononic crystal device. Another photolithography step was performed to pattern two triangular areas and the exposed silicon nitride was removed by RIE etching with CHF_3 and O_2 gas. Photoresist was stripped in NMP. Finally, the porous silicon nitride bridges were released by anisotropic Si wet etch. We used a buffered tetramethylammonium hydroxide (TMAH) formulation to prevent dissolution of aluminium.[36] The etchant was made of 200 mL 10% TMAH aqueous solution with 7 g Si powder dissolved at 40 °C. After adding 3 g ammonium persulfate and heating the solution to 85 °C, the device wafer was immersed in the bath for 30 min. The wafer was then cleaned by immersing in a boiling DI water bath, and a cold DI water bath, and rinsing thoroughly by DI water and isopropanol.

5.3.3 Thermoreflectance measurement

The thermal conductivity of amorphous silicon nitride phononic crystals was measured by time domain thermoreflectance (TDTR) method, which is an optical pump-probe transient response measurement.[37] The sample was placed in vacuum at a pressure of 5×10^{-4} Pa to exclude the influence of convection on thermal relaxation behavior. The center Al pad deposited on phononic crystal with was irradiated with both a continuous wave pump laser at a wavelength of 785 nm

and, a quasi-continuous wave pump laser with a pulse duration of 4 μs at a wavelength of 852 nm. The pump beam raises the temperature of the Al pad, then the reflectivity of the pad increases. By measuring intensity of the reflected probe beam, we can observe the temperature transient response of the Al pad, which includes the information of thermal conductivity. The measured thermoreflectance signals are analyzed by finite element method to obtain the thermal conductivity values of the sample. The standard error of our measurement is smaller than ±3% for each sample.

5.4 Results and Discussion

5.4.1 Design and fabrication process flow of silicon nitride phononic crystals

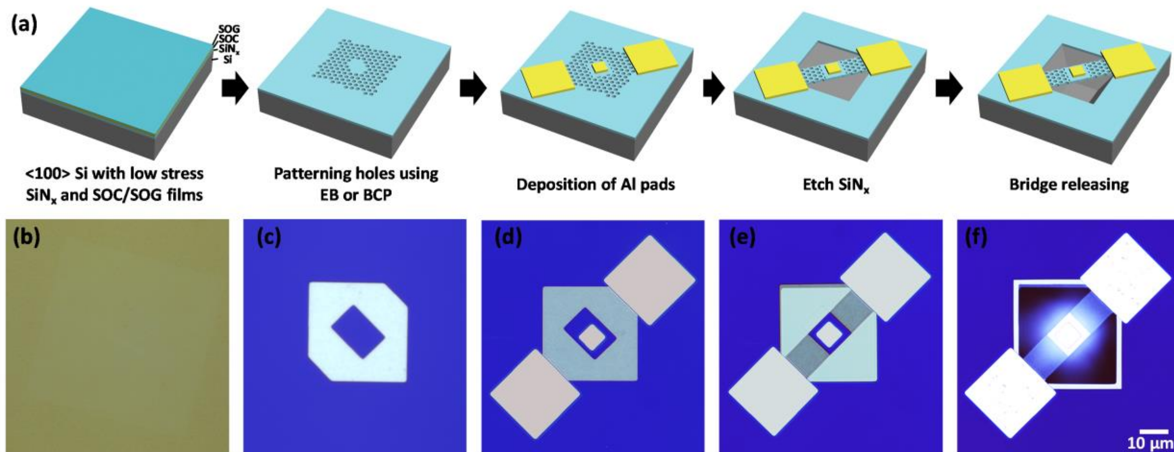

Figure 5-1: (a) Schematic illustration of fabricating silicon nitride phononic crystals for thermoreflectance measurement. The corresponding optical microscopy images showing the fabrication process of the DSA patterned phononic crystal device: (b) pattern transfer of the BCP templated holes into SOG film; (c) photolithography and only holes in the exposed area were transferred from SOG/SOC to silicon nitride (light blue color); (d) photolithography and metal lift-off to deposit the aluminum pads (white color); (e) silicon nitride was removed in the two triangular area; (f) the bridge of silicon nitride phononic crystal was released by Si wet etch.

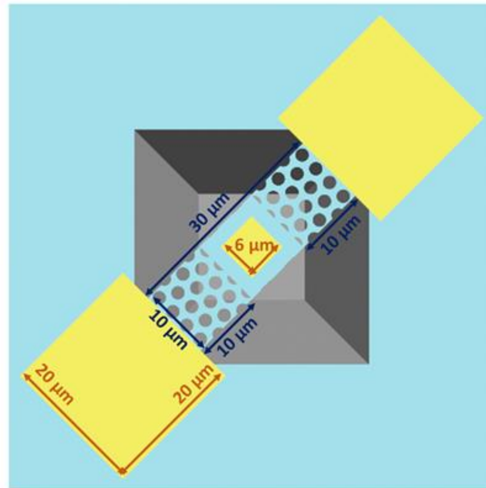

Figure 5-2: Design of the silicon nitride phononic crystals for thermoreflectance measurement with dimensions labeled.

Figure 5-1(a) schematically illustrates the fabrication process of silicon nitride phononic crystals, which is based on conventional microfabrication techniques using <100> Si wafer with patterned LPCVD SiN_x mask. (See experimental section for details.) First, the SiN_x film was patterned with hexagonal array of holes using either BCP lithography or e-beam lithography in the square shape area designed to be phononic crystals. Three Al pads (colored in yellow in Figure 5-1(a)) were deposited on each device area: a smaller one at the central and two larger ones at two opposite corners. Then the extra silicon nitride was removed leaving the phononic crystal patterned SiN_x in a rectangular bridge shape area with two long edges 45° relative to the Si <110> direction and two short edges covered by aluminum pads. To suspend the fabricated silicon nitride nanostructures, the device wafer was immersed in silicon wet etchant to selectively remove the exposed <100> Si. The dimensions of silicon nitride phononic crystals are labeled in Figure 5-2. As an example of the device fabrication, Figure 5-1(b-f) displays the corresponding optical images

when making phononic crystals patterned by BCP lithography. More details about BCP lithography will be explained in section 5.4.2.

The thermal properties of fabricated silicon nitride phononic crystals are measured using the time domain thermoreflectance (TDTR) technique which is a well-researched non-contact optical measurement technique for studying thermal properties of nanostructures[15,22,38]. The heat introduced by the pulsed pump beam irradiating the center Al pad would dissipate through the suspended structure of interest and escape to the bulk substrate at two ends.

The thermoreflectance measurement has been used to provide insights of phononic crystal effects in single crystal Si based nanostructures, where the samples were commonly prepared on silicon-on-insulator (SOI) wafers followed with etching the buried oxide in HF.[15,22,38] The etching of buried oxide is isotropic and leaves large undercutting surrounding the area of interest. The resulting large extra suspending film also contributes to the measured thermal conductance and thus increases the measurement error. In comparison, the wet etching of Si is highly anisotropic and self-limiting: the etch rate of <111> Si is negligible. To etch the Si underneath the silicon nitride, the bridge must rotate relative to the Si <110> direction as 45° in this study. Therefore, the released SiN_x bridges were hanging diagonally on top of a square shape concave made of <111> Si sidewalls at 54.7° relative to the wafer surface. The length of the SiN_x bridges is highly reproducible with minimized device-to-device variations. The two additional Al pads have edges covering the ends of SiN_x bridges and perpendicular to the direction of global heat flow. As the thermal conductivity of Al (about 120 W/mK for 100 nm Al[39]) is much higher than that of SiN_x (2.5 W/mK as in section 3.3), its contribution to measured thermal conductivity is negligible. The local heat flow will quickly escape to the heat sink once in contact with Al, which ensures phonons travel similar distance from the center Al pad to the bulk heat sink.

5.4.2 Patterning silicon nitride by directed self-assembly of BCP

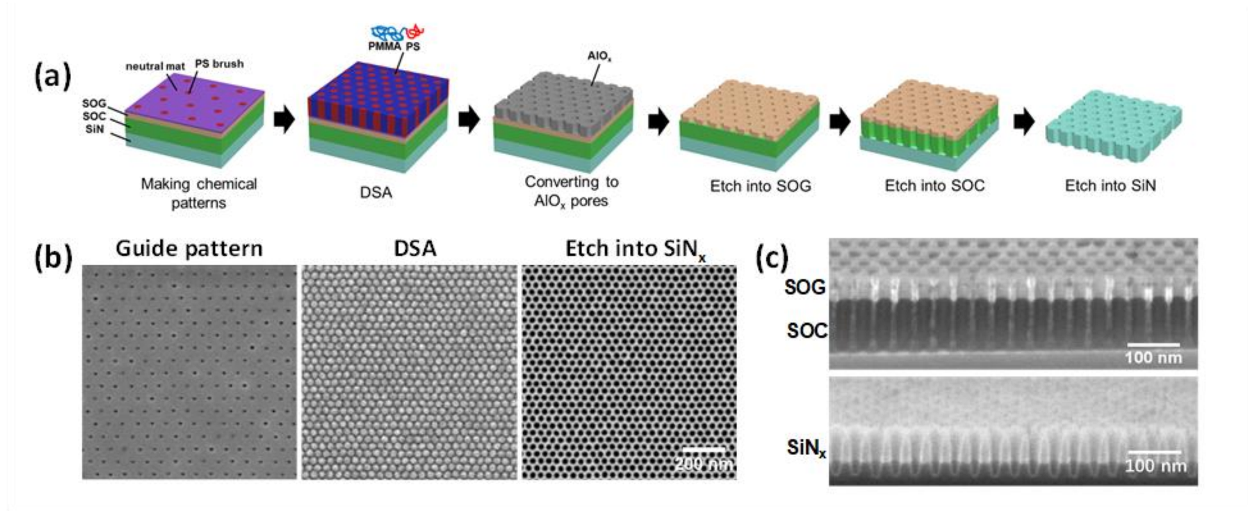

Figure 5-3: (a) Schematic illustration of DSA of PS-cylinder forming BCP on ebeam defined chemical pattern with $L_s = 2L_0$ and patterning silicon nitride with holes templated by the DSA pattern of PS cylinder forming BCP. (b) Top-down SEM images of ebeam resist pattern ($L_s = 75$ nm), DSA pattern of PS cylinder forming BCP ($L_0 = 37.5$ nm), and holes etched into silicon nitride with pitch 37.5 nm. (c) Cross-sectional SEM images of the BCP templated holes etched into SOG/SOC and silicon nitride respectively (imaged samples were tilted to 70 °).

To implement the DSA process on the SiN_x phononic crystals, it is necessary to ensure that well-ordered holes are successfully transferred from BCP film to SiN_x. We used a PS-cylinder-forming PS-*b*-PMMA (C2050) with self-assembly conditions studied in an earlier paper[35]. This BCP was used here because it could be easily transformed to array of AlO_x holes with highly uniform and tuanable hole size through a vapor phase reaction, SIS[35]. AlO_x has good dry etch resistivity, so it is a good etch mask to transfer the nanopores to hardmasks. The pore size of AlO_x is not limitied to the volume fraction of minority block in BCP but determined by the amount of AlO_x infiltrated into the BCP film during SIS, which allows furthur reduction of the neck width in future studies. The DSA of the PS-cylinder-forming BCP has not been reported. Chemical patterns or topographical patterns are often used to guide the formation of defect-free hexagonal arrays of BCP cylinders over the large area.[40–43] The prepatterned spots could have period L_s multiple

integral larger than BCP L_0 to reduce the patterning time.[41–44] Considering the process integration and pattern transfer uniformity, we employed chemical patterns on flat surface to DSA the PS cylinders in this study.

Figure 5-3 (a) shows the scheme of the chemoepitaxial DSA flow of PS-cylinder forming BCP, transformation of BCP cylinders to opened holes, and the pattern transfer process. A stack of spin-on-carbon (SOC) and spin-on-glass (SOG) layers were put on top of the SiN_x film and used for pattern transfer purpose after generating the BCP hexagonal packed cylinders. To prepare the chemical patterns, a thin film of neutral mat was used. The same mat, a crosslinkable PS-*r*-PMMA material (63 % PS), was reported to achieve the perpendicular cylinder orientation[35]. The neutral mat was e-beam patterned with hexagonal array spots patterns with period $L_s = 2L_0$. Hydroxyl terminated PS-OH homopolymer brush was grafted on the exposed SOG surface in the e-beam patterned dots. Thus, the formed chemical pattern has PS-wetting spots and non-preferential background. BCP (C2050) was thermally annealed on this chemical pattern to form hexagonal arrays of perpendicular PS cylinders in PMMA matrix. The density of DSA cylinders (period L_0) is 4 times higher than that of e-beam prepatterns (period L_s). The PMMA matrix was selectively converted to porous AlO_x. Subsequently, the holes formed were etched into SOG, and later from SOG to SOC with excellent dry etch selectivity. Then the holes were transferred into SiN_x using dry etch, which removed the SOG layer at the same time. The SOC was later removed by short oxygen plasma cleaning. Figure 5-3(b) shows the SEM images of e-beam resist patterning (L_s = 75 nm), DSA of C2050 in registration with underlying chemical pattern (L_0 = 37.5 nm) and holes etched into SiN_x (p = 37.5 nm). Figure 5-3(c) shows the etching profiles of holes in SOG/SOC and SiN_x.

During the device fabrication, the photoresist developer is a base solution which could dissolve AlO_x, so it is necessary to transfer the holes from AlO_x to SOG in the first step as shown in Figure 5-1(b) and 5-3(a). The color of square shape DSA patterned area is slightly different in optical microscopy due to the highly ordered nanostructures. Using conventional photolithography (Figure 5-1(c)), the holes were etched into the SiN_x only in the target device area. Then, following the schematic described in section 5.4.1, the DSA patterned SiN_x were made into suspending bridges designed for TDTR measurement.

The defect-free DSA was achieved after optimizing the e-beam patterned spots as well as the commensurability of L_s with $2L_0$. Figure 5-4(a) shows the DSA results on chemical patterns prepared with a range of e-beam exposure doses. L_s of all resist patterns was fixed at 75 nm. For the resist pattern with lowest dose, it had smallest spot sizes but very poor uniformity. The corresponding DSA pattern lacked long-range order because the registration of PS cylinders on PS-OH brush modified spot is too weak. When the resist patterned with higher e-beam doses, the spot sizes increased, the uniformity improved, and the registration of PS cylinders was achieved. At even higher dose, the assembly was still guided by the underlying chemical pattern, but number of defects greatly increased. Not only were there dark spots in hexagonal packed cylinders, but also different BCP morphologies other than perpendicular cylinders appeared. When the PS-OH brush modified spot is too big, the overall interfacial energy of underlying chemical pattern shifted out of the neutral window, so the perpendicular cylinder orientation could not sustain over large area. The moderate e-beam exposure dose (in red circle) is thus optimal for DSA.

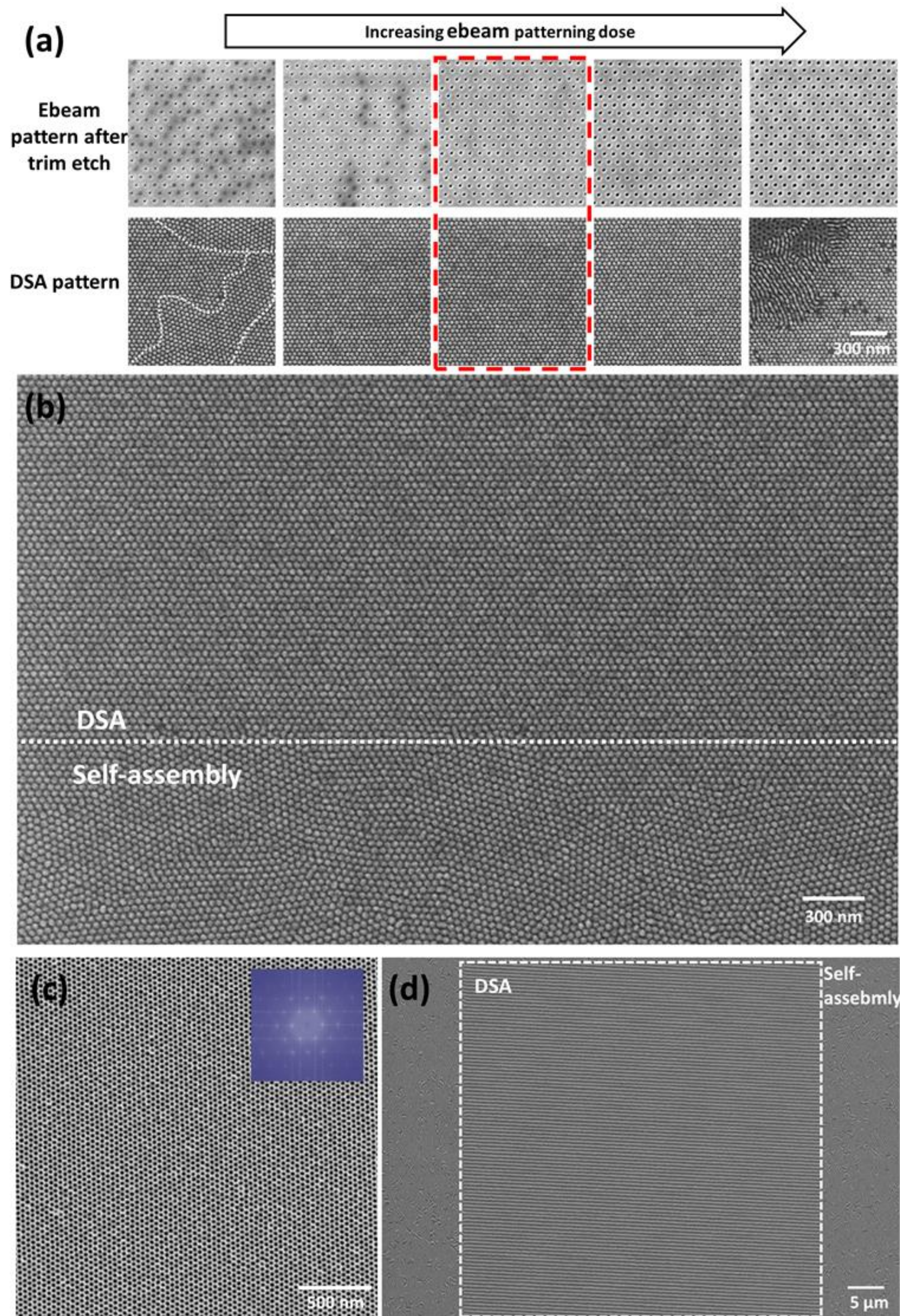

Figure 5-4: (a) SEM images of the resist patterns (L_s = 75 nm) with different exposed hole sizes and the corresponding DSA results. The ebeam condition circled in red was used to make phononic crystal device. (b) A SEM image of the DSA result taken at the edge of the patterned area. (c) A SEM image of the DSA holes in silicon nitride over a larger area and the 2D FFT image (insect). (d) The low-magnification SEM image with Moiré interference patterns of a 50 µm × 50 µm DSA patterned area (indicated by the white dash lines) with long range ordering. Outside of the DSA patterned area, the Moiré interference patterns have multiple orientations, indicating there is no long-range ordering.

As shown in Figure 5-4(b), perfectly long-range ordered and registered PS cylinders were formed on chemically patterned area. On non-patterned area, self-assembled perpendicular PS cylinders formed in small randomly oriented grains. SEM images of large area of DSA holes pattern transferred into silicon nitride are shown in Figure 5-4(c). The inserted 2D fast Fourier transform (FFT) has a symmetric hexagonal pattern with sharp peaks, indicating highly ordered hexagonal pattern of SiN_x. In Figure 5-4(d), the Moiré interference patterns represent an area as large as 50 µm × 50 µm of DSA pattern with high degree of perfection.

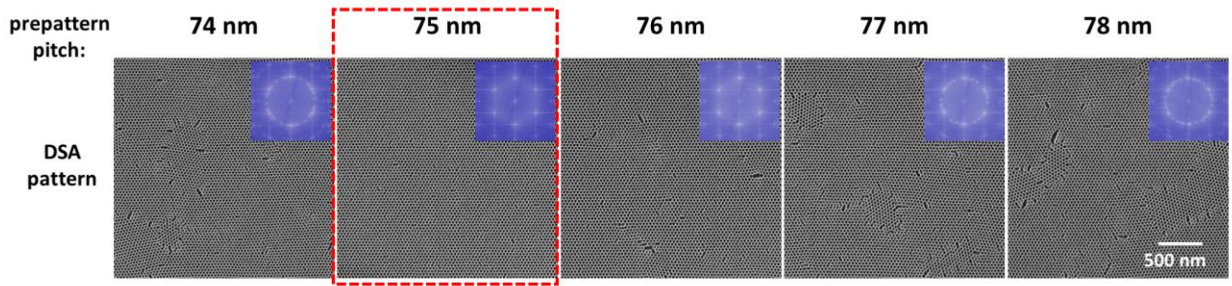

Figure 5-5: SEM images of DSA patterns etched into silicon nitride with different L_s and the 2D FFT images (inset). The DSA on resist pattern at L_s = 75 nm (in red circle) was used to make the phononic crystal device.

According to previous DSA studies, the DSA of BCP cylinders on chemical patterns is sensitive to the commensurability of L_s with L_0.[40,43,45] Yang et al. found well-ordered DSA cylinders of a PMMA-cylinder-forming BCP with L_0 = 28 nm were formed on patterns with L_s = 56-60 nm, and that the cylinders lost long-range order at L_s = 54 nm and 62 nm.[43] A similar tendency was observed for C2050 as shown in Figure 5-5. At L_s = 75 nm, the DSA pattern had fewest defects in SEM image. When L_s was smaller or larger than 75 nm, the DSA pattern had more merged cylinders (L_s = 76 nm) or small grains of misorientations (L_s = 74 nm, 77 nm and 78 nm). The ordering of the DSA patterns were revealed in FFT spectrums as well. The DSA patterns with fewer defects showed sharper hexagonal peaks, while the circles in FFT spectrum indicates existence of

misoriented grains. DSA pattern at L_s = 75 nm (in red circle) was therefore chosen to fabricate the phononic crystal devices.

5.4.3 Impact of limiting dimension

To study the impact of DSA patterning on thermal properties, we measured TDTR to compare different SiN_x phononic crystals. As shown in Figure 5-6, three types of samples were measured: SiN_x (a) with DSA patterned holes (p = 37.5 nm), (b) with e-beam patterned holes (p = 800 nm), and (c) without holes patterned, they were fabricated through very similar procedures (see experimental section for more details).

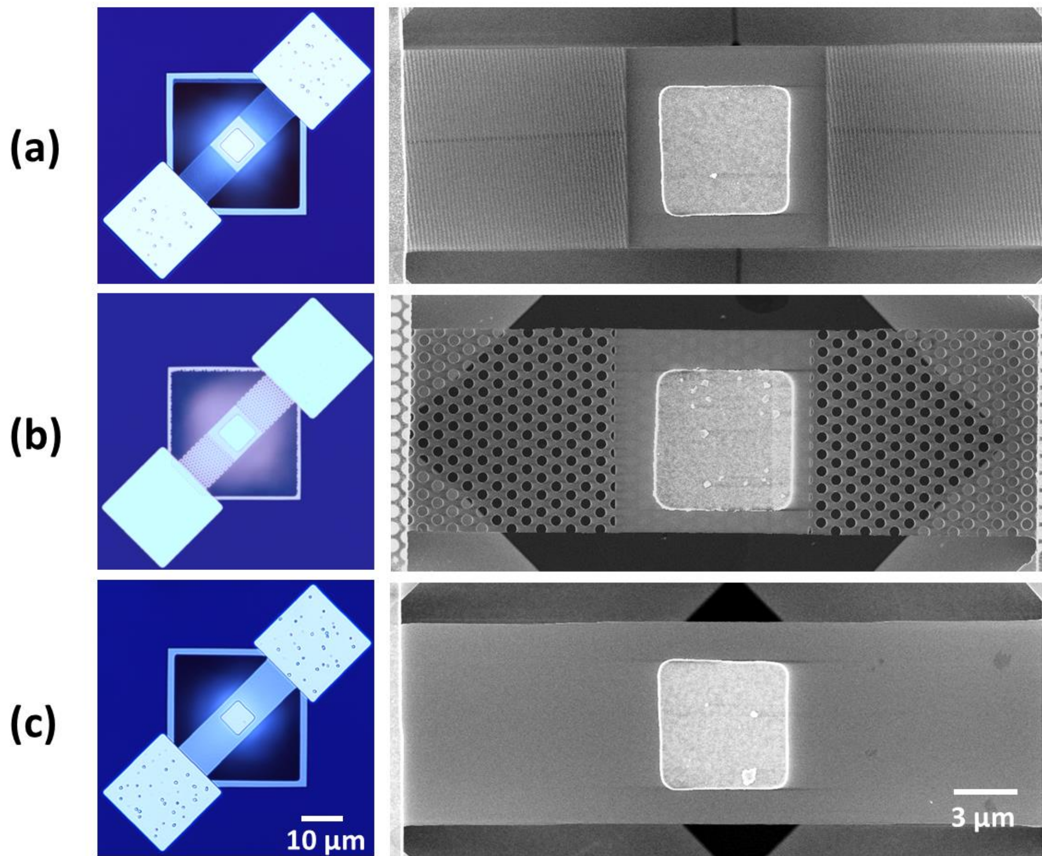

Figure 5-6: Optical microscopy and SEM images and of the suspending silicon nitride bridges (a) with DSA patterned holes (p = 37.5 nm), (b) ebeam patterned holes (p = 800 nm), and (c) without holes patterned

High magnification SEM images taken along the edge of the bridges patterned by DSA and e-beam lithography are displayed in Figure 5-7. Both of they showed very narrow hole diameter distribution. The DSA holes in silicon nitride bridge has an average hole diameter of 25.3 ±1.1 nm, neck size of 12.0 ±1.1 nm and the overall porosity of 41.9%. The e-beam patterned holes have an average hole diameter of 476.9 ±1.4 nm, neck size of 323.1 ±1.4 nm and the overall porosity of 32.2%.

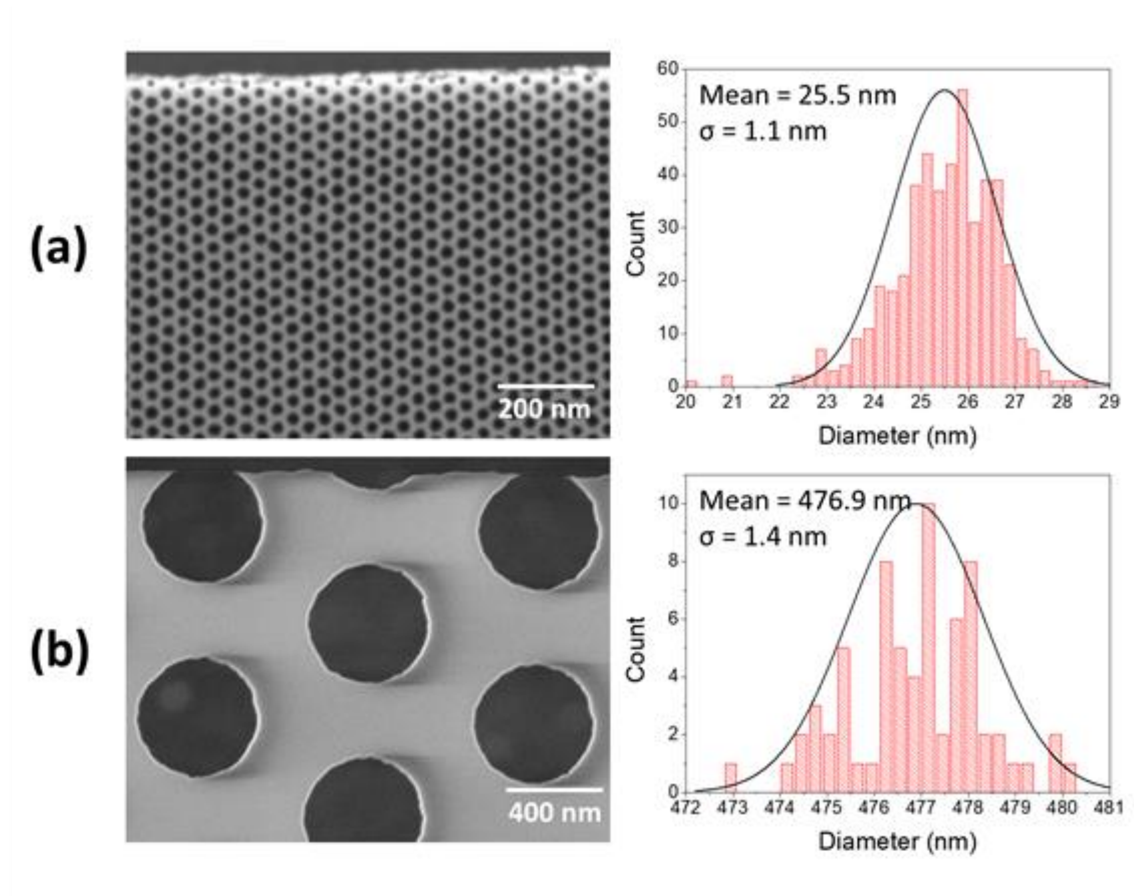

Figure 5-7: High magnification SEM images taken along the edge of the bridges and statistical analysis of hole sizes (fitted the normal distribution) of (a) DSA and (b) ebeam patterned holes.

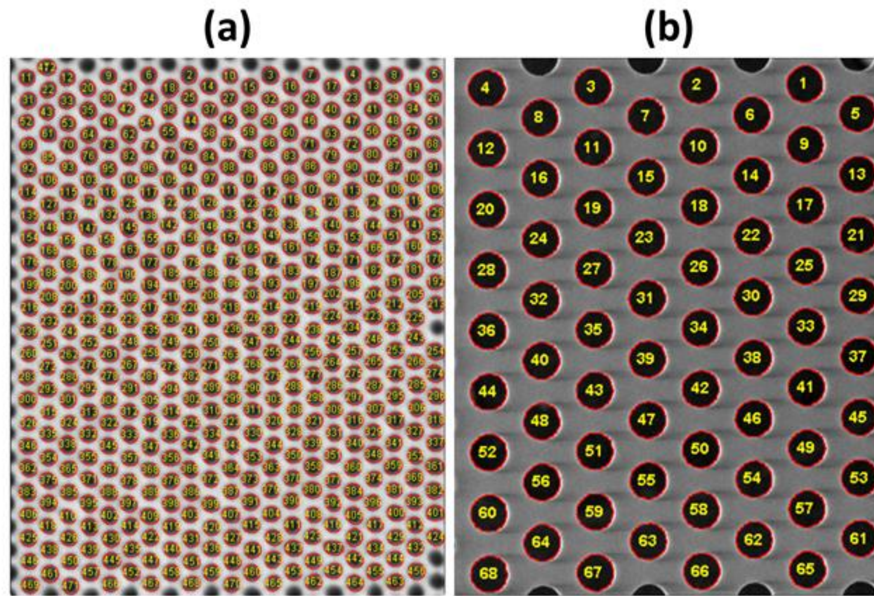

Figure 5-8: The outlines of (a) DSA and (b) ebeam patterned holes extracted from SEM image.

Figure 5-9(a) shows the schematic illustration of the cross-section of the device and the TDTR measurement: a pulse laser beam periodically heats the Al in the center of SiN_x bridge while the continuous laser measures the change in reflectance caused by the temperature rise. Figure 5-9(b) presents the themoreflectance signals collected from three different samples. The time dependence of the reflectance was well fitted by exponential decay, exp $(-t/\tau)$, where τ is the thermal decay time. The dimensions of holes and the measurement results for every samples are summarized in Table 5-1.

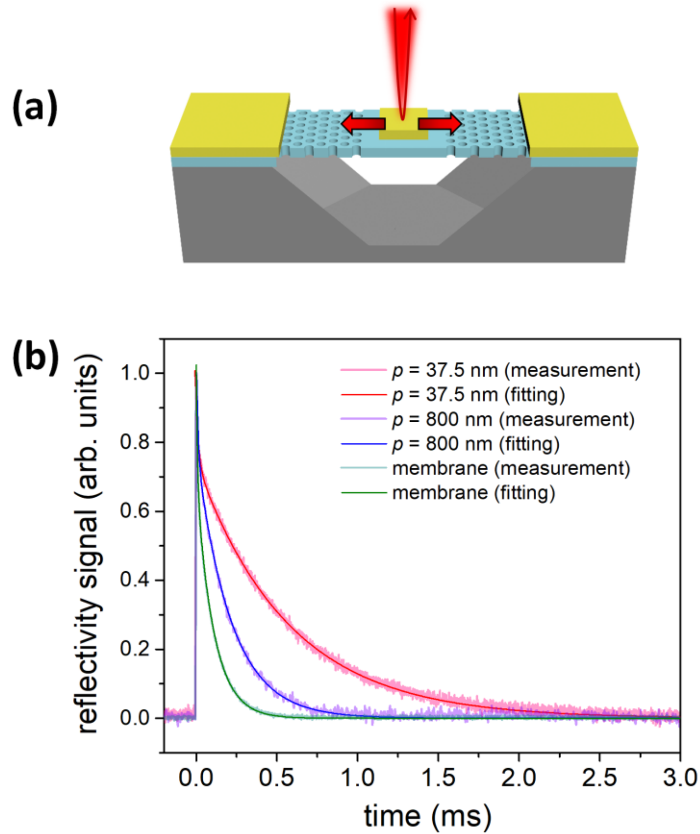

Figure 5-9: (a) Schematic illustration of cross-section of the device and the thermoreflectance measurement. Laser beams are focused on the aluminum pad placed at the center of silicon nitride bridge. (b) Representative recorded reflectance signals of silicon with DSA patterned holes (red curve), ebeam patterned holes (blue curve), and unpatterned silicon nitride membrane (green curve).

Table 5-1: Summary of measurement results

	p (nm)	d (nm)	n (nm)	Porosity	τ (μs)	$\kappa_{predicted}$ (W/mK)	$\kappa_{measured}$ (W/mK)
DSA holes	37.5	25.5	12.0	41.9%	570±30	1.0	0.39±0.02
e-beam holes	800	476.9	323.1	32.2%	210±4	1.3	1.2±0.02
membrane	0	0	0	0	120±5	2.5±0.1	2.5±0.1

The DSA patterned phononic crystal showed longest decay time and thus has highest thermal resistance. The thermal conductivities calculated for DSA patterned, e-beam patterned, and unpatterned SiN_x are 0.4, 1.2, and 2.5 W/mK, which are averaged value of 4 devices. The measured

value of unpatterned SiN_x thin film is in good agreement with the reported value for LPCVD deposited SiN_x[46]. This proves the reliability of the TDTR measurement and fitting. In this study, all samples were measured at room temperature only.

There is 84% and 52% reduction in thermal conductively when SiN_x was patterned by DSA with p =37.5 nm and e-beam with p = 800 nm respectively. The thermal conductivity reduction caused by phononic crystal patterning could be attributed to two mechanisms: the volume reduction and blocking of propagating phonons. Thus, it is illustrative to first compare against predicted thermal conductivity taking account of the effect of volume reduction which is related to their porosity, ϕ. The predicted thermal conductivities, $\kappa_{\text{predicted}}$, were calculated for SiN_x with different porosities by finite element method (FEM) simulation using ANSYS software. The $\kappa_{measured}$ is 61% smaller than $\kappa_{predicted}$ for DSA patterned phononic crystals, and 8% for e-beam patterned ones. Therefore, the volume reduction factor alone underestimates the reduction of thermal conductivities of amorphous SiN_x, especially when it was patterned with smaller DSA holes.

The effect of nanostructures on amorphous SiN_x thermal properties shows remarkable similarities with existing studies of crystalline materials: nanostructures with smaller p and n leads to smaller thermal conductivities than unpatterned SiN_x film even after taking account of the volume reduction. Because amorphous materials lack the translational symmetry and periodicity in atomic lattice, cautions should be taken when applying concepts of phonon transport to amorphous materials.[28] More recent models, and later proved by molecular dynamics simulations as well as experimental measurement state that in amorphous solids, although the majority of heat are carried by diffusive lattice vibrations with high frequency, which is called diffusons, there exists propagating phonon like vibration having relatively long MFP, which is called propagons.[47–51] Propagons are capable of transporting phonons much more efficiently than diffusons due to their

long MFP. Therefore, small population of propagons could contribute to great portion of overall thermal conductivity in amorphous solids.[50,51] For SiN_x, measurements showed unexpected high thermal conductivity compared with minimum thermal conductivity, which might come from the presence of long MFP propagons.[28,46] Therefore, it is likely that excluding the porosity factor, the phononic crystal patterning reducing the thermal conductivities in this study mainly by blocking long MFP propagons.

The observed neck size dependence of thermal is useful to qualitatively estimate the MFP distribution of porpagons.[52] The e-beam patterned sample with p = 800 nm and n = 323 nm only exhibited 8% lower thermal conductivity, indicating that propagons with MFPs greater than 323 nm contribute little to heat transport. Whereas DSA patterned SiN_x with p = 37.5 nm and n = 12 nm decreased thermal conductivity by 61%, showing that at this length scale a large amount of propagons are blocked. Our results indicate that propagons with MFP between 12 nm and 321 nm contribute to half of the heat conduction in SiN_x at room temperature. Further investigation is required both experimentally and theoretically to shed light on the exact length scales of the propagons in SiN_x. Using the fabrication platform developed in this study, we would further adjust the porosity of DSA patterned holes and make e-beam patterned phononic crystals with various p and n, which are however beyond the scope of this work. We will report more physical discussion and the comprehensive study about SiN_x phononic crystals elsewhere.

5.4.3 Impact of lattice orientation

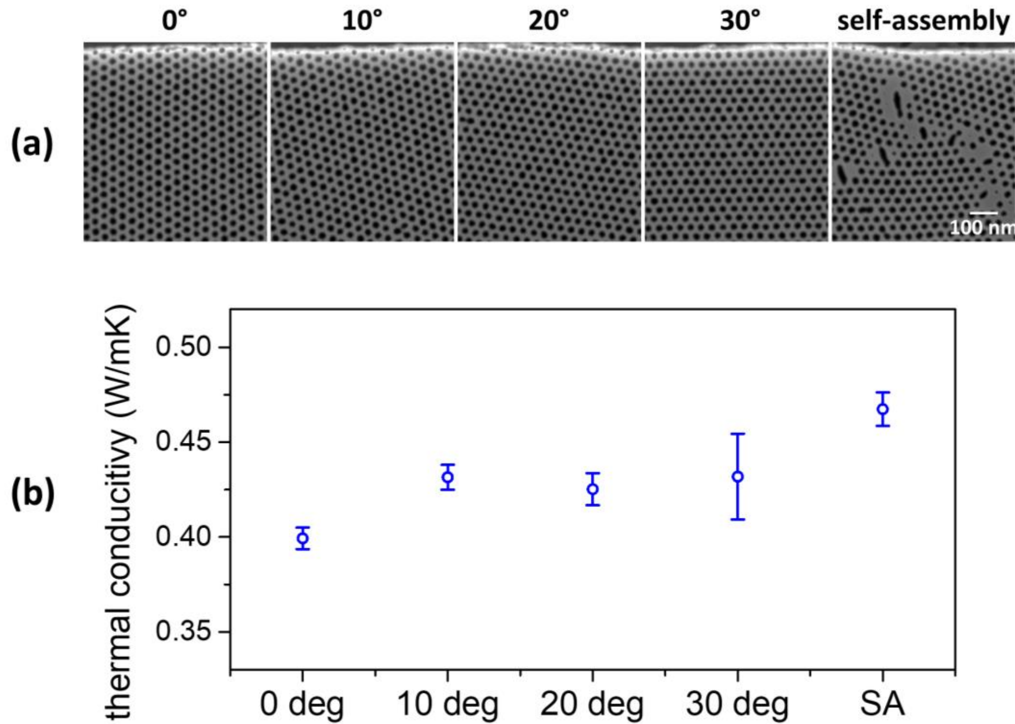

Figure 5-10: (a) SEM images and (b) corresponding thermal conductivities of DSA patterned silicon nitride phononic crystals with four different rotation angles and self-assembled holes. The SEM images were taken near the longer edges of bridges.

It is known for single crystal Si phononic crystals that phonon could travel ballistically in the aligned lattice.[6,7,38] To investigate whether the propagons in amorphous SiN_x travel with similar directionality, DSA samples with different rotation angles were measured. The self-assembly pattern where holes were packed in small and multidirectional grains was also included for comparison. The results are summarized in Figure 5-10. The direct phonon path in DSA sample of 0° rotation is fully blocked. When rotating additional 10°, 20° and 30°, the direct phonon path keeps increasing until fully opens at 30°. The κ of 0° sample is the smallest but is less than 10% smaller than those of other three lattice orientations, which is however within the measurement error range. As for the self-assembly pattern, the κ about 17% higher than that of 0° DSA sample, and 9% higher than those of 10°, 20° and 30° samples. Given that phonons mainly travel

incoherently at room temperature, this different could simply rise from its smaller porosity due to some defective cylinders weren't transferred to SiN_x around grain boundaries.

Anufriev et al. studied two types of hole arrangement in Si phononic crystals: squared lattice, in which phonons can travel in straight line, and staggered hexagonal lattice, in which the direct path of phonons is blocked.[7] They found phonons traveled faster through the aligned lattice than through the staggered lattice. There was 30% difference in thermal decay time when neck width was 30 nm at room temperature and the difference increased at lower temperature. In this study, we observed a much smaller impact of lattice orientation and phonon pathway in amorphous SiN_x phononic crystals, even though the neck width via DSA is much smaller compared with the Si phononic crystals. It indicates that in amorphous materials, due to the disorder atomic lattice, propagons, which like phonons have long MFP, travel in more random directions.

5.5 Conclusions

We presented the fabrication strategy of amorphous SiN_x phononic crystals for thermoreflectance measurement. Using DSA of BCP cylinders, hexagonal packed holes with pitch as small as 37.5 nm were generated in SiN_x thin films. The integration of the DSA patterning with the phononic crystal device fabrication was successfully demonstrated. The thermoreflectance measurement results showed that the DSA patterned SiN_x phononic crystals have 61% reduction in thermal conductivity. In comparison, the e-beam patterned holes with larger pitch and neck width reduced the thermal conductivity for only 8%. Our results indicate that one can use nanostructuring route to engineer the thermal properties of amorphous materials.

These experiments provide strong evidence that the heat transport in amorphous materials, like SiN_x, with long MFP propagons significantly contributing to their thermal conductivities, could be influenced by small nanostructures even at room temperature. The micromachining of SiN_x

bridges with different nanostructures we described here allows reliable measurement of thermal conductivity and is suitable to further investigate nanoscale heat transfer in amorphous solids. The small pitch and neck width provided by block copolymer patterning enable manipulating phonons with broad range of MFPs and making ultra-low thermal conductivity thin films with useful device-relevant thermal properties.

5.6 References

(1) Schierning, G. Silicon Nanostructures for Thermoelectric Devices: A Review of the Current State of the Art. *Phys. Status Solidi* **2014**, *211* (6), 1235–1249.

(2) Maldovan, M. Sound and Heat Revolutions in Phononics. *Nature* **2013**, *503* (7475), 209–217.

(3) Heremans, J. P.; Dresselhaus, M. S.; Bell, L. E.; Morelli, D. T. When Thermoelectrics Reached the Nanoscale. *Nat. Nanotechnol.* **2013**, *8* (7), 471–473.

(4) Nomura, M.; Shiomi, J.; Shiga, T.; Anufriev, R. Thermal Phonon Engineering by Tailored Nanostructures. *Jpn. J. Appl. Phys.* **2018**, *57* (8), 080101.

(5) Tang, J.; Wang, H. T.; Lee, D. H.; Fardy, M.; Huo, Z.; Russell, T. P.; Yang, P. Holey Silicon as an Efficient Thermoelectric Material. *Nano Lett.* **2010**, *10* (10), 4279–4283.

(6) Lee, J.; Lim, J.; Yang, P. Ballistic Phonon Transport in Holey Silicon. *Nano Lett.* **2015**, *15* (5), 3273–3279.

(7) Anufriev, R.; Ramiere, A.; Maire, J.; Nomura, M. Heat Guiding and Focusing Using Ballistic Phonon Transport in Phononic Nanostructures. *Nat. Commun.* **2017**, *8* (May), 15505.

(8) Yu, J. K.; Mitrovic, S.; Tham, D.; Varghese, J.; Heath, J. R. Reduction of Thermal Conductivity in Phononic Nanomesh Structures. *Nat. Nanotechnol.* **2010**, *5* (10), 718–721.

(9) Mahan, G. D. Introduction to Thermoelectrics. *APL Mater.* **2016**, *4* (10), 104806.

(10) Hochbaum, A. I.; Chen, R.; Delgado, R. D.; Liang, W.; Garnett, E. C.; Najarian, M.; Majumdar, A.; Yang, P. Enhanced Thermoelectric Performance of Rough Silicon Nanowires. *Nature* **2008**, *451* (7175), 163–167.

(11) Maire, J.; Anufriev, R.; Hori, T.; Shiomi, J.; Volz, S.; Nomura, M. Thermal Conductivity Reduction in Silicon Fishbone Nanowires. *Sci. Rep.* **2018**, *8* (1), 4452.

(12) Ali, A.; Chen, Y.; Vasiraju, V.; Vaddiraju, S. Nanowire-Based Thermoelectrics. *Nanotechnology* **2017**, *28* (28), 282001.

(13) Pernot, G.; Stoffel, M.; Savic, I.; Pezzoli, F.; Chen, P.; Savelli, G.; Jacquot, A.; Schumann, J.; Denker, U.; Mönch, I.; et al. Precise Control of Thermal Conductivity at the Nanoscale through Individual Phonon-Scattering Barriers. *Nat. Mater.* **2010**, *9* (6), 491–495.

(14) Ravichandran, J.; Yadav, A. K.; Cheaito, R.; Rossen, P. B.; Soukiassian, A.; Suresha, S. J.; Duda, J. C.; Foley, B. M.; Lee, C. H.; Zhu, Y.; et al. Crossover from Incoherent to Coherent Phonon Scattering in Epitaxial Oxide Superlattices. *Nat. Mater.* **2014**, *13* (2), 168–172.

(15) Anufriev, R.; Maire, J.; Nomura, M. Reduction of Thermal Conductivity by Surface Scattering of Phonons in Periodic Silicon Nanostructures. *Phys. Rev. B* **2016**, *93* (4), 045411.

(16) Yanagisawa, R.; Maire, J.; Ramiere, A.; Anufriev, R.; Nomura, M. Impact of Limiting Dimension on Thermal Conductivity of One-Dimensional Silicon Phononic Crystals. *Appl. Phys. Lett.* **2017**, *110* (13), 133108.

(17) Maldovan, M. Phonon Wave Interference and Thermal Bandgap Materials. *Nat. Mater.* **2015**, *14* (7), 667–674.

(18) Maldovan, M.; Thomas, E. L. *Periodic Materials and Interference Lithography: For Photonics, Phononics and Mechanics*; 2009.

(19) Zen, N.; Puurtinen, T. A.; Isotalo, T. J.; Chaudhuri, S.; Maasilta, I. J. Engineering Thermal Conductance Using a Two-Dimensional Phononic Crystal. *Nat. Commun.* **2014**, *5* (1), 3435.

(20) Wang, X.; Huang, B. Computational Study of In-Plane Phonon Transport in Si Thin Films. *Sci. Rep.* **2015**, *4* (1), 6399.

(21) Lee, J.; Lee, W.; Wehmeyer, G.; Dhuey, S.; Olynick, D. L.; Cabrini, S.; Dames, C.; Urban, J. J.; Yang, P. Investigation of Phonon Coherence and Backscattering Using Silicon Nanomeshes. *Nat. Commun.* **2017**, *8*, 14054.

(22) Anufriev, R.; Ramiere, A.; Maire, J.; Nomura, M. Heat Guiding and Focusing Using Ballistic Phonon Transport in Phononic Nanostructures. *Nat. Commun.* **2017**, *8*, 15505.

(23) Nomura, M.; Kage, Y.; Nakagawa, J.; Hori, T.; Maire, J.; Shiomi, J.; Anufriev, R.; Moser, D.; Paul, O. Impeded Thermal Transport in Si Multiscale Hierarchical Architectures with Phononic Crystal Nanostructures. *Phys. Rev. B - Condens. Matter Mater. Phys.* **2015**, *91* (20), 1–6.

(24) Segalman, R. A. Patterning with Block Copolymer Thin Films. *Mater. Sci. Eng. R Reports* **2005**, *48* (6), 191–226.

(25) Thurn-Albrecht, T.; Steiner, R.; DeRouchey, J.; Stafford, C. M.; Huang, E.; Bal, M.; Tuominen, M.; Hawker, C. J.; Russell, T. P. Nanoscopic Templates from Oriented Block Copolymer Films. *Adv. Mater.* **2000**, *12* (11), 787–791.

(26) Jung, Y. S.; Ross, C. A. Well-Ordered Thin-Film Nanopore Arrays Formed Using a Block-Copolymer Template. *Small* **2009**, *5* (14), 1654–1659.

(27) Lim, J.; Wang, H. T.; Tang, J.; Andrews, S. C.; So, H.; Lee, J.; Lee, D. H.; Russell, T. P.; Yang, P. Simultaneous Thermoelectric Property Measurement and Incoherent Phonon Transport in Holey Silicon. *ACS Nano* **2016**, *10* (1), 124–132.

(28) Wingert, M. C.; Zheng, J.; Kwon, S.; Chen, R. Thermal Transport in Amorphous Materials: A Review. *Semicond. Sci. Technol.* **2016**, *31* (11), 113003.

(29) Einstein, A. Elementare Betrachtungen Über Die Thermische Molekularbewegung in Festen Körpern. *Ann. Phys.* **1911**, *340* (9), 679–694.

(30) Cahill, D. G.; Watson, S. K.; Pohl, R. O. Lower Limit to the Thermal Conductivity of Disordered Crystals. *Phys. Rev. B* **1992**, *46* (10), 6131–6140.

(31) Slack, G. A. The Thermal Conductivity of Nonmetallic Crystals. *Solid State Phys. - Adv. Res. Appl.* **1979**.

(32) Radziemska, E. Thermal Performance of Si and GaAs Based Solar Cells and Modules: A Review. *Progress in Energy and Combustion Science*. 2003.

(33) Goodson, K. E.; Flik, M. I.; Su, L. T.; Antoniadis, D. A. Prediction and Measurement of the Thermal Conductivity of Amorphous Dielectric Layers. *J. Heat Transfer* **2008**.

(34) Kaloyeros, A. E.; Jové, F. A.; Goff, J.; Arkles, B. Review—Silicon Nitride and Silicon Nitride-Rich Thin Film Technologies: Trends in Deposition Techniques and Related Applications. *ECS J. Solid State Sci. Technol.* **2017**, *6* (10), 691–714.

(35) Zhou, C.; Segal-Peretz, T.; Oruc, M. E.; Suh, H. S.; Wu, G.; Nealey, P. F. Fabrication of Nanoporous Alumina Ultrafiltration Membrane with Tunable Pore Size Using Block Copolymer Templates. *Adv. Funct. Mater.* **2017**, *27* (34), 1701756.

(36) Laconte, J.; Flandre, D.; Raskin, J. P. *Micromachined Thin-Film Sensors for SOI-CMOS Co-Integration*; Springer US, 2006.

(37) Nomura, M.; Kage, Y.; Nakagawa, J.; Hori, T.; Maire, J.; Shiomi, J.; Anufriev, R.; Moser, D.; Paul, O. Impeded Thermal Transport in Si Multiscale Hierarchical Architectures with Phononic Crystal Nanostructures. *Phys. Rev. B - Condens. Matter Mater. Phys.* **2015**.

(38) Maire, J.; Anufriev, R.; Nomura, M. Ballistic Thermal Transport in Silicon Nanowires. *Sci. Rep.* **2017**, *7* (1), 41794.

(39) Schmidt, A. J.; Cheaito, R.; Chiesa, M. Characterization of Thin Metal Films via Frequency-Domain Thermoreflectance. *J. Appl. Phys.* **2010**, *107* (2), 024908.

(40) Park, S. M.; Craig, G. S. W.; Liu, C. C.; La, Y. H.; Ferrier, N. J.; Nealey, P. F. Characterization of Cylinder-Forming Block Copolymers Directed to Assemble on Spotted Chemical Patterns. *Macromolecules* **2008**, *41* (23), 9118–9123.

(41) Ruiz, R.; Kang, H.; Detcheverry, F. A.; Dobisz, E.; Kercher, D. S.; Albrecht, T. R.; De Pablo, J. J.; Nealey, P. F. Density Multiplication and Improved Lithography by Directed Block Copolymer Assembly. *Science (80-.).* **2008**, *321* (5891), 936–939.

(42) Wan, L.; Yang, X. Directed Self-Assembly of Cylinder-Forming Block Copolymers: Prepatterning Effect on Pattern Quality and Density Multiplication Factor. *Langmuir* **2009**, *25* (21), 12408–12413.

(43) Yang, X. M.; Wan, L.; Xiao, S.; Xu, Y.; Weller, D. K. Directed Block Copolymer Assembly versus Electron Beam Lithography for Bit-Patterned Media with Areal Density of 1 Terabit/Inch2and Beyond. *ACS Nano* **2009**, *3* (7), 1844–1858.

(44) Kang, H.; Craig, G. S. W.; Han, E.; Gopalan, P.; Nealey, P. F. Degree of Perfection and Pattern Uniformity in the Directed Assembly of Cylinder-Forming Block Copolymer on Chemically Patterned Surfaces. *Macromolecules* **2012**, *45* (1), 159–164.

(45) Tada, Y.; Akasaka, S.; Yoshida, H.; Hasegawa, H.; Dobisz, E.; Kercher, D.; Takenaka, M. Directed Self-Assembly of Diblock Copolymer Thin Films on Chemically-Patterned Substrates for Defect-Free Nano-Patterning. *Macromolecules* **2008**, *41* (23), 9267–9276.

(46) Sultan, R.; Avery, A. D.; Underwood, J. M.; Mason, S. J.; Bassett, D.; Zink, B. L. Heat

Transport by Long Mean Free Path Vibrations in Amorphous Silicon Nitride near Room Temperature. *Phys. Rev. B* **2013**, *87* (21), 214305.

(47) Allen, P. B.; Feldman, J. L. Thermal Conductivity of Disordered Harmonic Solids. *Phys. Rev. B* **1993**, *48* (17), 12581–12588.

(48) Allen, P. B.; Feldman, J. L.; Fabian, J.; Wooten, F. Diffusons, Locons and Propagons: Character of Atomie Yibrations in Amorphous Si. *Philos. Mag. B Phys. Condens. Matter; Stat. Mech. Electron. Opt. Magn. Prop.* **1999**, *79* (11–12), 1715–1731.

(49) Feldman, J. L.; Kluge, M. D.; Allen, P. B.; Wooten, F. Thermal Conductivity and Localization in Glasses: Numerical Study of a Model of Amorphous Silicon. *Phys. Rev. B* **1993**, *48* (17), 12589–12602.

(50) He, Y.; Donadio, D.; Galli, G. Heat Transport in Amorphous Silicon: Interplay between Morphology and Disorder. *Appl. Phys. Lett.* **2011**, *98* (14), 144101.

(51) Regner, K. T.; Sellan, D. P.; Su, Z.; Amon, C. H.; McGaughey, A. J. H.; Malen, J. A. Broadband Phonon Mean Free Path Contributions to Thermal Conductivity Measured Using Frequency Domain Thermoreflectance. *Nat. Commun.* **2013**, *4* (1), 1640.

(52) Nomura, M.; Nakagawa, J.; Sawano, K.; Maire, J.; Volz, S. Thermal Conduction in Si and SiGe Phononic Crystals Explained by Phonon Mean Free Path Spectrum. *Appl. Phys. Lett.* **2016**, *109* (17), 1–5.

CHAPTER 6: CONCLUSION

The work in this thesis demonstrates the capabilities as well as several design considerations of using block copolymer for nanofabrication. Chapter 2 shows the advantages of using self-assembled block copolymer in separation membrane applications, including highly uniform feature size, simple process, and ability to template inorganic materials. We discussed that to utilize the self-assembled block copolymer thin films, the interfacial energy as well the surface energy needs to be carefully controlled to achieved desired microdomain orientation.

The interfacial energy plays an important role in block copolymers annealed within confinement as well. In chapter 3, we used STEM tomography, which is an advanced metrology to characterize the three-dimensional block copolymer structures, to understand how the surface chemistry as well as the geometry of the cylindrical template influence the through-film morphology of single cylinders self-assembled within confinement. This study is helpful to understand the sources of defects when applying the DSA cylinders to pattern high resolution contacts holes for future generation integrated circuits.

Templated block copolymer lamella is very useful to pattern unidirectional line and space patterns. In chapter 4, using chemical contrast patterns to DSA a high-χ BCP followed by self-aligned double patterning, a total density multiplication factor of 8 was achieved in comparison to the original sparse guiding pattern. The final line and space patterns have full pitch as small as 10.5 nm, which could be developed as the future lithography method to manufacture bit-patterned media with high storage density in hard-disk drive industry.

Block copolymer patterning offers easy process to fabricate uniform nanostructures, which could be integrated with device fabrication to study nanoscale physics. Chapter 5 describes how to template arrays of hexagonal packed holes in suspending silicon nitride film using block

copolymer and the fabrication procedure of phononic crystal device for thermoreflectance measurement. As expected from the small pitch and neck size provided by block copolymer, a great reduction in thermal conductivity is observed from thermoreflectance measurements. The difference with classic predicted thermal conductivity leads to discussions about nanoscale phonon transport in amorphous solids.